The Dissertation Committee for Kelly Marriott Thom Certifies that this is the approved version of the following dissertation:

Growth and Characterization of Ru Films Deposited by Chemical Vapor Deposition: Towards Enhanced Nucleation and Film Properties

Committee:

John G. Ekerdt, Supervisor

Gyeong S. Hwang

Richard A. Jones

Charles B. Mullins

Noel M. Russell

Growth and Characterization of Ru Films Deposited by Chemical Vapor Deposition: Towards Enhanced Nucleation and Film Properties

by

Kelly Marriott Thom, B.S.

Dissertation

Presented to the Faculty of the Graduate School of
The University of Texas at Austin
in Partial Fulfillment
of the Requirements
for the Degree of

Doctor of Philosophy

The University of Texas at Austin
December, 2009

Dedication

To my husband, Jeff.

Acknowledgements

I would like to extend my deepest gratitude to my advisor, Dr. John G. Ekerdt, for his guidance and patience. I genuinely appreciate all of the support and counsel he has given me during my graduate studies. Dr. Ekerdt always offered valuable advice when it seemed as if my research was at a standstill, and he was always available to help regardless of the demands of his busy schedule. I am also very grateful to my colleagues in the Ekerdt group, who provided invaluable support and advice. I am especially thankful to Wyatt Winkenwerder, Luke Henderson, and Ryan Fitzpatrick for insightful discussions regarding my research, as well as always lending a helping hand when one of my systems needed maintenance or repair.

I would also like to acknowledge Dr. Yang-Ming Sun for his expertise in UHV systems and surface analysis. I sincerely thank him for teaching me about the operation of UHV systems, as well as how to design experiments and interpret data. His genuine kindness and patience were always appreciated. I also thank Dr. Hugo Celio for his training and support on the high resolution XPS and SEM. I offer thanks to Jim Smitherman and Butch Cunningham, who manage the Chemical Engineering Instrumentation and Repair Shop. I appreciate all of the work they did to support not only my research, but that of the entire Ekerdt group.

I am also grateful to Dr. Timothy J. Anderson at the University of Florida for acting as my undergraduate research advisor for the 2.5 years that I worked in his group. I owe a special thank you to his former student, Dr. Omar Bchir, for mentoring me in the laboratory and encouraging me to pursue graduate school. My initial knowledge and interest in thin film deposition came from working with Omar.

Finally, I thank the Semiconductor Research Corporation (SRC) for their financial support during my graduate studies. I am especially honored and grateful to have been the first recipient of the GRC/Al Tasch Fellowship for doctoral study in microelectronics-related disciplines. In addition to the financial award, the SRC provided invaluable opportunities to network with other students and members of industry, most notably during the annual Techcon conference.

Growth and Characterization of Ru Films Deposited by Chemical Vapor Deposition: Towards Enhanced Nucleation and Film Properties

Publication No._____________

Kelly Marriott Thom, Ph.D.
The University of Texas at Austin, 2009

Supervisor: John G. Ekerdt

As device dimensions in integrated circuits scale down, there is an increasing need to deposit ultra-thin, smooth, continuous films for use in applications such as the liner in back end processing. The liner must have good adhesion to both Cu and the dielectric, act as a Cu diffusion barrier, and be conductive enough to allow the electroplating of Cu. Ruthenium (Ru) has been considered as a possible material to be implemented into the liner due to its low electrical resistivity, high thermal and chemical stability, and negligible solubility with copper. Chemical vapor deposition (CVD) is an attractive growth technique for Ru films because it allows conformal deposition in high-aspect ratio features. However, there are some limitations that must be overcome in the deposition of Ru films. CVD Ru films suffer from poor nucleation on oxide and nitride substrates. Poor nucleation leads to rough, large-grained polycrystalline columnar films, which may not coalesce into a continuous film until the thickness greatly exceeds the requirements for the liner. This dissertation presents surface chemistry and film growth studies involving Ru CVD and focuses on improving the nucleation and properties of Ru films.

In situ surface analysis techniques including X-ray photoelectron spectroscopy (XPS) and temperature programmed desorption (TPD) were used to study the fundamental adsorption behavior of the Ru precursor, (2,4-dimethylpentadienyl)(ethylcyclopentadienyl)Ru or DER, on polycrystalline Ta, both with and without iodine adsorbed on the Ta. Based upon these results, CVD films were grown using DER/O_2, and it was shown that nucleation and film properties can be improved by the addition of methyl iodide. Ru films grown using DER/O_2 show sparse nucleation, which leads to very rough surface topography and large polycrystalline columnar grains. The addition of methyl iodide during growth significantly improves nucleation and results in smoother, smaller-grained films. Iodine adsorbs on the initially-formed Ru islands and continuously segregates through the film to the surface during the entire deposition. In addition, CVD films grown with $Ru_3(CO)_{12}$ were studied. Use of the $Ru_3(CO)_{12}$ precursor results in thin, ultra-smooth films that show little to no columnar grain structure.

Table of Contents

List of Tables

List of Figures

List of Illustrations

Chapter 1: Introduction

1.1 OVERVIEW

Over the last 50 years, advancements in semiconductor device fabrication have led to increasing device performance. The demands for increased speed, power, and functionality along with reduced cost have been met primarily by decreasing the physical dimensions of device features [1]. In 1965, Moore predicted that the number of transistors per chip will double every 2 years [2]. Thus far, the semiconductor industry has been able to meet the demands of Moore's Law and it is expected that the scaling of device dimensions will continue well into the future.

Shrinking device size leads to new manufacturing and materials challenges, such as those involved with scaling of the interconnect. The interconnect consists of conductive wires and dielectric materials that connect transistors and deliver electrical signals and power to the various components on an integrated circuit (IC). At the 250 nm node and below, IC performance is limited by the interconnect time delay, also known as the resistance-capacitance (*RC*) delay [3,4]. The RC time delay is a product of the resistance (*R*) of the metal lines and the capacitance (*C*) due to the insulating dielectric layers. Assuming that the dielectric space above and below the metal line is equal to the line thickness (*T*), and the dielectric space adjacent to the metal line is equal to the metal line width (*W*), as depicted in Illustration 1.1a, the RC delay can be expressed as [5,6]:

$$R = \frac{\rho L}{WT} \tag{1.1}$$

$$C = 2(C_L + C_v) = 2kL(\frac{T}{W} + \frac{W}{T}) \tag{1.2}$$

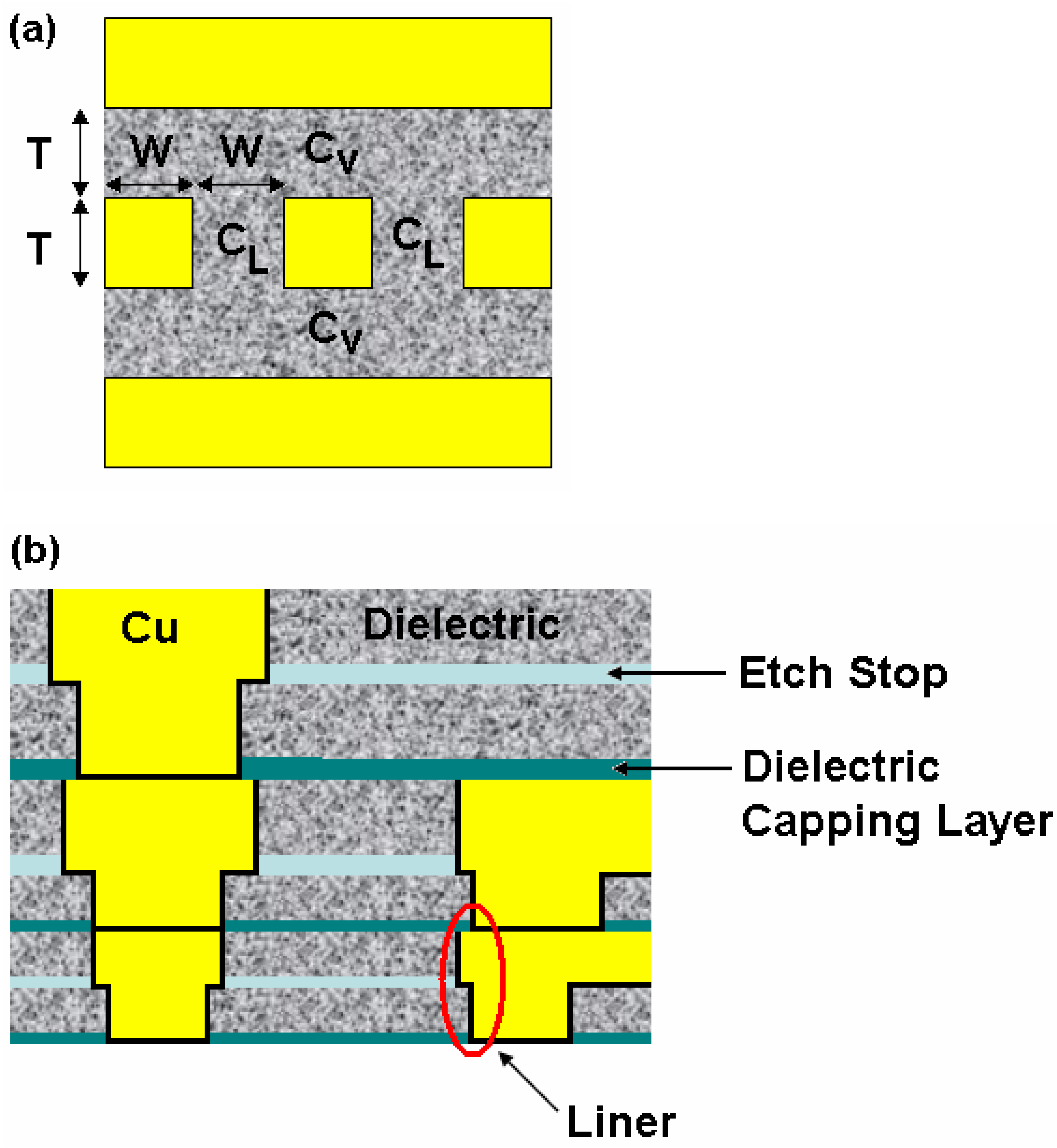

Illustration 1.1. Cross-section illustrations of Cu interconnects formed in a dual damascene process a) depicting the dimensions used in estimating *RC* delay, adapted from [5] and b) showing the liner material.

$$RC = 2\rho k L^2 \left(\frac{1}{W^2} + \frac{1}{T^2} \right) \tag{1.3}$$

where ρ is the resistivity of the metal line, k is the dielectric constant of the dielectric material, L is the length of the metal line, C_L is the lateral capacitance between adjacent metal lines, and C_V is the vertical capacitance between wiring levels. Because there are multiple layers with differing dielectric constants in an IC, the value of k used in Equations 1.2 and 1.3 should be an effective k value that can be determined experimentally.

As the interconnect dimensions T and W scale down, the RC delay will increase. In order to combat increases in RC delay due to shrinking device dimensions, new materials have been introduced into production that lower the metal wire resistance and reduce the capacitance of the dielectrics. To this end, Al and SiO_2 have been replaced with Cu and low-k dielectrics. Cu is superior to Al due to its lower bulk resistivity (1.7 μΩ-cm for Cu vs. 2.7 μΩ-cm for Al) and its superior electromigration resistance, which is several orders of magnitude higher than that of Al [7]. The introduction of low-k dielectrics began with replacing SiO_2 (k = 3.9-4.1) with fluorine doped SiO_2 (k = 3.7) [1]. Further improvements have been made with the introduction of insulating materials such as organosilicate glasses (k = 2.6-3.1) [8]. The development of porous low-k materials is ongoing; however, the integration of these materials is proving to be quite problematic [1].

Massive gains in performance and cost have been realized due to the use of Cu and low-k dielectric materials; however, the introduction of these new materials has led to manufacturing and materials challenges.

1.2 BACKGROUND

1.2.1 The Interconnect

The first chips containing Cu were introduced in 1998 [1]. Since that time, many obstacles have been overcome, including the development of a new metallization process, while many new difficulties have arisen, such as those involving scaling of the liner material.

1.2.1.1 Cu Metallization

The implementation of the Cu interconnect has revolutionized back-end processing; however, Cu metallization required major changes from its Al predecessor. Al deposition was followed by reactive ion etching (RIE) to make a pattern. However, it is very difficult to etch Cu because it does not form volatile by-products. To overcome difficulties with etching Cu, a new integration scheme, the dual-damascene process, was developed [6]. In the dual-damascene process, features (vias and trenches) are etched into the dielectric layers and then are subsequently filled with Cu by electroplating. Excess Cu is then removed by chemical mechanical planarization (CMP). A cross-section of Cu interconnects formed in a dual-damascene process is shown in Illustration 1.1b.

The implementation of Cu and the dual-damascene process have allowed significant improvements such as increased conductivity, reduced capacitance, decreased number of interconnect levels, decreased power consumption, and decreased cost due to fewer manufacturing steps [9], but with these benefits come several drawbacks. Cu is a fast diffuser into surrounding materials, including Si, SiO_2, and low-k dielectrics. Cu diffusion into neighboring layers can cause an increase in contact resistance, leaky p-n junctions, the formation of deep level traps, and destruction of electrical connections that can ultimately cause serious device degradation and failure [10]. Furthermore, Cu has very poor adhesion with dielectric materials. In order to prevent Cu diffusion, a diffusion barrier material must be deposited between the Cu and surrounding materials. Due to issues with adhesion to both the dielectric and the Cu, diffusion barriers are typically implemented in a multilayer stack, which is often called the liner material. The liner material must be have good adhesion to both the Cu and dielectric, prevent Cu diffusion, and be conductive enough to allow the electrodeposition of Cu.

1.2.1.2 The Liner Material

The current commercial liner material is shown in Illustration 1.2a [6]. The TaN layer acts as the Cu diffusion barrier and has good adhesion to the dielectric. The Ta layer acts as a diffusion barrier to some extent (not as well as TaN), but is included in the stack primarily because of its good adhesion with Cu [6]. However, Cu cannot be electroplated directly on the Ta because of the formation of a surface oxide [11], thus a Cu seed layer is deposited on the Ta to enable Cu electrodeposition. Currently, the liner material is deposited by ionized physical vapor deposition (I-PVD). PVD is a technique in which the directionality of the atoms traveling towards the substrate during growth causes step shadowing and makes it very difficult to deposit conformal films in high-aspect ratio features. It is believed that PVD will not be extendable as device dimensions continue to shrink and thinner liner materials are required. However, advances in PVD have proven these predictions wrong in the past. Eventually the physical processes will have to give way to chemical processes. The International Technology Roadmap for

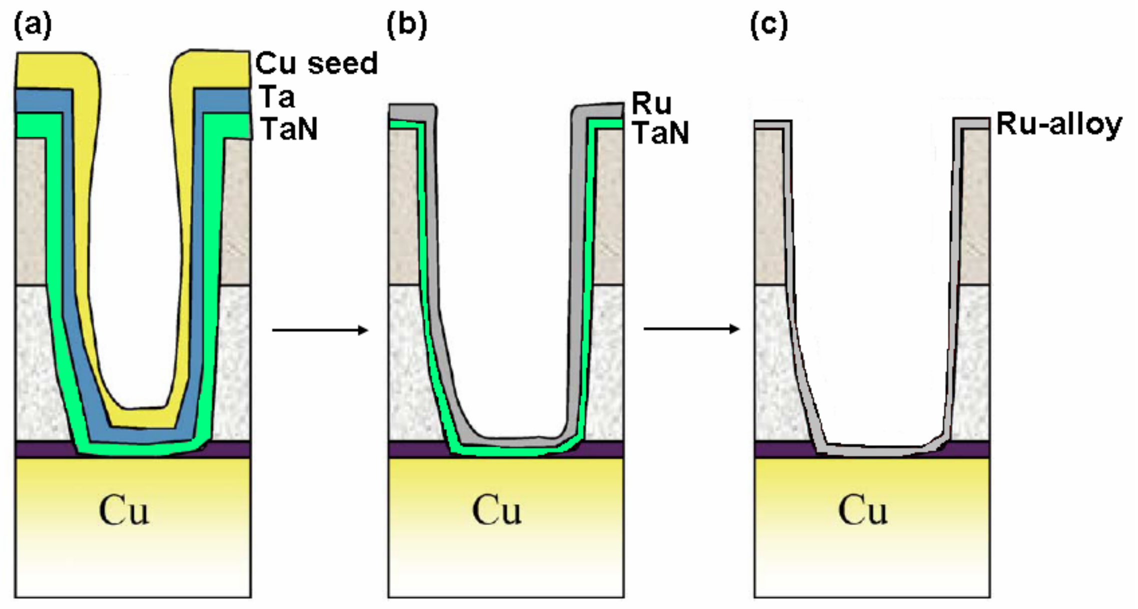

Illustration 1.2. Schematic representation of the a) current commercial liner of TaN/Ta/Cu seed deposited by ionized-PVD, b) next generation liner of TaN/Ru deposited by CVD or ALD, and c) later technology Ru-alloy deposited by CVD, adapted from [6].

Semiconductors (ITRS) projects that the liner thickness will need to be 3.3 nm, 2.4 nm, and 1.7 nm for the 45 nm, 32 nm, and 22 nm nodes, respectively [1].

Ideally, the TaN/Ta/Cu seed multilayer liner should be replaced with a single-layer material that has good adhesion to both the Cu and dielectric, prevents Cu diffusion, and is conductive enough to allow the electrodeposition of Cu. However, it is difficult to find one material that meets all of these criteria. The microstructure of the diffusion barrier material is of major concern. The film microstructure can be classified as single crystal, polycrystalline, or amorphous. The ideal diffusion barrier is a defect free single crystal, which does not contain grain boundaries; however, deposition of single crystal films on small damascene structures is impractical [10]. Grain boundaries in films act as facile paths for diffusion and severely limit the performance of a barrier material. Polycrystalline films, especially those with columnar structure, are the least desirable for diffusion barrier applications. These films often have grain boundaries that extend from one side of the barrier to other and provide a facile path for Cu diffusion. Nanocrystalline films, which also have grain boundaries, perform better than polycrystalline films because the distance for Cu to diffuse through the barrier is significantly increased. Amorphous films are the most effective as diffusion barriers due to their lack of grain boundaries. It is also possible to create a diffusion barrier by adding contaminants (such as N, C, P) that stuff the grain boundaries and suppress diffusion [12]. In consideration of the liner material, it is often difficult to find a material with appropriate microstructure to act as a diffusion barrier, as well as have good adhesion to both Cu and dielectric, and be electrically conductive.

Emerging solutions for the liner material involve deposition with alternative techniques, as well as the introduction of new materials. Techniques such as chemical vapor deposition (CVD) and atomic layer deposition (ALD) allow conformal deposition of ultra-thin films in high-aspect ratio features and will most likely replace PVD for deposition of the liner. One promising alternative for the liner is depicted in Illustration 1.2b. The TaN diffusion barrier, previously deposited by PVD, may be deposited by ALD, decreasing the thickness from ~ 10 nm to < 2 nm [6]. Furthermore, the Ta/Cu seed layer may be replaced by CVD or ALD Ru.

Ru is a desirable material in the liner because of its low electrical resistivity, high thermal and chemical stability, and negligible solubility with Cu [13]. Ru does not oxidize easily and even if some oxidation occurs, RuO_2 is still highly conductive. Furthermore, Ru has good adhesion to Cu. Because of this, Ru can replace the Ta/Cu seed layer bi-layer stack, as Cu can be directly plated on Ru [14]. It is generally accepted that Ru alone is not a viable Cu diffusion barrier [1]. Ru almost always shows polycrystalline columnar structure. However, alloys of Ru with P have shown promising barrier properties, as they form amorphous films and the grain boundaries are eliminated [15,16]. Ideally, the multilayer liner could be replaced with a CVD Ru-alloy film, as shown in Illustration 1.2c. A Ru-alloy film should have good adhesion to the Cu, prevent Cu diffusion, and be conductive enough to allow the electrodeposition of Cu; however, Ru shows poor adhesion with the dielectric [17], and this obstacle would need to be overcome.

1.2.2 Nucleation in CVD Film Growth

Although CVD Ru films are attractive candidates for use in the liner material, there are some limitations that must be overcome in the deposition of Ru films. CVD Ru films suffer from poor nucleation on oxide and nitride substrates, such as SiO_2 [18-20], Si_3N_4 [21,22] and TiN [23,24]. The issue of nucleation will become increasingly significant with decreasing device dimensions. The required liner thickness will be < 3 nm for technology nodes beyond 45 nm, thus the liner must be the thinnest possible continuous film that retains the required material properties. A high initial nucleation density is essential to achieve continuity of ultra-thin films; poor nucleation leads to sparse islands on the substrate surface, which do not coalesce into a continuous film until the thickness greatly exceeds the requirements for the liner material. Furthermore, poor nucleation results in films with increased surface roughness, and high surface roughness leads to a significant increase in resistivity [25,26]. Inadequate nucleation in Ru film growth is evidenced by long incubation times at the onset of growth [18,20,27,28], sparse island formation [24,29-32], porous films that do not fully coalesce [6,18,24,29,33], and increased film roughness [18,29,32,33].

In order to take advantage of the benefits of implementing CVD Ru films in the liner, it is necessary to develop techniques to improve nucleation of Ru on oxide and nitride substrates.

1.2.2.1 Nucleation Theory

The extent of nucleation is primarily determined by the reactivity of a surface towards adsorption and dissociation of the precursor. Classically, nucleation and subsequent film growth are explained in terms of the relative interfacial surface energies of the substrate and film, as shown in Illustration 1.3. The three relevant interfacial energies are γ_{sv} (substrate-vapor), γ_{sf} (substrate-film) and γ_{fv} (film-vapor).

If the criterion $\gamma_{fv} < \gamma_{sv} + \gamma_{sf}$ is met, then layer-by-layer (2D or Frank-van der Merwe) growth occurs, but this growth mode is only observed in practice for semiconductor homoepitaxy. Alternatively, island (3D or Volmer-Weber) growth arises when the criterion $\gamma_{fv} > \gamma_{sv} + \gamma_{sf}$ is met, which is usually the case for CVD deposition of metals on oxides and nitrides. And finally, the Stranski-Krastanov (SK) growth mode arises when one or more layers grow in layer-by-layer and then island growth occurs on top of the first layer(s). SK growth is often observed in heteroepitaxy [34].

Although classical models adequately describe island formation, an atomistic view of nucleation is necessary to illustrate the behavior of molecules on a surface. Illustration 1.4 depicts the different processes that may occur in nucleation of CVD films. A schematic diagram for the general CVD process is depicted in Illustration 1.4a. Gas phase reactants diffuse to the substrate surface and adsorb. Several surface processes take place, including surface diffusion and reaction, and then reaction by-products desorb and diffuse away from the surface. Illustration 1.4b describes these processes in more detail. A precursor molecule arrives from the gas phase (1) and may then diffuse across the surface (2) before reacting. The molecule may partially dissociate (3) or may fully dissociate to form an adatom (4). Adatoms may complete a subcritical cluster by merging with it (5) or may join an existing stable cluster (6). Finally, reaction by-products desorb and diffuse away from the surface (7) or may become incorporated into the growing film [34].

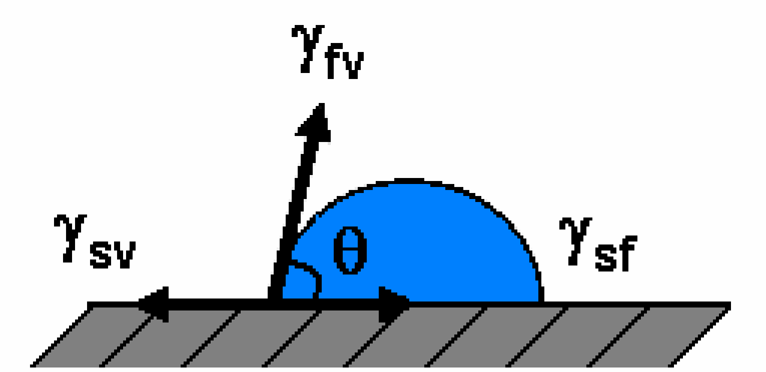

Illustration 1.3. Interfacial surface energies involved in nucleation and film growth. The three interfacial energies are γ_{sv} (substrate-vapor), γ_{sf} (substrate-film) and γ_{fv} (film-vapor).

(a) General CVD Process

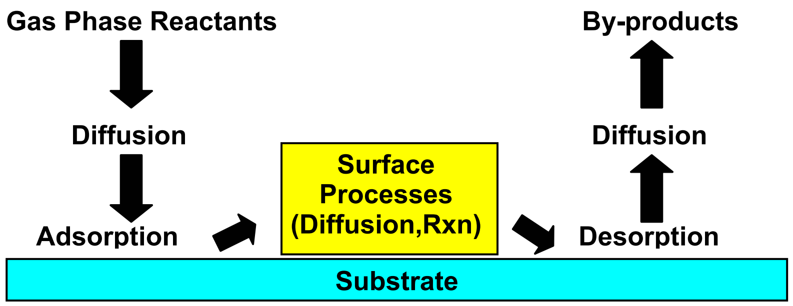

(b) Molecular Pathways in CVD

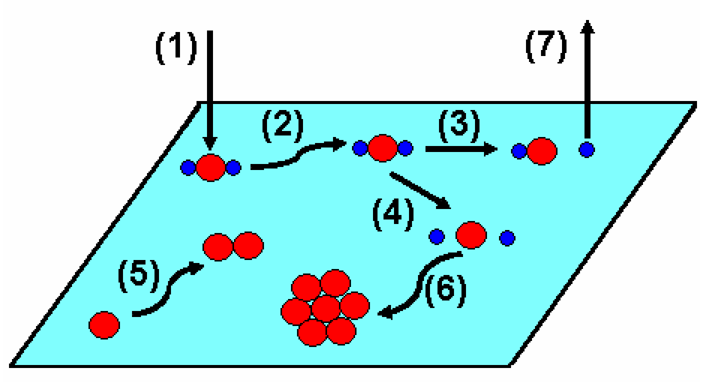

Illustration 1.4. Diagram of CVD processes a) depicting the general process including diffusion, adsorption, reaction, and desorption and b) the molecular pathways that lead to nucleation in CVD, including (**1**) diffusion of gas phase precursor molecule to surface, (**2**) surface diffusion, (**3**) partial dissociation of molecule, (**4**) complete dissociation of molecule to form adatom, (**5**) creation of a critical cluster by adatom surface diffusion, (**6**) addition of adatom to stable cluster, and (**7**) diffusion of reaction by-products away from surface.

Critical clusters are stable in that another adatom usually arrives before the cluster decays. Once a critical cluster has been formed, nucleation for that cluster is complete and growth of the cluster commences. Conversely, subcritical clusters may decay by loss of adatoms (to both the gas phase and other clusters) and are in local equilibrium with the surrounding adatom population. Although the number of critical clusters that form is influenced by process conditions, such as deposition rate and substrate temperature, the number of active sites on the substrate ultimately determines the adatom population.

In reality, the CVD process is complicated by adatoms and precursor ligand fragments from reaction by-products, which often get incorporated into the films as contamination. Illustration 1.5 depicts the CVD process for a single-source precursor [35], which shows that nucleation of the desired adatom is often accompanied by additional, undesired atoms and/or molecules that deposit on the surface as well. These contaminants may influence nucleation by blocking active sites on the substrate surface.

Nucleation is affected by both the quantity and nature of active sites on the surface and the reactivity of the precursor toward the surface. The number of active sites that are present on the substrate is determined by the chemical and physical properties of the surface, such as the type of substrate bonding, the quantity and type of functional groups, and the quantity and type of defects. The type of bonding, electron density, and electronegativity of the surface atoms influence their ability to be active nucleation sites. For example, Ru nucleates more readily on the ionic surfaces TiO_2 and Ta_2O_5, as compared with the covalent surfaces Si_3N_4, TiN, and SiO_2 [22]. In the case of ionic substrates, electron density from the surface is available to bond with the Ru precursor and precursor adsorption occurs readily. A strong precursor-surface complex is formed,

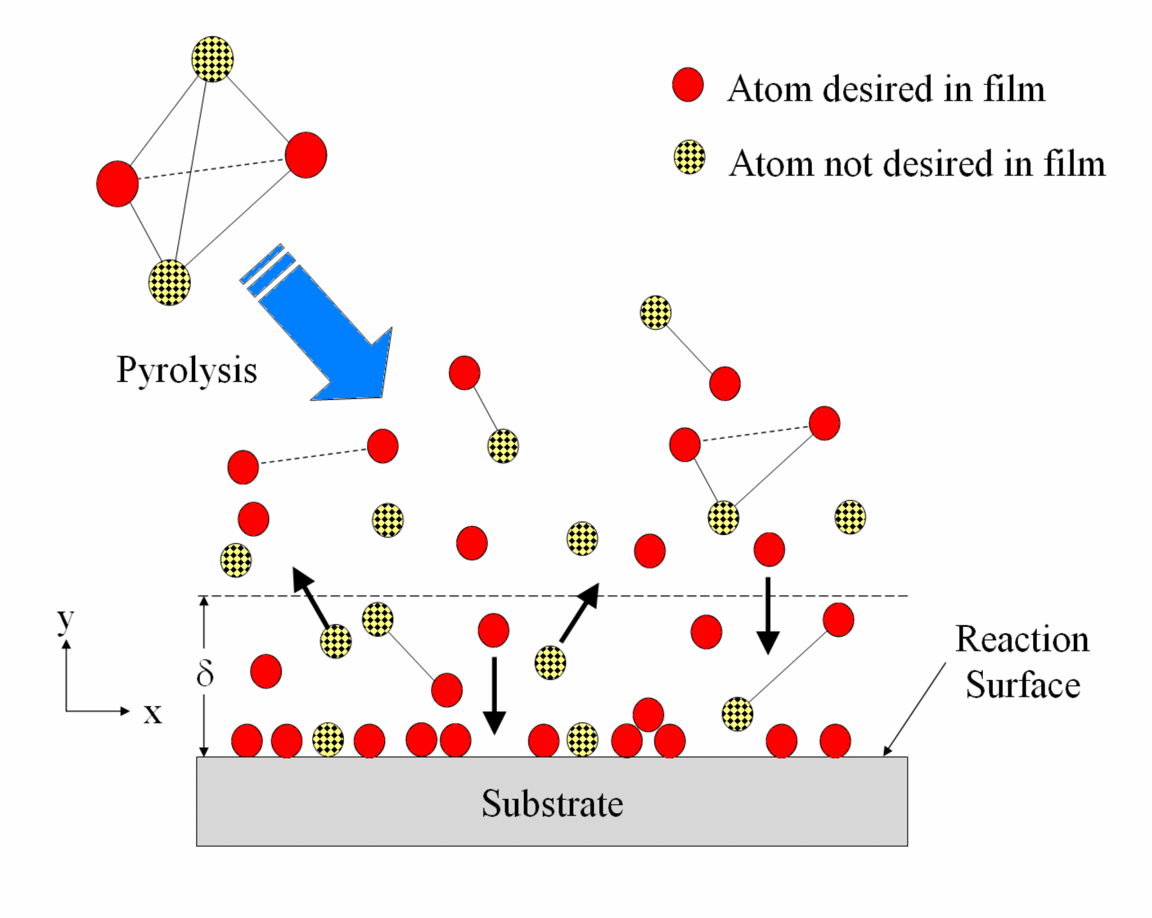

Illustration 1.5. Diagram of the CVD process for a single-source precursor, showing that nucleation of the desired adatom is often accompanied by additional, undesired atoms and/or molecules that deposit on the surface as well, taken from [35].

enhancing nucleation. For covalent surfaces, little electron density is available from the surface and adsorption of the Ru precursor is diminished, resulting in poorer nucleation.

The quantity and type of functional groups on the surface influences nucleation in much the same way as the type of substrate bonding. Surfaces with functional groups that are capable of bonding with Ru precursors, such as –OH groups, show better nucleation than surfaces with terminating $–CH_3$ groups. For instance, Ru films deposited on low-k dielectrics enriched with –OH groups showed good nucleation. However, if the low-k dielectric is silylated and all –OH groups are replaced with $–CH_3$ groups, no nucleation or film growth occurs at all [36].

The quantity and type of defects present on the surface include point defects (vacancies, substitutions, interstitial atoms) and line defects (dislocations that create terraces, steps, and kinks) [37]. Defects are known to increase the surface energy of the substrate and nucleation of critical clusters occurs more readily at defects such as steps and kinks. For example, the nucleation of WN_xC_y is better on 4° miscut Si(111) than on Si(100) [35]. When Si(111) is miscut, the number of dangling bonds, as well as terraces, steps, and kinks, increases due to the formation of vicinal surfaces. These defects add additional active sites for nucleation.

Furthermore, nucleation is influence by the reactivity of the precursor. Precursor reactivity is primarily governed by the ability of the ligands to dissociate intact from the metal center. Attempts to tailor the reactivity of CVD precursors involve issues such as altering the metal-ligand bond dissociation energy and/or increasing the reactivity of a ligand towards a surface. The metal-ligand bond strength should not be low enough to allow precursor dissociation in the gas phase and should not be high enough to require excessive deposition temperatures [38,39]. In addition, the ligands should cleave from the metal center due to reaction with the substrate surface, but be stable enough to dissociate intact without incorporating carbon or other contaminants into the growing film. Generally, precursor reactivity impacts nucleation when the precursor is relatively inert to the substrate surface, which causes sparse nucleation and a long incubation time at the onset of growth.

1.2.2.2 Modifying Nucleation

Attempts to modify nucleation usually involve altering the quantity and nature of active sites on the substrate surface or influencing the reactivity of the precursor toward either the substrate surface or the growing film. Efforts to increase the quantity and alter the nature of active sites on the substrate surface have included the addition of seed layers or the use of plasma pre-treatments.

Seed layers, such as Ru or Pd, are sputtered onto inert substrates, such as SiO_2, TiN and TaSiN, to improve nucleation [18,24,40]. Metallic seed layers provide electron density that contributes to enhanced adsorption and dissociation of Ru precursors and co-reactants. Another technique that may alter both the physical and chemical properties of the surface involves using plasma to pre-treat the substrate prior to film growth. Ar, H_2 and O_2 plasma pretreatments all improve the nucleation behavior of Ru films on TiN and SiO_2 [29,41,42]. The improvements in nucleation are likely due to multiple effects. Plasma treatments clean the substrate and remove adsorbed passivating molecules, such as hydrocarbons, which exposes additional surface sites. Furthermore, ion bombardment can introduce new active sites in the form of defects, which result from ion damage [40,41]. In the case of TiN, plasma treatment results in the removal of nitrogen atoms from the substrate surface, which makes the surface more metallic (and less covalent), leading to improvements in nucleation [42].

Attempts to influence the reactivity of the precursor involve either making the precursor more reactive to the substrate surface or altering the reactivity of the precursor toward the growing film. One example of modifying precursor reactivity toward the substrate involves increasing the reactivity of the ligands. The precursor $Ru(EtCp)_2$ (EtCp = ethylcyclopentadienyl) is known to exhibit very poor nucleation on oxide surfaces [18,20,27]. The EtCp ligand is a very stable closed-ring aromatic pentadiene, which does not adsorb or dissociate easily. In an attempt to improve the reactivity of $Ru(EtCp)_2$, a derivative was synthesized that replaces one of the EtCp ligands with the more reactive DMPD ligand (DMPD = 2,4-dimethylpentadienyl). The DMPD ligand is a linear aromatic pentadiene, which is much less stable than the EtCp ligand. This precursor, Ru(DMPD)(EtCp) or DER, has been shown to produce smaller, more dense nuclei with reduced incubation times, as compared with $Ru(EtCp)_2$ [30,31,43]. The improvements in nucleation are attributed to the more reactive DMPD ligand.

The majority of the research presented here (Chapters 2 and 3) will focus on the use of DER as a potential CVD Ru precursor. Although nucleation of films from DER is enhanced as compared with $Ru(EtCp)_2$, the improvements in nucleation are not sufficient to result in the ultra-thin, smooth Ru films needed for the liner. For this reason, attempts have been made to influence the reactivity of the DER precursor and O_2 co-reactant by altering reactivity toward the growing film (Chapter 3).

1.3 OBJECTIVE AND CHAPTER OVERVIEW

The goal of the research presented here is to evaluate precursor chemistry for Ru CVD, apply this chemistry to grow films, and to characterize the films for use in the liner material in integrated circuits. Surface science and film growth results reveal that DER is a potential precursor for Ru CVD, and nucleation and film properties can be improved by the addition of methyl iodide (Chapters 2 and 3). In addition, use of the $Ru_3(CO)_{12}$ precursor results in thin, ultra-smooth films, which are good candidates for inclusion in the liner (Chapter 4). Summarizing commentary and suggestions for future work are presented in Chapter 5.

In Chapter 2, an X-ray photoelectron spectroscopy (XPS) and temperature programmed desorption (TPD) study of DER on polycrystalline Ta is presented. DER exposures to Ta at 140 K result in primarily molecular adsorption and desorption, while a minor surface reaction occurs at defect sites. Monolayer DER desorbs between 278 and 297 K with increasing coverage, exhibiting a first order, zero coverage desorption energy of 2.3 eV. Multilayer DER desorbs between 272 and 263 K, most likely with fractional order kinetics, and exhibits a zero coverage desorption energy of 0.9 eV. Because multilayer growth occurs well before saturation of the monolayer, layer-by-layer (2D) and Strankski-Krastanov (SK) growth modes can be ruled out. DER is adsorbing in the form of 3D molecular islands; however, island formation can be governed by either the relative strength of molecule-substrate and intramolecular interactions, or islands may arise due to the random formation of 3D “hit and stick” structures, which develop due to the lack of adsorbate mobility at sufficiently low substrate temperatures. Because the monolayer desorption energy (2.3 eV) is higher than that of the multilayer (0.9 eV), intramolecular interactions are not stronger than molecule-substrate interactions, and the islanding of DER is due the formation of 3D hit and stick structures that result from lack of adsorbate mobility at 140 K. The validity of this growth model is verified by annealing experiments. XPS Ru 3d binding energies (BE) increase with increasing coverage due to core hole screening in the monolayer regime and increasing sample charging as the DER overlayer becomes thicker in the multilayer regime. XPS predicts the molecular DER overlayer thickness to be ~ 10.5-14.5 nm for exposures of 1.3-38.1 L. DER exposures to Ta between 298-773 K result in minor decomposition resulting primarily in adsorbed hydrocarbon species on the surface. The XPS BE decreases with increasing temperature, indicating that the amount of molecular dissociation increases with temperature. However, the BE never reaches that of metallic Ru, indicating that the DER cannot fully decompose by thermal means alone. When the Ta is pre-covered with atomic iodine, DER dissociation is significantly decreased while adsorption is increased. At room temperature, on bare Ta, only minor adsorption and dissociation occurs. At room temperature, on I/Ta, DER adsorbs molecularly. The atomic iodine blocks active sites on the Ta (reducing dissociation) and increases the sticking coefficient.

Chapter 3 describes CVD of Ru films from DER and O_2, which was carried out both with and without CH_3I addition. The addition of CH_3I during film growth results in chemisorbed iodine on the growing Ru film, but has no effect on the SiO_2 substrate. CH_3I is known to dissociate into adsorbed CH_3 and I on Ru, and the CH_3 groups desorb as methane below room temperature, while the adsorbed I is stable > 1000 K [48,49]. CH_3I is inert to the SiO_2 surface [50]. For films grown both with and without CH_3I addition, XPS results indicate ~ 7% oxygen and ~ 7% carbon contamination; therefore, the addition of CH_3I does not significantly increase the amount of carbon in the films. XPS also indicates that adsorbed iodine segregates through the film to the surface during growth, resulting in a continuously depressed deposition rate. Scanning electron microscopy (SEM) images show that the addition of CH_3I more than doubles the number of islands on the surface, and the improvement in nucleation results in smaller-grained, smoother films. Atomic force microscopy (AFM) indicates that the roughness of all films grown with CH_3I is decreased from that of films not grown with CH_3I; for instance, the roughness of 60 nm films decreased from 8.42 to 5.62 nm for no CH_3I and CH_3I addition, respectively. During nucleation, the adsorbed iodine stunts the growth of the initially-formed islands, allowing time for additional nucleation to occur on the SiO_2 surface. The iodine is active throughout the entire film deposition because it segregates through the film during growth. The role of iodine during nucleation and film growth is primarily to block O_2 adsorption and dissociation sites, which reduces the oxygen supply available to decompose the ligands of the DER precursor. Furthermore, the surface science studies described in Chapter 2 indicate that adsorbed iodine also increases DER adsorption (which may block additional active sites available for O_2 adsorption and dissociation), and decreases DER dissociation, which may also contribute to the stunted nucleation and depressed growth rate.

Chapter 4 presents a comparison of CVD Ru films deposited using $Ru_3(CO)_{12}$ as the precursor with PVD Ru films. Typically PVD films are smoother because PVD follows a 2D growth mode, while CVD films are rougher because CVD follows a 3D growth mode. In this study, AFM indicates that the CVD Ru films are very smooth, with roughness values ranging from 0.40-0.63 nm for film thicknesses of 9-28 nm. The PVD films are also smooth, with roughness values ranging from 0.11-3.36 nm for film thicknesses of 3.5-50 nm; however, the CVD films are smoother than those from PVD. SEM analyses indicate that the CVD films have a very smooth surface topography, and cross-sectional images show little to no columnar grain structure. The PVD films have a rougher surface topography that shows cracking due to residual stress in the films, and cross-sectional images show significant polycrystalline columnar grain structure. During CVD growth, Ru is deposited on the heated chamber, and the reaction by-product CO desorbs from the walls. Thus, deposition of metallic Ru on the SiO_2 substrate occurs in an atmosphere of both $Ru_3(CO)_{12}$ precursor and CO. There is a competition for adsorption sites between CO and the $Ru_3(CO)_{12}$ precursor. During deposition, the CO stunts the growth of the initially-formed Ru islands, allowing additional nucleation to occur on the SiO_2 surface, and CO continues to block active sites throughout the entire deposition. CO poisoning results in ultra-smooth Ru films with an average grain size $<$ 10 nm. In addition, Nilsen et al. have published a series of articles on the simulation of the growth of thin films from various seed objects, such as spheres, cubes, octahedra, truncated cubes, and tetragonal crystallites [44-47]. The shape of the different seed objects, or nuclei, that form are determined by the different growth precursors used and/or the crystal structure of the evolving material. Nilsen et al. have shown that the different types of crystal shapes forming each island during nucleation significantly impact both growth dynamics and the topography and surface roughness of the resulting films. This chapter will also address the shape of the seed objects and the resulting topography and surface roughness of CVD Ru and RuO_2 films. It is shown that the experimental roughness values of these films support the order of surface roughness predicted by Nilsen et al. based on seed object and the resulting topography.

1.4 REFERENCES

[1] International Technology Roadmap for Semiconductors, 2007 Edition, http://public.itrs.net (2007).

[2] G. E. Moore, Electronics 38 (1965) 114.

[3] C. Whitman, M. M. Moslehi, A. Paranjpe, L. Velo, T. Omstead, J. Vac. Sci. Technol. A 17 (1999) 1893.

[4] C.-K. Hu, Mat. Res. Soc. Sym. Proc. 511 (1998) 305.

[5] M. T. Bohr, Tech. Dig., Int. Electron Devices Meet. (1995) 241.

[6] H. Kim, Surf. Coating Technol. 200 (2006) 3104.

[7] S. P. Murarka, S. W. Hymes, Crit. Rev. Solid State Mat. Sci. 20 (1995) 87.

[8] L. Peters, Semiconductor International 24 (2001) 66.

[9] B. Zhao, M. Brongo, Mat. Res. Soc. Symp. Proc. 564 (1999) 485.

[10] A. E. Kaloyeros, E. Eisenbraun, Ann. Rev. Mat. Sci. 30 (2000) 363.

[11] M. W. Lane, C. E. Murray, F. R. McFeely, P. M. Vereecken, R. Rosenburg, Appl. Phys. Lett. 83 (2003) 2330.

[12] A. Kohn, M. Eizenberg, Y. Shacham-Diamond, Appl. Surf. Sci. 212 (2003) 367.

[13] I. Goswami, R. Laxman, Semicond. Int. 27 (2004) 49.

[14] O. Chyan, T. N. Arunagiri, T. Ponnuswamy, J. Electrochem Soc. 150 (2003) C347.

[15] J. Shin, A. Waheed, W. A. Winkenwerder, H.-W. Kim, K. Agapiou, R. A. Jones, G. S. Hwang, J. G. Ekerdt, Thin Solid Films 515 (2007) 5298.

[16] L. B. Henderson, J. G. Ekerdt, Thin Solid Films 517 (2009) 1645.

[17] C.-C. Yang, T. Spooner, S. Ponoth, K. Chanda, A. Simon, C. Lavoie, M. Lane, C.-K. Hu, E. Liniger, L. Gignac, T. Shaw, S. Cohen, F. McFeely, D. Edelstein, Proc. IEEE International Interconnect Tech. Conf. (2006) 187.

[18] J. Papadatos, S. Consiglio, S. Skordas, E. T. Eisenbraun, A. E. Kaloyeros, J. Peck, D. Thompson, C. Hoover, J. Mater. Res. 19 (2004) 2947.

[19] P. G. Ganesan, M. Eizenberg, C. Dornfest, J. Electrochem. Soc. 149 (2002) G510.

[20] Y. Matsui, M. Hiratani, T. Nabatame, Y. Shimamoto, S. Kimura, Electrochem. Solid-State Lett. 4 (2001) C9.

[21] K. C. Smith, Y.-M. Sun, N. R. Mettlach, R. L. Hance, J. M. White, Thin Solid Films 376 (2000) 73.

[22] S. Y. Kang, C. S. Hwang, H. J. Kim, J. Electrochem. Soc. 152 (2005) C15.

[23] K. Choi, J. Lim, S. Roy, C. Lee, Jpn. J. Appl. Phys 42 (2003) 5539.

[24] H. Han, J. J. Kim, D. Y. Yoon, J. Vac. Sci. Technol. A 22 (2004) 1120.

[25] H. Marom, M. Eizenberg, J. Appl. Phys. 99 (2006) 123705.

[26] W. Tang, K. Xu, P. Wang, X. Li, Microelectronic Eng. 66 (2003) 445.

[27] T. Aaltonen, P. Alen, M. Ritala, M. Leskela, Chem. Vap. Deposition 9 (2003) 45.

[28] K. J. Park, J. M. Doub, T. Gougousi, G. N. Parsons, Appl. Phys. Lett. 86 (2005) 051903.

[29] S. Y. Kang, K. H. Choi, S. K. Lee, C. S. Hwang, H. J. Kim, J. Electrochem. Soc. 147 (2000) 1161.

[30] T. Shibutami, K. Kawano, N. Oshima, S. Yokoyama, H. Funakubo, Electrochem. Solid-State Lett. 6 (2003) C117.

[31] T. Shibutami, K. Kawano, N. Oshima, S. Yokoyama, H. Funakubo, Mat. Res. Soc. Symp. Proc. 748 (2003) 111.

[32] J. J. Kim, D. H. Jung, M. S. Kim, S. H. Kim, D. Y. Yoon, Thin Solid Films 409 (2002) 28.

[33] J. J. Kim, M. S. Kim, D. Y. Yoon, Chem. Vap. Deposition 9 (2003) 105.

[34] J. A. Venables, Introduction to Surface and Thin Film Processes (2000).

[35] O. J. Bchir, Ph.D Dissertation, The University of Florida (2004).

[36] J. Heo, S.-J. Won, D. Eom, S. Y. Lee, Y. B. Ahn, C. S. Hwang, H. J. Kim, Electrochem Solid-State Lett. 11 (2008) H210.

[37] L. H. Van Vlack, Elements of Materials Science and Engineering, 6th Ed. (1990).

[38] O. J. Bchir, K. M. Green, M. S. Hlad, T. J. Anderson, B. C. Brooks, C. B. Wilder, D. H. Powell, L. McElwee-White, J. Organometallic Chem. 684 (2003) 338.

[39] O. J. Bchir, K. M. Green, H. M. Ajmera, E. A. Zapp, T. J. Anderson, B. C. Brooks, L. L. Reitfort, D. H. Powell, K. A. Abboud, L. McElwee White, J. Am. Chem. Soc. 127 (2005) 7825.

[40] J. Lim, H. Park, C. Lee, Thin Solid Films 475 (2005) 194.

[41] S.-E. Park, H.-M. Kim, K.-B. Kim, S.-H. Min Electrochem. Solid-State Lett. 1 (1998) 262.

[42] K. Choi, J. Lim, S. Roy, C. Lee, Jpn. J. Appl. Phys. 42 (2003) 5539.

[43] S. K. Kim, S. Y. Lee, S. W. Lee, G. W. Hwang, C. S. Hwang, J. W. Lee, J. Jeong, J. Electrochem. Soc. 154 (2007) D95.

[44] O. Nilsen, O. B. Karlsen, A. Kjekshus, H. Fjellvåg, Thin Solid Films 515 (2007) 4527.

[45] O. Nilsen, O. B. Karlsen, A. Kjekshus, H. Fjellvåg, Thin Solid Films 515 (2007) 4538.

[46] O. Nilsen, O. B. Karlsen, A. Kjekshus, H. Fjellvåg, Thin Solid Films 515 (2007) 4550.

[47] O. Nilsen, O. B. Karlsen, A. Kjekshus, H. Fjellvåg, J. Crystal Growth 308 (2007) 366.

[48] Y. Zhou, M. A. Henderson, W. M. Feng, J. M. White, Surf. Sci. 224 (1989) 386.

[49] A. Kis, J. Kiss, F. Solymosi, Surf. Sci. 459 (2000) 149.

[50] K. C. McGee, M. D. Dreissen, V. H. Grassian, J. Catal. 159 (1996) 69.

Chapter 2: Surface Chemistry of (2,4-dimethylpentadienyl)(ethylcyclopentadienyl)Ru on Polycrystalline Ta

2.1. INTRODUCTION

Organometallic precursors have been extensively studied for the chemical vapor deposition (CVD) of thin metallic films for microelectronic applications. Ultra-thin Ru films are currently being explored as a potential liner material in integrated circuits [1]. CVD is an attractive film deposition technique because the non-directional nature of the reactant gas flux at the substrate surface allows conformal deposition in high aspect ratio features. Ru has several properties that make it a desirable material in semiconductor devices, such as low electrical resistivity, high thermal stability, high chemical stability in the presence of oxygen and water, and negligible solubility with copper [1].

CVD Ru films have been deposited using a number of organometallic precursors, including the carbonyl-containing compounds, such as $Ru_3(CO)_{12}$ [2,3]; β-diketonate complexes, such as $Ru(dpm)_3$ (dpm = dipivaloylmethanate) [4]; pyrazolate-containing compounds, such as $Ru(CO)_3$(3,5-bis(trifluoromethyl) pyrazole) [5]; and the family of compounds containing cyclopentadienyl and pentadienyl ligands, such as $Ru(Cp)_2$ (Cp = cyclopentadienyl) [6,7], $Ru(EtCp)_2$ (EtCp = ethylcyclopentadienyl) [8,9], and $Ru(DMPD)_2$ (DMPD = 2,4-dimethylpentadienyl) [10]. All of the aforementioned precursors are solid at room temperature, except for $Ru(EtCp)_2$. The use of solid precursors in CVD presents several difficulties, including problems with delivery due to high melting point and low vapor pressure. $Ru(EtCp)_2$ has received attention because it is a liquid at room temperature with a high vapor pressure; however, this precursor has presented several drawbacks, such as poor nucleation on oxide and nitride substrates, which results in a long incubation time at the onset of film growth [11]. In an attempt to improve the reactivity of $Ru(EtCp)_2$ towards oxide and nitride substrates, a derivative has been synthesized that replaces one of the EtCp ligands with the more reactive DMPD ligand. This precursor, Ru(DMPD)(EtCp), also called DER, is a highly volatile liquid. Recent film growth studies indicate that the DER precursor deposits films with better characteristics than $Ru(EtCp)_2$. DER results in a higher nucleation density, a lower incubation time, and smoother films as compared with $Ru(EtCp)_2$ [12,13]; it is believed that the higher reactivity of the DMPD ligand versus the EtCp ligand has resulted in these improved properties [14]. Although film growth studies with DER show promising results, the surface chemistry of DER is largely unexplored.

Futhermore, attempts have been made to improve the nucleation and film properties of CVD Ru films deposited with $Ru(EtCp)_2$. One such attempt by Kim et al. [15,16] involved the introduction of an iodine source (i.e., CH_3I, C_2H_5I) during film growth. These researchers expanded on the work of Hwang et al. [17,18] who showed that during Cu CVD, iodine acted as a catalytic surfactant to reduce surface roughness, in a manner similar to surfactant addition in homo- and heteroepitaxy. Kim et al. also observed that iodine addition impacts CVD Ru films; adsorbed iodine results in smaller, denser nuclei, which leads to films with smaller grain size and improved film roughness [15,16].

Hwang et al. have shown that the particular iodine source being used is not significant, as long as the iodine-containing molecule leaves only adsorbed iodine on the growing film surface. For example, CH_3I dissociates on Cu into adsorbed methyl groups and iodine atoms. Above 400 K, the methyl groups decompose to evolve methane, ethylene, propylene, and ethane, while the adsorbed iodine is stable up to 950 K [19]. Similarly, CH_3I dissociates into adsorbed methyl groups and iodine atoms on Ru(001); although the only gas that desorbs is methane, the majority of which evolves at 170 K [20]. Adsorbed iodine is stable on the Ru surface up to 1080 K [21]. Furthermore, while the iodine source dissociatively adsorbs on the metal film surface, it is inert to the oxide or nitride substrate. The influence of iodine on CVD film growth is an interesting result, and this motivates the study reported herein on the interaction of DER with adsorbed iodine.

This chapter presents X-ray photoelectron spectroscopy (XPS) and temperature programmed desorption (TPD) studies of the organometallic CVD Ru precursor DER adsorbed on a polycrystalline Ta substrate, both on bare and iodine pre-covered Ta. CVD Ru films have been deposited on a variety of substrates including oxides, nitrides, and other metals. A Ta substrate was chosen for this work because Ta is metallic and is utilized in various microelectronic applications, including the Ta/TaN bi-layer used as a Cu diffusion barrier [1]. TPD is often used to investigate phenomena such as molecular versus dissociative adsorption, adsorbate growth mode, sticking coefficient, and issues concerning desorption kinetics, including reaction order, desorption energy and the presence of lateral molecular interactions. TPD is used herein to address these topics for DER on Ta. XPS allows the determination of adsorbate binding energies and overlayer thicknesses. Binding energy (BE) shifts can be attributed to initial-state effects, final state effects such as core hole screening, or sample charging [22]. It will be shown herein that both core hole screening and sample charging impact the BE shifts of DER on Ta.

The majority of this work focuses on molecular DER adsorption and desorption, although a minor surface reaction that most likely occurs at defect sites will be addressed.

2.2 EXPERIMENTAL DETAILS

Experiments were conducted in an ultra-high vacuum system, described in detail elsewhere [23]. The system is equipped with a cryogenic pump, used to maintain a base pressure of 5.0×10^{-10} torr, and a diffusion pump, used during gas dosing and surface analysis, which maintains a base pressure of 1.0×10^{-9} torr. XPS was conducted on a Perkin Elmer PHI 5000C ESCA system using a non-monochromatic Al Kα x-ray source. The XPS system is not equipped for charge neutralization (i.e., no electron flood gun). TPD was conducted on an Extrel C50 quadrupole mass spectrometer. Up to eight mass to charge (*m/z*) signals could be monitored during each TPD analysis. Curve fitting of the XP spectra was carried out using Shirley background subtraction and Gaussian/Lorentzian peak shapes. TPD spectra were also fit using Gaussian/Lorentzian peaks.

A 13 mm × 15 mm piece of 0.025-mm thick Ta foil (Electronic Space Products International, 3N8 grade) was used as the substrate, and it could be cooled by liquid N_2 to 120 K and heated resistively to 1273 K. The sample was cleaned in-between experiments by 5 keV Ar^+ ion sputtering followed by a 10 min anneal at 1073 K to heal the ion damage. Surface cleanliness was verified by confirming that the C 1s XPS signal was below the noise level. As evidenced by XPS, the Ta surface was slightly oxidized to a Ta_xO_y, which could not be removed even after repeated sputter clean and annealing cycles. A pure, oxygen-free Ta surface can only be achieved in UHV by annealing to 2800 K [24], which exceeds the high-temperature limit of our system.

DER was supplied by Tosoh Corp. and was delivered into the chamber using an uncalibrated pinhole doser. The Ta substrate was positioned ~ 0.5 cm away from the doser tube. Because the vapor pressure of DER is sufficiently high (0.04 torr at 333 K) [25], the saturator was kept at room temperature and no heating was necessary to deliver the precursor. In order to minimize variations in precursor delivery, the DER saturator was pumped by a turbomolecular pump for 10 min prior to dosing, and then the valve between the pump and the saturator was closed. The valve between the saturator and chamber was opened next for a set amount of time to control the exposure. CH_3I (Sigma-Aldrich, 99.5%) was introduced using a leak valve. Because of its high vapor pressure (~ 400 torr at 298 K) [15], the CH_3I saturator was kept at room temperature and no heating was required for delivery. Gas exposures were calculated in Langmuir ($1\ L = 1 \times 10^{-6}$ torr s) by integrating chamber pressure versus time and subtracting out the chamber base pressure, in a manner similar to that described in Ref. 26.

In the experiments involving low temperature DER adsorption (no CH_3I), DER was dosed to the Ta foil held at 140 K, followed by XPS analysis, TPD over the temperature range 145-973 K, and then a final XPS analysis after TPD. It is known that irradiation effects from the XPS process can alter the physical and chemical properties of an overlayer film [27]. In order to verify that the XPS process did not alter the TPD data for DER on Ta, several TPD spectra were taken without XPS being acquired first. No differences were observed in the TPD spectra for DER overlayer films with and without prior XPS analysis.

2.3. RESULTS AND DISCUSSION

2.3.1 Molecular DER Adsorption and Desorption at 140 K

The TPD and XPS data described in this section show that the growth mode of DER on Ta is a result of the random formation of three-dimensional (3D) “hit and stick” structures. The growth of molecular adsorbates on surfaces are classified in the same manner as the growth of atomic solid films [28]. Layer-by-layer, or Frank-van der Merwe, growth occurs when molecule-substrate interactions are stronger than intramolecular interactions. Island, or Volmer-Weber, growth occurs when intramolecular interactions are stronger than molecule-substrate interactions. And finally, the Stranski-Krastanov (SK) growth mode arises when one or more molecular layers grow in layer-by-layer and then island growth occurs on top of the first molecular layer(s). In the case of DER on Ta, both the layer-by-layer and SK growth modes are ruled out because second layer desorption occurs well before saturation of the monolayer. Thus DER is adsorbing in the form of 3D molecular islands. However, it is worth noting that although island formation can be governed by the relative strength of molecule-substrate and intramolecular interactions, islands may also arise due to the random formation of 3D hit and stick structures [29], which develop due to the lack of adsorbate mobility at sufficiently low substrate temperatures.

2.3.1.1 TPD Following DER Adsorption on Ta at 140 K

TPD experiments reveal molecular DER desorption, along with a minor surface reaction involving desorption of the DER ligands. Masses corresponding to entities such as the intact ligands (*m/z* 77, 91, 94, 96), Ru (*m/z* 102), ligand or ligand fragments bonded to Ru (*m/z* 192, 194, 195, 197), and intact molecular DER (*m/z* 290) were monitored over the TPD range of 145-973 K. The majority of the monitored masses have spectra with the same features as the DER parent molecule and are attributed to ionization-induced fragmentation of DER in the mass spectrometer. For comparison purposes, the mass fragmentation pattern of the DER was determined in our system prior to TPD. Several of the monitored masses (*m/z* 77, 91, 94, 96) have small features that differ from that of molecular DER desorption and indicate ligand dissociation from the metal center. These minor dissociative surface reaction(s) are discussed in Section 2.3.2.

Fig. 2.1 shows a series of TPD spectra for molecular DER (*m/z* 290) as a function of increasing exposure. DER desorption is characterized by a single feature at 273 K for exposures up to 0.45 L, which splits into two peaks for exposures greater than 0.45 L. The peak that develops as the higher temperature feature saturates with increasing exposure and is attributed to first layer or monolayer desorption. The lower temperature peak does not saturate with increasing exposure and is assigned to second layer or multilayer desorption. The monolayer peak increases in temperature with increasing coverage, from 278 K at 0.64 L to 297 K at 24.8 L, while the multilayer peak decreases in temperature from 272 K at 0.64 L to 263 K at 6.1 L. The multilayer peak desorption temperature remains constant at 263 K for 6.1 and 24.8 L. For exposures of 0.85 L and greater, two peaks could be clearly distinguished and fit using Gaussian/Lorentzian peak shapes. For exposures of 0.85 to 3.6 L, the two peaks could be fitted giving an r^2 value of 0.99. For exposures of 6.1 and 24.8 L, the r^2 values were slightly lower, at 0.97 and 0.96, respectively.

Fig. 2.2 presents the uptake curves based on DER desorption from Ta. Fig. 2.2a shows the total TPD peak area including both peaks for the raw experimental data (not

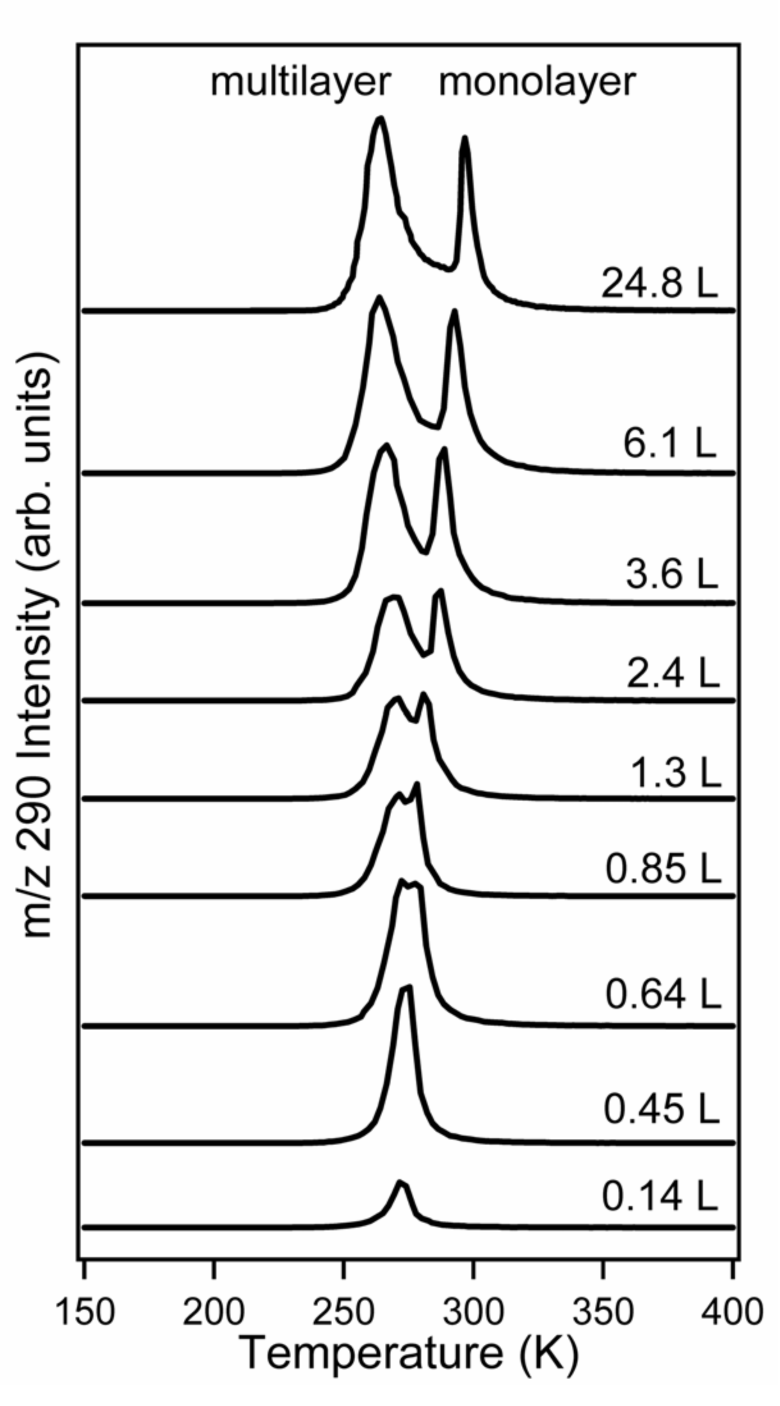

Figure 2.1. TPD spectra of DER (m/z 290) after adsorption on Ta at 140 K. The heating rate was 7 K/s.

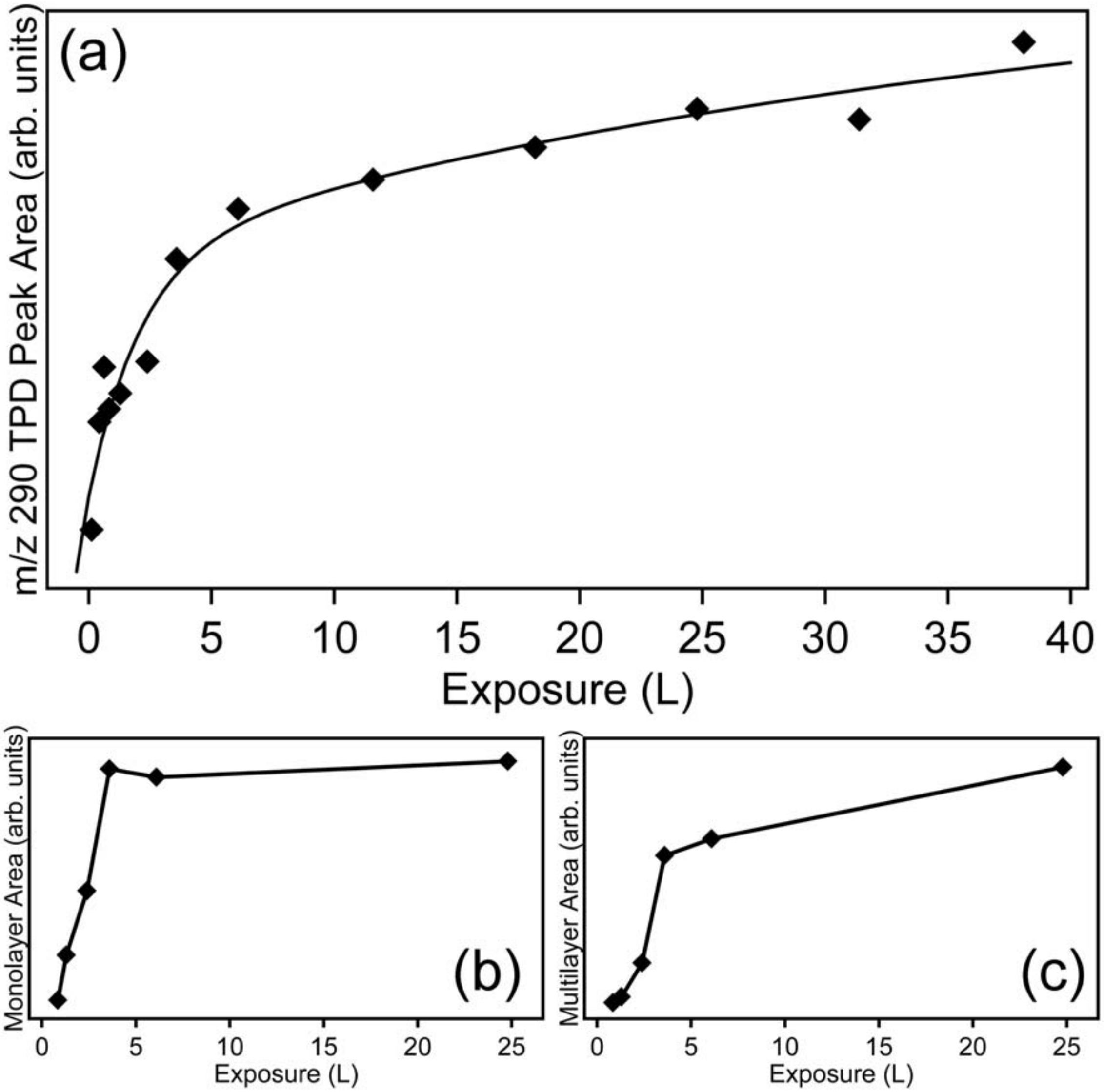

Figure 2.2. TPD uptake curves of DER after adsorption on Ta at 140 K for a) total TPD peak area including both peaks from the raw experimental data, b) monolayer TPD peak area from the fitted data, and c) multilayer TPD peak area from the fitted data.

the fit) as a function of increasing exposure. The TPD peak area increases sharply for exposures < 3.6 L and then increases more gradually thereafter for exposures > 3.6 L. For exposures of 3.6 L and greater, the uptake curve is linear. Fig. 2.2b and 2.2c show the TPD peak areas for the monolayer and multilayer peaks, respectively, using the fitted peaks. The monolayer peak area saturates at 3.6 L. The multilayer peak area increases abruptly for exposures up to 3.6 L and then increases in a more gradual linear fashion for exposures of 3.6 L and greater. The abrupt change in slope is most likely related to the sticking coefficient of DER.

The sticking coefficient for adsorbed molecules on surfaces typically drops once the saturated monolayer is complete and multilayers begin to form. The sticking coefficient begins to level-off at the coverage where arriving molecules can no longer make contact with the bare surface [30] and a change in sticking coefficient is usually indicated by a change in slope of the uptake curve, such as that reported for molecular nickelocene desorbing from Ag(100) [31]. In the case of DER on Ta, it appears that the monolayer saturates and the sticking coefficient decreases at exposures of about 3.6 L. The sticking coefficient of DER on Ta is much larger than the sticking coefficient of DER on condensed DER. Once there are no more available adsorption sites for the DER on the Ta surface, the sticking coefficient decreases and the uptake curve increases more gradually with increasing exposure.

The multilayer feature in Fig. 2.1 appears well before the saturation of the monolayer peak, indicating that second layer growth occurs prior to the completion of a full monolayer. In fact, it is likely that the two peaks are present for the 0.45 L exposure as well, but are simply not discernible until higher coverages have been reached. The total peak area for the 0.45 L exposure is greater than the peak area associated with saturation of the monolayer, indicating that some multilayer desorption is occurring at 0.45 L. On the other hand, the total peak area for the 0.14 L exposure is significantly less than the peak area for saturation of the monolayer, indicating that at this exposure, it is possible that only monolayer DER is desorbing from the surface. However, for exposures of 1.3 to 24.8 L, the full width at half maximum (FWHM) of the monolayer peak is approximately constant at 7 K. The FWHM of the 0.14 L peak is ~ 8.5 K, which means that there may be some multilayer desorption even at 0.14 L.

The fact that the multilayer peak is evident at exposures as low as 0.45 L gives some insight into the growth mode of DER on Ta. Both the layer-by-layer and SK growth modes can be ruled out because second layer desorption occurs well before saturation of the monolayer. Thus DER is adsorbing in the form of 3D molecular islands. Island formation can be governed by the relative strength of molecule-substrate and intramolecular interactions and/or islands may arise due to formation of 3D hit and stick structures [29], associated with limited adsorbate mobility. Insight into island formation of DER on Ta can be found from the desorption kinetics.

The desorption kinetics of DER on Ta are somewhat complex. Typical multilayer desorption exhibits zero order kinetics in which the TPD spectra share a common leading edge and the desorption temperature increases with increasing coverage. However, it is not uncommon for multilayer desorption to follow fractional order kinetics, which occur due to desorption from 3D islands and is often observed when the multilayer peak appears before the monolayer is saturated. For example, fractional order multilayer desorption has been observed for naphthalene on Ag(111) [32] and methanol (CH_3OH)

on graphite [33]. For DER on Ta, the multilayer desorption peaks do not share a common leading edge, thus multilayer desorption is mostly likely of fractional order with desorption occurring from the islands. The fact that the multilayer desorption temperature decreases until a constant value is reached is somewhat unusual, but this same trend has been observed in the case of aluminum on Re, in which fractional order multilayer desorption kinetics were also observed [34]. Decreasing desorption temperature is often attributed to repulsive lateral molecular interactions (when second order desorption kinetics are not a consideration) and it is possible that repulsive intramolecular interactions are occurring in the DER islands. It has been shown that disorder in molecular overlayers may lead to repulsive interactions, as in the case of N_2 desorption from Ni(100) [35]. N_2 desorption showed weakly repulsive lateral interactions when the N_2 overlayer was disordered, but strongly attractive interactions were observed when the N_2 overlayer was ordered. It is possible that DER islands are forming due to random 3D hit and stick structures, which are highly disordered and lead to repulsive lateral interactions.

Multilayer DER desorption most likely follows fractional order kinetics with repulsive lateral interactions. Even though this assessment of reaction order has some uncertainty, the leading edge method can still be used to evaluate the multilayer desorption energy. The leading edge method can be applied in cases when the reaction order is unknown; however, its application relies on the assumption that the desorption energy is coverage independent. Assuming that the desorption energy does not depend on coverage is only valid at very low coverages in systems that have lateral intramolecular interactions [36]. The multilayer desorption energy was extrapolated back to the limit of zero coverage, as most methods for determining desorption energy from TPD spectra are found to be accurate if extrapolated back to the limit of zero coverage [37]. Fig. 2.3a shows the multilayer desorption energy as a function of exposure determined by the leading edge method for DER exposures of 1.3 L and greater. It appears that the desorption energy increases with increasing coverage (which would normally be attributed to attractive lateral interactions); however, this increasing trend in desorption energy may be due to error in using the leading edge method at higher coverages. It seems very unlikely that attractive lateral interactions occur in the DER multilayer, as the desorption temperature *decreased* with increasing coverage. Extrapolating the desorption energy back to the limit of zero coverage gives a multilayer desorption energy of 0.9 eV (87 kJ/mol). This value is in good agreement with the desorption energy for the organometallic precursor $Ru(EtCp)_2$, which forms clusters on an Al_2O_3 substrate held at 110 K and exhibits a desorption energy of 94 kJ/mol [38].

Monolayer desorption typically follows a coverage-dependent desorption rate (non-zero order) and is usually first order for non-dissociative molecular desorption. Typical first order desorption kinetics show a constant desorption temperature with increasing coverage; however, it is common for molecular adsorbates with attractive lateral interactions to show increasing desorption temperature with increasing coverage. Thus it appears that DER monolayer desorption is likely first order with attractive lateral interactions. Like the multilayer desorption case, this assessment of reaction order has some uncertainty; however, the leading edge method, which does not rely on a known reaction order, cannot be applied to the monolayer peaks because the leading edges are lost in the overlap with the multilayer peaks. Thus the method of Chan et al. (CAW) [39]

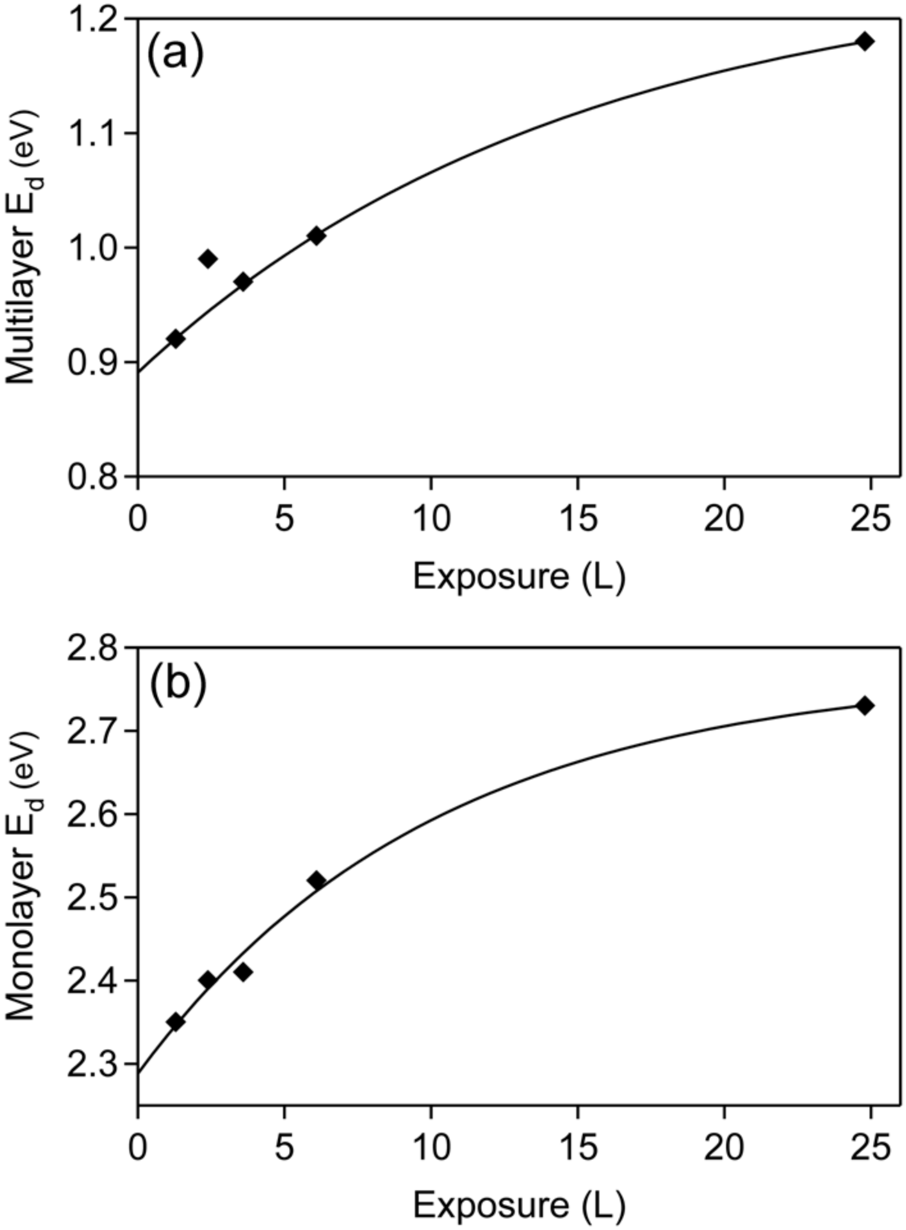

Figure 2.3. Desorption energy of DER on Ta at 140 K for a) fractional order multilayer desorption determined by the leading edge method and b) first order monolayer desorption determined by the CAW method. The lines were fit to an exponential function to facilitate extrapolation to the zero-coverage limit.

was applied using the assumption that monolayer desorption is first order. It has been shown that the CAW method gives highly inaccurate results at higher coverages for first order systems with attractive interactions; the desorption energy and the magnitude of the lateral interaction are greatly overestimated and even the type of interaction (attractive or repulsive) may be predicted incorrectly [37]. However, the CAW method does correctly predict the desorption energy in the limit of zero coverage [37]. Furthermore, the CAW method requires both the desorption temperature at the peak maximum and the FWHM. For DER monolayer desorption, the FWHM was determined from the fitted monolayer peaks.

Fig. 2.3b shows the monolayer desorption energy as a function of exposure determined by the CAW method for DER exposures of 1.3 L and greater. It appears that the desorption energy increases with increasing coverage; however, it was noted previously that the CAW method greatly overestimates both the desorption energy and magnitude of lateral interactions at higher coverages. Thus the trend of increasing desorption energy with increasing coverage is not taken as confirmation that attractive lateral interactions are present in the monolayer. The primary indication of attractive interactions is the increasing desorption temperature with increasing coverage. As was the case for the multilayer, the desorption energy has been extrapolated back to the limit of zero coverage, giving a monolayer desorption energy of 2.3 eV (222 kJ/mol). Similar first order monolayer desorption energies were reported for the large aromatic molecule $C_{54}H_{22}$ on graphite of 2.3 eV [40] and the straight chain alkane $H(CH_2)_{35}H$ on graphite of ~ 220 kJ/mol [41].

As mentioned previously, islanding of adsorbate molecules upon adsorption may occur because intramolecular interactions are stronger than molecule-substrate interactions or because random 3D hit and stick structures form due to the lack of adsorbate mobility at very low substrate temperatures. In the case of DER on Ta, the zero coverage desorption energies of the multilayer and monolayer are 0.9 and 2.3 eV, respectively. Because the monolayer desorption energy is higher than the multilayer desorption energy, intramolecular interactions are not stronger than molecule-substrate interactions. Thus the islanding of DER upon adsorption is most likely due to a low surface diffusion rate at the substrate temperature of 140 K, resulting in the formation of random hit and stick structures. The surface diffusion rate is most likely low at this temperature because the DER molecules are well chemisorbed. A similar phenomenon was observed for CH_3OH on graphite, in which the bonding of CH_3OH to the surface was stonger than that of one CH_3OH to another CH_3OH, but islanding was still observed [33]. The islanding was attributed to lack of CH_3OH mobility at the adsorption temperature of 105 K.

2.3.1.2 XPS Following DER Adsorption on Ta at 140 K

Fig. 2.4 shows Ru 3d XP spectra for DER molecules adsorbed on Ta as a function of increasing exposure. Because the Ru $3d_{3/2}$ and C 1s XPS peaks overlap, the Ru $3d_{3/2}$ peak relative to the Ru $3d_{5/2}$ peak is much larger than for a metallic Ru film due to the abundance of carbon in the DER molecule. The BE of both the Ru $3d_{3/2}$ and the Ru $3d_{5/2}$ peaks increase with increasing exposure. In order to examine this trend more carefully, the Ru $3d_{3/2}$ BE has been plotted in Fig. 2.5a as a function of increasing exposure (the Ru $3d_{5/2}$ BE follows the same trend). The inset in Fig. 2.5a shows that the BE of the Ru $3d_{3/2}$

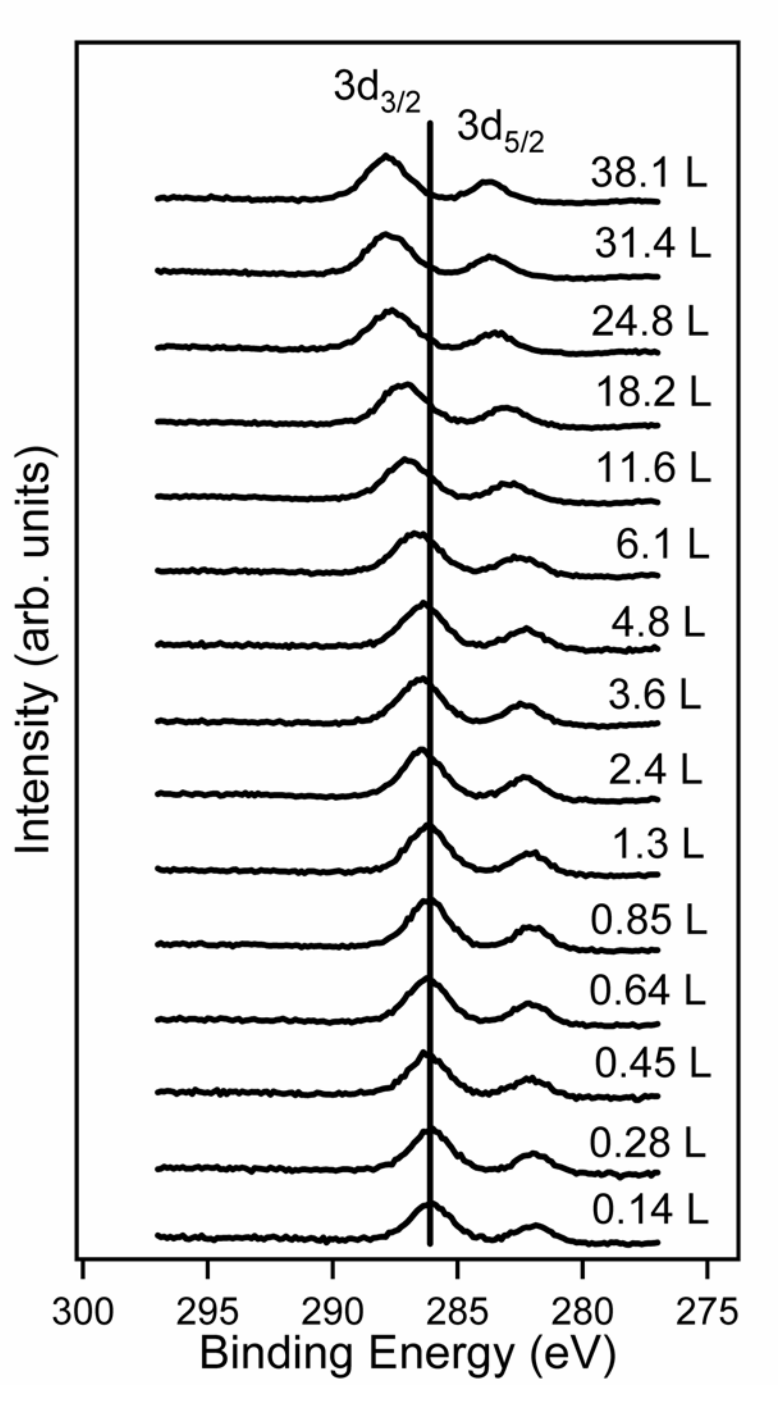

Figure 2.4. Ru 3d XP spectra of DER on Ta at 140 K. The line is shown to guide the eye.

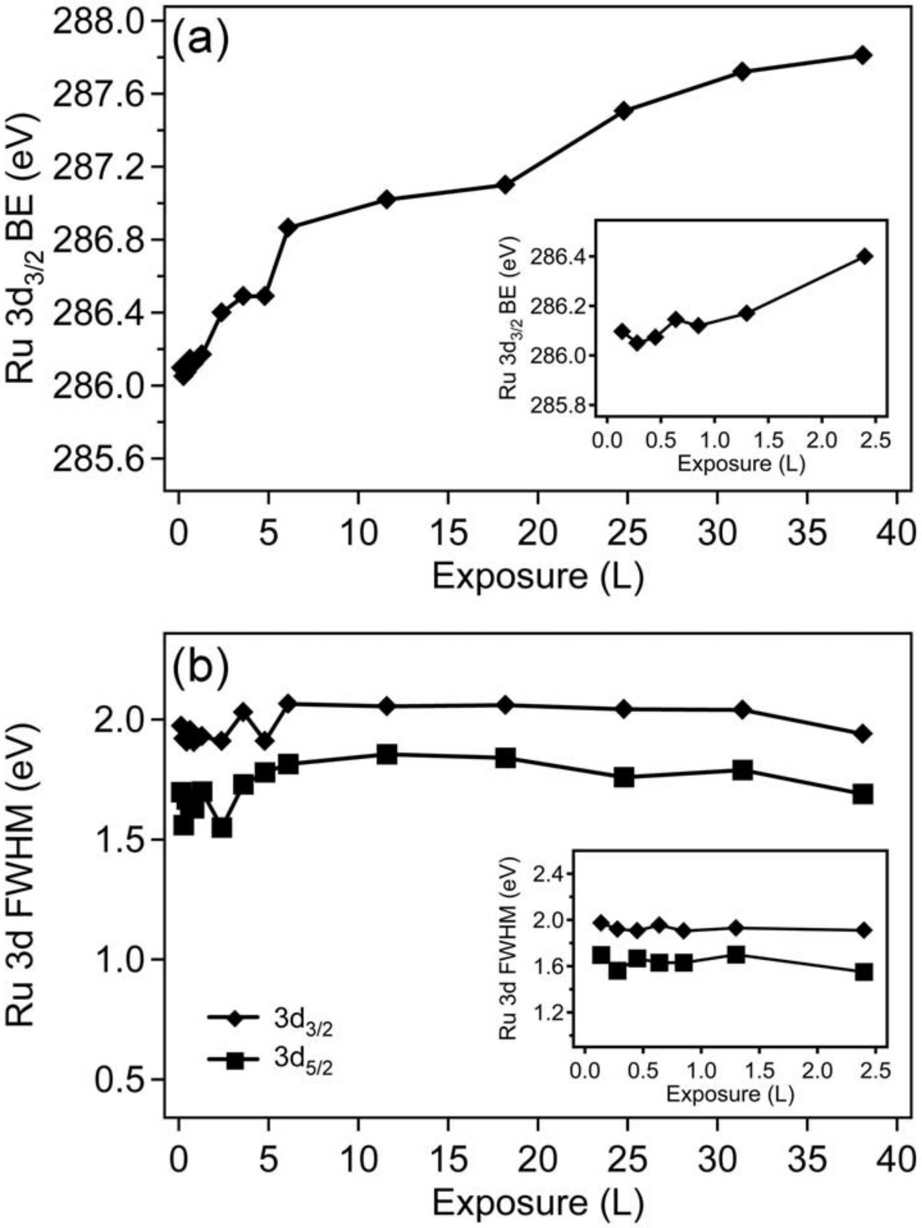

Figure 2.5. Ru 3d XPS data for DER on Ta at 140 K for the a) $3d_{3/2}$ BE and b) $3d_{3/2}$ and $3d_{5/2}$ FWHM both as a function of increasing exposure. The insets allow a more careful examination of the BE and FWHM at lower exposures.

peak is essentially constant at 286.1 eV from 0.14 to 1.3 L. The BE then increases to a value of 286.4 eV at 2.4 L and continually increases throughout the entire coverage range until it reaches 287.9 eV at 31.4 L.

The origin of the BE shift, or XPS chemical shift, can usually be attributed to one or more of the following: (1) initial-state effects, such as the oxidation state of an atom; (2) final-state effects, such as the extra-molecular relaxation energy due to core hole screening and (3) charging, which occurs as a result of both the material properties being analyzed and instrument-dependent factors such as the type of x-ray source and sample mounting being used [22]. In the case of DER on Ta, initial-state effects do not contribute to the BE shift with increasing coverage, but initial-state effects do explain the difference in BE between Ru in the DER molecule and metallic Ru. Metallic Ru has BE values of 284.3 and 280.1 eV for the $3d_{3/2}$ and $3d_{5/2}$ peaks, respectively, while a 0.14 L dose of DER adsorbed to Ta has BE values of 286.1 and 282.0 eV for the $3d_{3/2}$ and $3d_{5/2}$ peaks, respectively. The BE of Ru in DER is ~ 1.8 eV higher because the oxidation state of Ru is + 2, as opposed to zero valent metallic Ru. The oxidation state of Ru in molecularly adsorbed DER does not change with increasing coverage, and thus initial-state effects do not contribute to the measure BE shift.

Charging may result for insulating and partially-conducting materials when a net positive charge builds up on the sample surface due to core holes that are formed in the XPS process, which usually results in peaks that shift to higher BE and broaden appreciably. However, sample charging may result in a measurable BE shift, but have negligible impact on peak width and shape. Additionally, differential charging may occur, which is a more complicated effect that occurs when spatial variations in potential develop across the surface of a sample. Differential charging may result from inhomogeneities in the sample, resulting in regions of different electrical conductivity, or from instrument factors such as improper grounding of the sample [42]. However, the most common cause of differential charging is the use of a monochromated x-ray source, which results in a non-uniform x-ray flux across the image field. Differential charging results not only in peaks that shift to higher BE, but peaks that are also significantly broadened and distorted [43]. In the case of DER on Ta, a non-monochromatic x-ray source was used and the peaks do not broaden appreciably with increasing coverage.

Fig. 2.5b shows the FWHM of both the $3d_{3/2}$ and $3d_{5/2}$ peaks for the entire coverage range, while the inset allows a more careful examination of the FWHM at the lower coverages. The FWHM of both peaks remains constant within experimental uncertainty. It is very unlikely that any differential charging occurs, and any sample charging that occurs does not result in a significant broadening of the XPS peaks. Because of the abundance of carbon in the DER molecules, it is expected that some charging would occur in the molecular overlayer; however, it is known that the secondary electrons that are produced along with x-rays from a non-monochromatic x-ray source help neutralize sample charging [44]. Thus it is believed that some charging of the DER overlayer does occur, but the magnitude of the charging effect on the observed BE shift is uncertain.

Sample charging should not affect monolayer DER. It has been shown that molecular films of octadecylphosphonic acid (ODPA) adsorbed on native oxide-covered silicon did not charge in the monolayer regime, while multilayers exhibited charging; in fact, this effect was used to distinguish between monolayer and multilayer films of

ODPA [45]. Thus it is expected that monolayer DER does not charge, but multilayer DER exhibits some charging. Furthermore, it is well known that increasing film thickness leads to an increase in charging, as is the case for SiO_2 on Si [22]. Thus as the DER overlayer thickness increases, the sample charging will also increase.

Final-state effects in the XPS of adsorbed molecules on surfaces are quite common. The formation of a core hole in a molecular adsorbate results in an increase in the relaxation energy, referred to as the extra-molecular relaxation energy, due to screening of the core hole [46]. Both the substrate and the neighboring adsorbate molecules can contribute to core hole screening [47]. Charge transfer screening is common for both chemisorbed and physisorbed molecules on transition metal surfaces [46,48]. Core hole screening results in BE shifts with increasing coverage of adsorbate molecules. For example, in the case of SF_6 on Ni(111), the BE increases 0.2-0.3 eV going from mono- to bilayer and increases 0.8-0.9 eV going from mono- to multilayer. The observed BE in the monolayer regime is heavily influenced by image potential screening, while the BE in the multilayer regime is not significantly influenced by screening as the distance from substrate to adsorbate has increased [49]. In the case of DER on Ta, it is expected that the dominant screening mechanism is charge transfer screening. The high desorption energy of the monolayer of 2.3 eV points to chemisorption, and the dominant mechanism for chemisorbed adsorbates on transition metal surfaces is charge transfer screening.

Thus for low exposures of DER, the observed BE shift is mainly a result of charge transfer screening. The BE begins to shift at 2.4 L as a result of decreased charge transfer screening as the distance from adsorbate to substrate has increased. However, it is expected that at moderate to high DER exposures, sample charging will also impact the BE shift. The influence of sample charging will become more significant as the DER overlayer grows thicker.

The effect of the DER adsorbate on the Ta substrate was also examined. Fig .2.6 shows the substrate Ta 4f XP spectra for a bare surface and increasing DER dose amounts ranging from 0.14 to 6.1 L. Above 6.1 L, the Ta substrate attenuates significantly and the Ta 4f feature appears as a broad peak in which the doublet peaks are indistinguishable from one another, thus spectra for coverages above 6.1 L are not shown. The $4f_{5/2}$ BE does not shift at all up to 2.4 L and shows a slight decrease of 0.4 eV from 24.5 eV to 24.2 eV for a 6.1 L exposure, but the magnitude of this shift is uncertain due to the significant amount of noise in the spectrum for 6.1 L. Although core hole screening from the substrate and charging of the molecular overlayer impact the BE of the overlayer peaks, these effects do not significantly impact the BE of the substrate peaks.

The XPS data can also be utilized to investigate the exposure at which the Ta substrate is saturated with DER molecules. Fig. 2.7a shows the Ta 4f XPS peak area following adsorption of DER as a function of increasing exposure. The Ta peak area attenuates significantly and approaches a limiting value at an exposure of ~ 1.3 L. Furthermore, it is expected that as the Ta 4f substrate signal rapidly attenuates, the Ru 3d signal from the condensed DER should simultaneously increase to a limiting value. Fig. 2.7b shows the Ru 3d XPS peak area as a function of exposure. The Ru 3d peak area also reaches a limiting value at ~ 1.3 L. In order for the Ta signal to attenuate almost completely and the Ru signal to reach a limiting value, it is expected that the Ta substrate

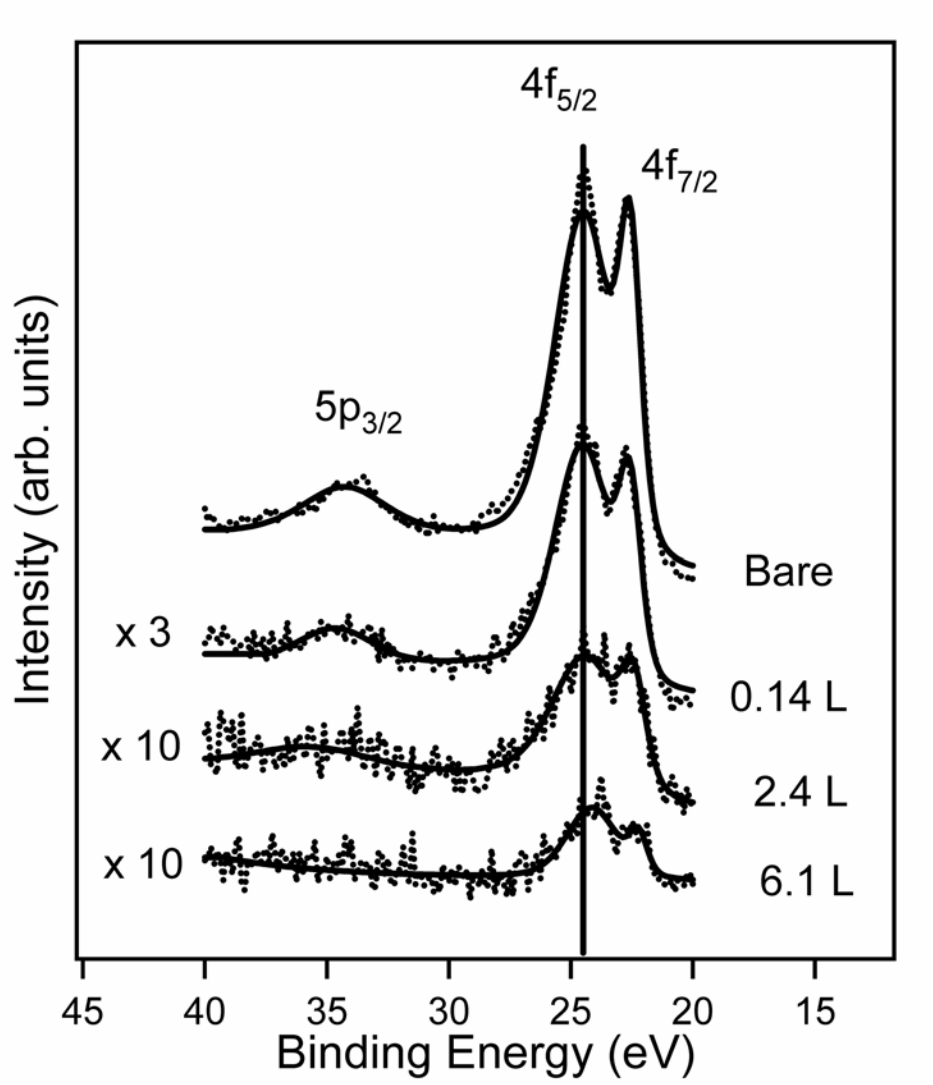

Figure 2.6. Ta 4f XP spectra for a bare surface and for DER on Ta at 140 K for exposures up to 6.1 L. The line is shown to guide the eye.

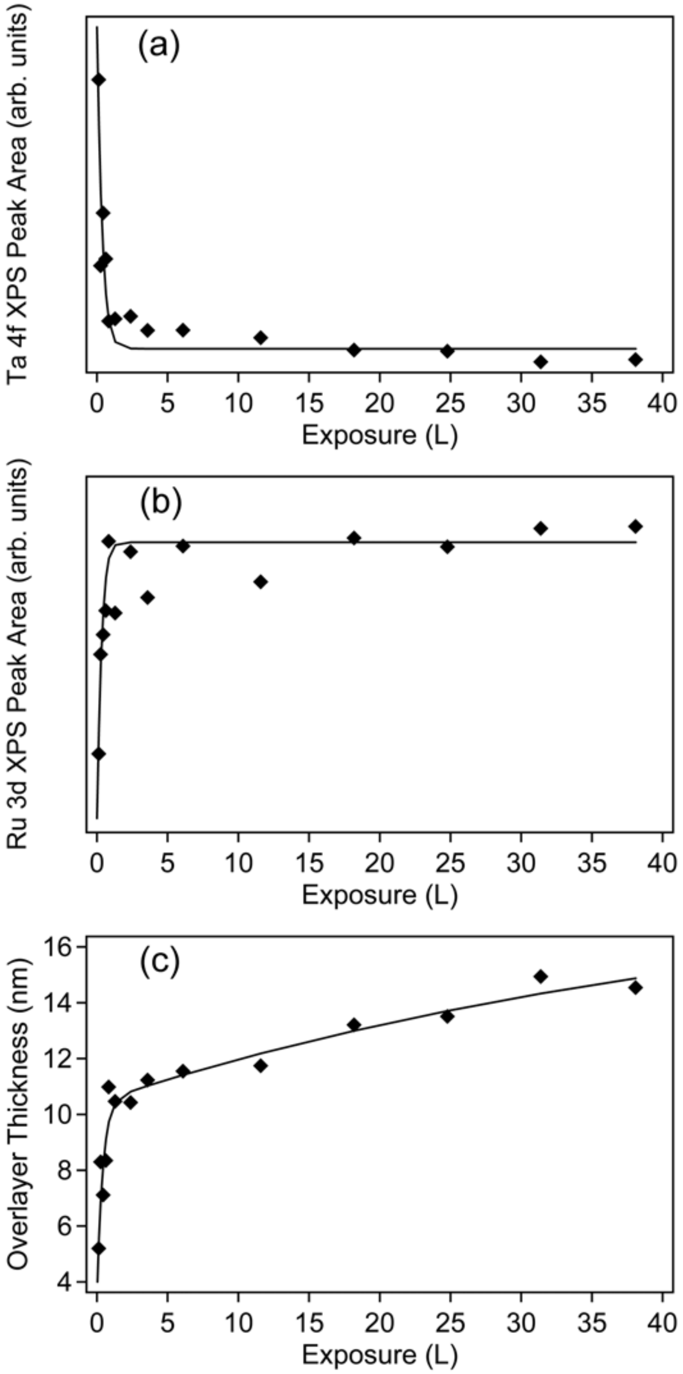

Figure 2.7. XPS data for DER on Ta at 140 K for the a) Ta 4f XPS peak area, b) Ru 3d XPS peak area, and c) DER overlayer thickness all as a function of increasing exposure. The attenuation length for Ta 4f photoelectrons passing through a DER overlayer is estimated to be 3.48 nm.

must be fully covered by DER molecules at the exposure of ~ 1.3 L. Due to the hit and stick 3D growth mode of the DER molecules, it is expected that at 1.3 L, the molecules have finally covered all available surface sites. It should be noted that a discrepancy exists between the TPD and XPS data in determining the exposure at which the Ta surface has been fully covered. The XPS data indicate Ta saturation at 1.3 L, while the TPD data show monolayer saturation at 3.6 L.

Additionally, XPS can be used to estimate the adsorbate thickness using the equation $t = -\lambda \ln(I/I_0)$ where t is the adsorbate thickness, λ is the attenuation length of the Ta 4f photoelectron through the molecular overlayer, and I and I_0 are the Ta 4f peak areas following and prior to adsorption, respectively. It should be noted that the equation is only strictly valid if the molecular overlayer is a flat, continuous film with no island structure, which is not the case for DER on Ta. In general, if the overlayer is excessively rough or has island structure, the signal from the overlayer will be attenuated while the substrate signal will be stronger as compared with the same amount of adsorbate molecules arranged in a 2D planar film. As a result of the stronger substrate signal, XPS will under-predict the film thickness. In addition, the attenuation length, λ, is not known for Ta 4f photoelectrons passing through a molecular DER overlayer. In order to obtain a reasonable estimate for λ, the NIST Electron Effective-Attenuation-Length Database has been used, which makes use of the equations developed by Tanuma, Powell, and Penn [50,51]. The NIST software gives an attenuation length of 3.48 nm for Ta 4f photoelectrons passing through a DER overlayer. Fig. 2.7c shows the overlayer thickness as a function of increasing exposure. The overlayer thickness increases abruptly for exposures up to 1.3 L and then increases in a more gradual linear fashion for exposures of 1.3 L and greater. The thickness ranges from 5.2 to 14.5 nm over the entire coverage range; however, it is somewhat meaningless to assign a film thickness to isolated DER islands that have yet not coalesced into a continuous film. The Ta 4f and Ru 3d XPS peak areas as a function of increasing exposure (Fig 2.7a and 2.7b) indicate that the Ta substrate has been fully covered by an exposure of 1.3 L. Thus it is expected that the calculated film thickness values are reasonable for exposures of 1.3 L and greater. Between 1.3 and 38.1 L, the film thickness increases from 10.5 to 14.5 nm, respectively. The fact that the film thickness only increases by 3 nm is further confirmation that a decrease in sticking coefficient occurs when arriving molecules can no longer make contact with the bare surface.

A discrepancy exists between the TPD and XPS data in determining the exposure at which the Ta surface has been fully covered. The XPS data indicate that the Ta surface is fully covered at 1.3 L, while the TPD data indicate that the monolayer is not fully saturated until 3.6 L. The island structure of the DER overlayer may lead to an attenuated XPS Ru signal from the overlayer and a stronger XPS Ta signal from the substrate as compared with the same number of DER molecules adsorbed in a 2D planar film. If this were indeed happening, it would be expected that the XPS data would incorrectly predict a *larger* exposure for saturation of the monolayer as compared with the TPD data, which is not the case here. Furthermore, if DER molecules were rearranging during the TPD heating ramp to fill in empty substrate sites, it would be expected that the TPD data would predict a *smaller* exposure for the saturation of the monolayer as compared with the XPS data, which is also not the case here. At this time, it is not understood why the XPS data predict a smaller saturation exposure than the TPD data. It can only be said that saturation of the monolayer occurs in the exposure range of 1.3-3.6 L.

2.3.1.3 XPS Following Annealing at 190 K

Annealing experiments were carried out in an attempt to check the validity of the 3D hit and stick growth mode proposed for DER on Ta. In these experiments, DER was dosed to a Ta surface held at 140 K, then annealed to 190 K for 10 min, and then cooled back down to 140 K for XPS analysis. The annealing temperature of 190 K is below the onset of desorption for DER, thus no DER should desorb and the surface coverage should remain constant. During the anneal, the chamber pressure did not increase appreciably, indicating that DER desorption did not take place. If the annealing temperature is high enough to allow surface diffusion to occur, it is expected that the DER molecules would rearrange to approach the minimum free energy structure. Thus molecules would either diffuse away from island-type structures to fill in empty surface sites or they would exhibit clustering and form 3D island structures. In the proposed 3D hit and stick growth mode, the islanding of adsorbate molecules upon adsorption occurs due to the lack of adsorbate mobility at the adsorption temperature of 140 K, as opposed to the intramolecular interactions being stronger than molecule-substrate interactions. If this is the case, it would be expected that during the anneal, DER molecules would diffuse to fill in empty substrate sites and the Ta XPS signal should attenuate.

Because it is believed that 3D hit and stick structures form at even the lowest coverages, an annealing experiment was performed for an exposure of 0.14 L. Fig. 2.8a shows the Ta substrate signal before and after the anneal for the 0.14 L exposure; the Ta

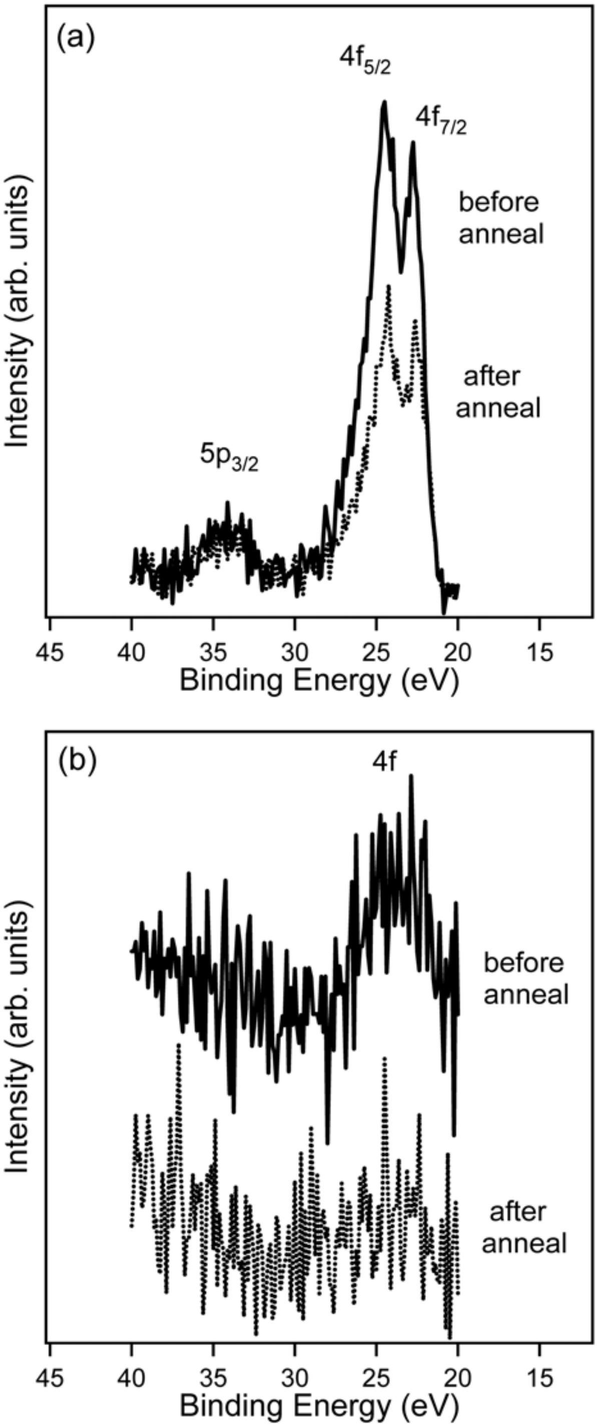

Figure 2.8. Ta 4f XP spectra for a 10 min anneal at 190 K for DER exposures of a) 0.14 L and b) 24.8 L. The anneal was completed after DER exposure to Ta at 140 K.

signal clearly attenuates, indicating that molecules have diffused to fill in empty substrate sites. Additionally, an anneal experiment was also carried out for a 24.8 L exposure. At this larger exposure, the monolayer should be fully saturated; however due to the 3D hit and stick growth mode, the overlayer film is expected to be rough and non-uniform with areas of both sparse DER coverage and areas of thicker molecular coverage. It is expected that the anneal would allow the DER molecules to rearrange to a more uniform film, in which case the Ta signal would also attenuate. Fig. 2.8b shows the Ta signal before and after the anneal for the 24.8 L exposure. The anneal causes the Ta signal to fully attenuate, supporting the proposition that 3D hit and stick structures cause a non-uniform film to form. The decrease in Ta signal with the anneal is also an indication that the overlayer thicknesses estimated from XPS are indeed under-predicted. The actual overlayer thickness for the annealed 24.8 L exposure cannot be determined because the Ta signal is fully attenuated. The anneal experiments are consistent with the proposed 3D hit and stick growth mode for DER on Ta.

2.3.2 Dissociative DER Adsorption and Desorption at 140 K

Several of the masses monitored during TPD (*m/z* 77, 91, 94, 96) have small features that differ from that of molecular DER desorption and indicate ligand dissociation from the metal center. It is important to note, however, that both ligands on the DER molecule are aromatic pentadienes and have almost identical mass spectra. For example, the EtCp ligand, which has a molecular mass of 94, has high intensity mass fragments at *m/z* 77 and 91. The DMPD ligand, which has a molecular mass of 96, has high intensity mass fragments at *m/z* 77, 91, and 94. There are no unique *m/z* values that can be used to differentiate between the two ligands in TPD, although any signal at *m/z*

96 must be due to the DMPD ligand. However, the signal at *m/z* 94 may be a result of either desorption of the intact EtCp ligand *or* cracking of the DMPD ligand in the mass spectrometer. If the ratio of the *m/z* 94 and 96 TPD peak areas is consistent with the ratio of *m/z* 94 and 96 in the mass spectrum of DMPD, then any contribution from EtCp can be ruled out. These ratios are not consistent, and thus desorption signals for masses 77, 91, and 94 most likely include contributions from both the EtCp and DMPD ligands. Thus signals for *m/z* 77, 91, 94, and 96 are a result of desorption of the intact ligands, for which *m/z* 77 and 91 correspond to the cracking of the ligands in the mass spectrometer, *m/z* 94 corresponds to both desorption of the intact EtCp ligand and cracking of the DMPD ligand in the mass spectrometer, and *m/z* 96 corresponds to the desorption of intact DMPD. Although *m/z* 77 and 91 were monitored to verify ligand desorption, these signals have spectra with the same features as the intact ligands (*m/z* 94 and 96) and are not shown.

Fig. 2.9 shows TPD spectra for *m/z* 94 and 96 for a 24.8 L exposure. In addition to the multilayer and monolayer peaks, there are two additional features at 168 K and 215 K that appear for both *m/z* 94 and 96, but are not present for molecular DER desorption (see Fig 2.1). Because the desorption signal for *m/z* 94 most likely contains contributions from both the EtCp and DMPD ligands, it appears likely that both ligands are contributing to the desorption features at 168 and 215 K. Ligand desorption indicates that a surface reaction is taking place, although it is unclear whether the reaction occurs upon DER adsorption or during the TPD temperature ramp.

XPS analysis reveals that hydrocarbon and Ru-hydrocarbon fragments remain on the Ta surface after TPD has been completed. Fig. 2.10 shows Ru XP spectra for a 24.8

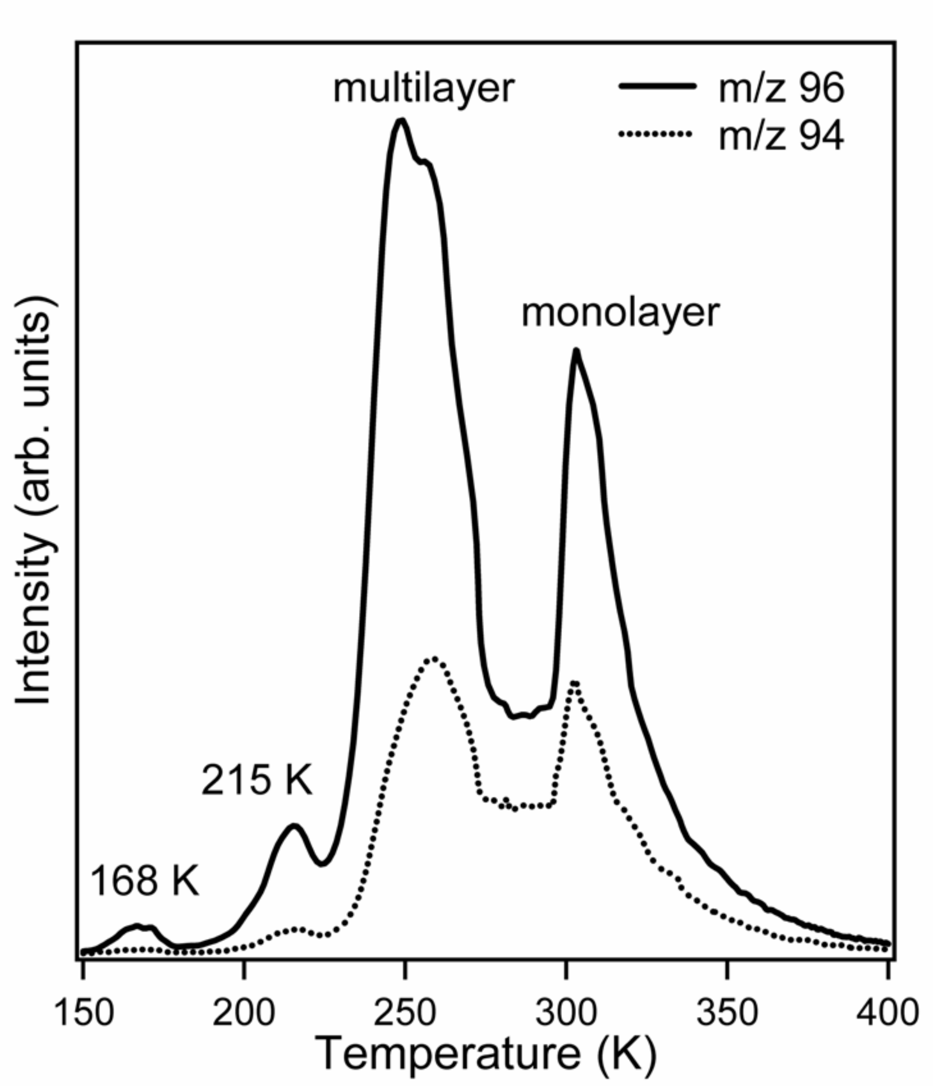

Figure 2.9. TPD spectra for EtCp + DMPD (m/z 94) and DMPD (m/z 96) for a 24.8 L DER exposure to Ta at 140 K. The heating rate was 7 K/s.

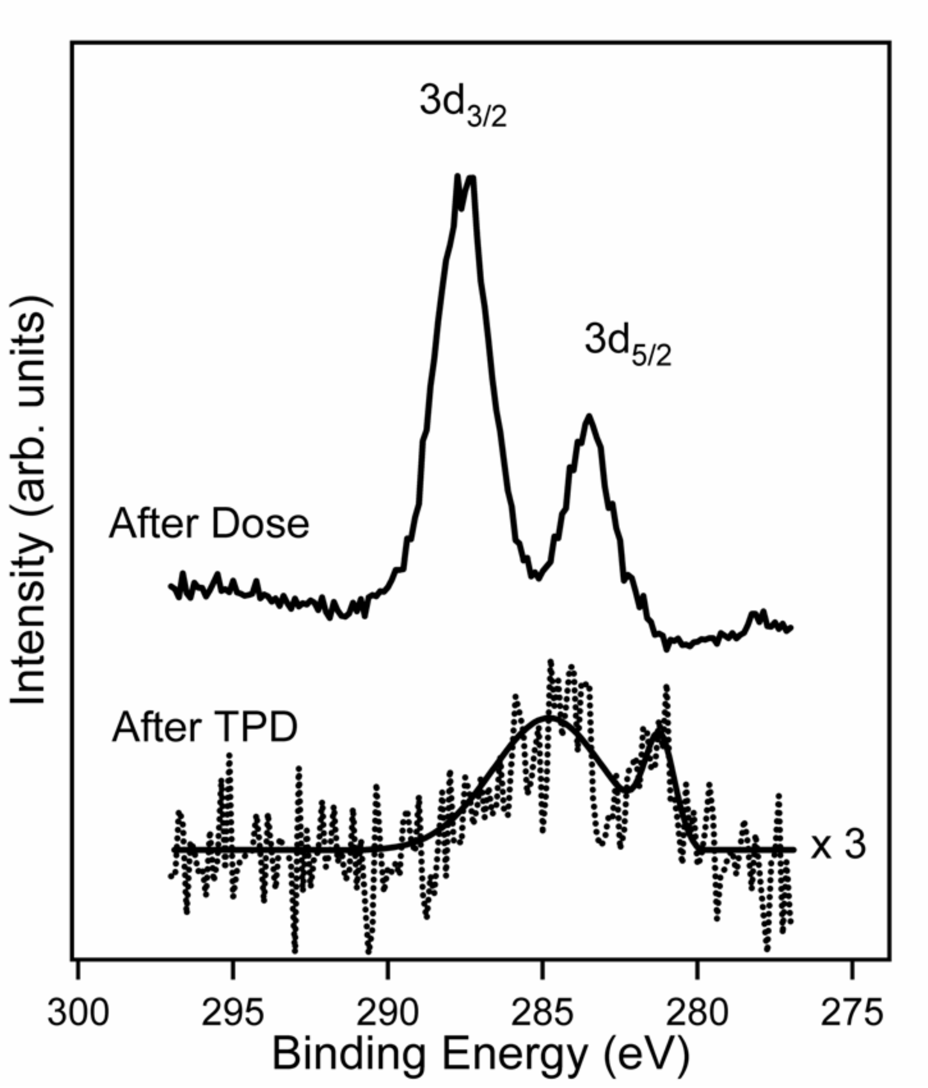

Figure 2.10. Ru 3d XP spectra for a 24.8 L DER exposure for both molecular adsorption at 140 K and the surface species remaining after TPD at 7 K/s from 145-973 K.

L exposure both after the DER dose and following TPD. The spectrum for DER following the dose is identical to the one shown in Fig. 2.4 and is reproduced here for comparison purposes. For molecular DER adsorption, the Ru $3d_{3/2}$ and $3d_{5/2}$ peaks are at 287.5 and 283.4 eV, respectively. After TPD, the Ru $3d_{3/2}$ and $3d_{5/2}$ peaks decrease to 284.9 and 281.3 eV, respectively. The Ru $3d_{3/2}$ and C1s peaks overlap, so the feature at 284.9 eV is a result of both Ru and C fragments on the surface. The decreasing shift in BE is a result of dissociation of the DER molecules; however, the DER ligands have not completely dissociated from the Ru core to leave metallic Ru on the surface. The $3d_{3/2}$ and $3d_{5/2}$ BE for metallic Ru are 284.3 and 280.1 eV, respectively. Thus after TPD, the Ru 3d BE values are in-between that of molecular DER and metallic Ru, indicating that the adsorbed Ru remaining on the surface is still bonded to some type of hydrocarbon fragment, possibly an intact or partially dissociated ligand.

In addition, the surface reaction is suppressed when the Ta substrate is not properly cleaned. After each experiment, the Ta surface is cleaned by Ar^+ ion sputtering followed by a 10 min anneal at 1073 K to heal the ion damage. If the Ta surface is not cleaned and the hydrocarbon/Ru residue remains on the surface, the TPD desorption peaks at 168 K and 215 K are not present. Thus the hydrocarbon/Ru residue is blocking the active sites on the surface at which reaction occurs. The desorption features at 168 K and 215 K are a result of monolayer DER dissociating on the Ta surface into hydrocarbon and Ru-hydrocarbon fragments that remain adsorbed to the surface and intact EtCp and DMPD ligands that desorb.

The quantity of monolayer DER that dissociates as compared with the quantity that desorbs molecularly cannot be determined; however, the monolayer desorption peaks for molecular DER (Fig.2.1) are significantly larger than those corresponding to ligand desorption (Fig. 2.9). Furthermore, XP spectra in the monolayer regime are expected to be significantly broader if dissociation occurs, due to the presence of both molecularly adsorbed molecules and their decomposition products. For example, monolayer thiophene on W(110) had a C 1s FWHM of 3.2 eV as compared with multilayer thiophene with a FWHM of 2.2 eV. The broadening of the monolayer peak was a result of both thiophene and its decomposition being present on the surface [52]. As mentioned previously, the FWHM of the Ru 3d spectra remains constant within experimental uncertaintly over the entire coverage range examined. The small TPD ligand desorption peaks and the constant XPS FWHM of the Ru 3d peaks going from monolayer to multilayer coverage both indicate that the amount of monolayer DER that dissociates is not significant as compared with the amount that desorbs molecularly. It is likely that the DER dissociation is occurring at defect sites, such as step-edges or kinks, on the polycrystalline Ta. It is uncertain why ligand desorption results in two separate peaks in the TPD spectra; however, it is possible that the two features at 168 K and 215 K may result from desorption from different types of defect sites.

The fact that DER only undergoes a minor surface reaction at defect sites is not unexpected. The DER precursor requires oxygen as a co-reactant in order for Ru films to be deposited [14]. The oxygen combusts the EtCp and DMPD ligands, which are not labile enough to be dissociated thermally. It is suspected that the higher reactivity of the DMPD ligand as compared with the EtCp ligand leads to improved nucleation of Ru films from DER versus $Ru(EtCp)_2$. It is believed that the DMPD ligand facilitates the initial adsorption of DER on the substrate and the DMPD dissociates from the precursor more easily than EtCp [14]. Unfortunately, we are unable to address the validity of this suggestion due to the inability to differentiate between the DMPD and EtCp ligands in TPD, as the signals at *m/z* 94 and 96 most likely contain contributions from the desorption of both ligands.

2.3.3 DER Adsorbed at Room Temperature and Above

While the majority of the DER adsorbs molecularly to Ta held at 140 K, DER does not adsorb molecularly when the Ta is held at room temperature and above. At room temperature and above, only first layer adsorption occurs (no second layer DER adsorbs), thus sample charging does not impact the observed BE values. Fig. 2.11a shows Ru 3d XP spectra for 0.85 L exposures of DER adsorbed to Ta for temperatures from 303 K to 773 K. The BE of the Ru $3d_{3/2}$ + C 1s peak decreases with increasing temperature, as shown in Fig. 2.12a, while the Ru $3d_{5/2}$ peak is not distinguishable until 673 K. The decreasing shift in BE is a result of increasing dissociation of the DER molecules with increasing temperature. As the DER molecules dissociate, the Ru 3d BE decreases to approach that of metallic Ru. For temperatures of 303-573 K, the absence of the Ru $3d_{5/2}$ peak suggests that DER has deposited only hydrocarbon fragments on the surface. At the highest temperature of 773 K, the $3d_{3/2}$ and $3d_{5/2}$ BE values are 284.3 and 280.5 eV, respectively. For metallic Ru, the $3d_{3/2}$ and $3d_{5/2}$ BE values are 284.3 and 280.1 eV, respectively. Thus at 773 K, the BE values are very close to those of metallic Ru, indicating that the DER has dissociated considerably. The surface species include Ru and Ru-hydrocarbon fragments, similar to the surface species remaining after TPD, as discussed in Section 2.3.2.

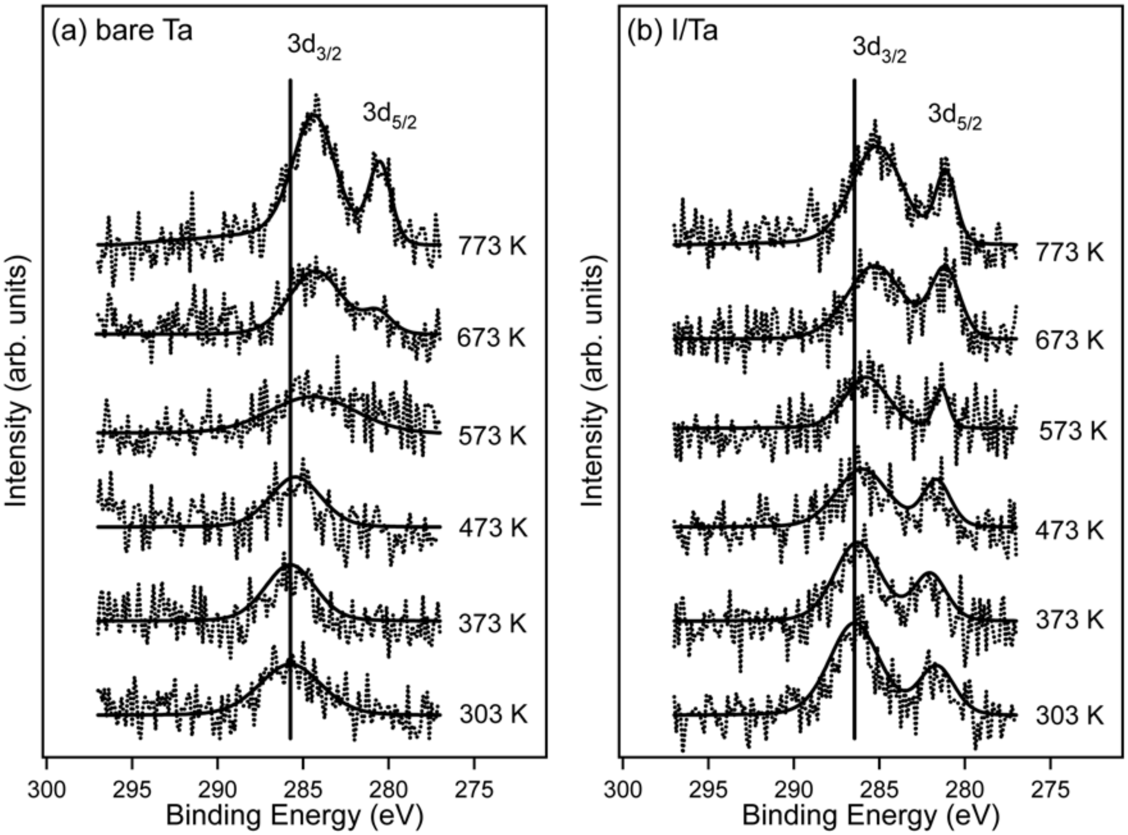

Figure 2.11. Ru 3d XP spectra for 0.85 L DER exposures from 303-773 K for a) bare Ta and b) I/Ta. The lines are shown to guide the eye.

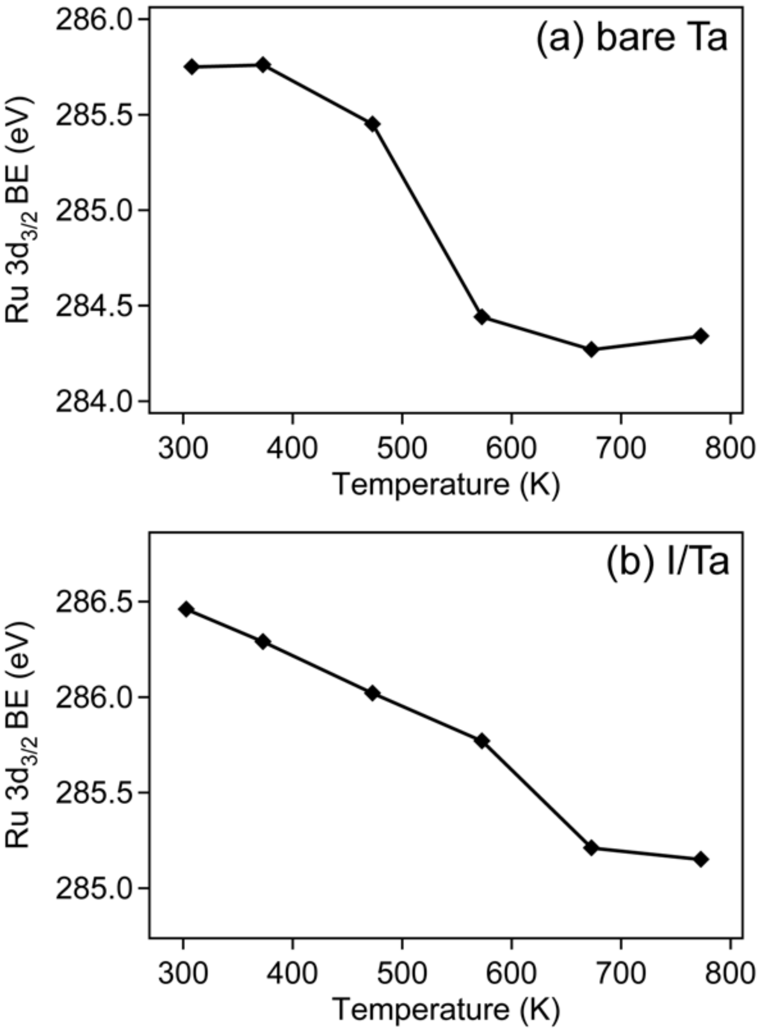

Figure 2.12. Ru $3d_{3/2}$ BE for 0.85 L DER exposures from 303-773 K for a) bare Ta and b) I/Ta.

2.3.4 DER Adsorption With CH_3I

2.3.4.1 CH_3I Adsorption on Ta

The surface chemistry of CH_3I has been extensively studied on many transition metal surfaces, including Cu(111) [19], Ru(001) [20], Pd(111) [53], Pt(111) [54], Ag(111) [55], Ni(100) [56], and polycrystalline W [57]. On all of these surfaces except for W, CH_3I dissociates into adsorbed CH_3 and I. Depending on the particular transition metal surface, the adsorbed methyl group may evolve as methane, or the methyl group may undergo additional surface reaction and desorb as another hydrocarbon species such as ethane. In most cases, adsorbed iodine is stable up to temperatures between 800-1000 K. Although the hydrocarbon desorption temperatures vary depending on the particular gas being evolved and the transition metal surface, in general, hydrocarbon desorption is complete by 400 K, leaving only adsorbed iodine on the metal surface, along with residual surface carbon in some cases. It is worth noting that on W, CH_3I dissociates into adsorbed surface carbon, iodine, and H_2. No methane or other hydrocarbon species desorb.

Although an in-depth study of CH_3I adsorption and dissociation on polycrystalline Ta has not been completed, CH_3I behaves similarly on Ta as it does on the other transition metals. Upon dosing CH_3I to Ta held at 140 K, the XPS C 1s signal is located at 286.3 eV and the I $3d_{5/2}$ signal is located at 621.7 eV (not shown). Upon heating the Ta to 500 K, the C 1s signal is not distinguishable above the noise level and the I $3d_{5/2}$ signal decreases to 619.5 eV. It is known that not all first layer CH_3I dissociates on transition metal surfaces. For example, molecularly adsorbed monolayer CH_3I desorbs from Ni(100) at 169K [56], from Ag(111) at 192 K [55], and from Pt(111) at 239 K [54].

Thus at 140 K, both molecular and dissociated CH_3I are most likely on the Ta surface. Furthermore, some multilayer CH_3I may also be present at 140 K. Thus the C 1s and I $3d_{5/2}$ BE values at 140 K represent both molecularly adsorbed CH_3I and any dissociated CH_3I as well. Upon heating to 500 K, the XPS carbon signal disappears, indicating that any multilayer or molecularly adsorbed monolayer CH_3I has desorbed. Furthermore, the remaining monolayer CH_3I has fully dissociated (most likely into CH_3 and I) and the resulting hydrocarbon species (i.e., methane, ethane) have desorbed. Although it may be expected that CH_3I on polycrystalline Ta may behave similarly to that on polycrystalline W, the absence of surface carbon after heating indicates otherwise. In addition, after heating to 500 K, the I $3d_{5/2}$ signal at 619.5 eV corresponds to that of atomically adsorbed iodine. Thus dosing CH_3I to a Ta surface held at 140 K and then heating to 500 K results in a carbon-free Ta surface with atomically adsorbed iodine.

2.3.4.2 DER Adsorption on I/Ta

Fig. 2.13a shows Ru 3d XP spectra for a 0.45 L DER exposure to a Ta surface held at 298 K. The DER exposure leads to a small, broad peak resulting from hydrocarbon residue from DER decomposition, but no Ru or Ru-containing species are present. To determine if adsorbed iodine influences the adsorption and/or dissociation behavior of DER, CH_3I was dosed to the Ta surface prior to the DER dose. For this experiment, CH_3I was dosed to the Ta held at 140 K, then heated to 500 K to leave atomically adsorbed iodine, and then cooled back down to 298 K for the DER dose. Fig. 2.13b shows the Ru 3d XP spectra for a 0.45 L DER exposure to an iodine-modified Ta surface at 298 K. In contrast with dosing DER to a bare Ta surface, the DER adsorbs molecularly to the iodine-modified Ta surface. Fig. 2.13c shows a 0.45 L exposure of

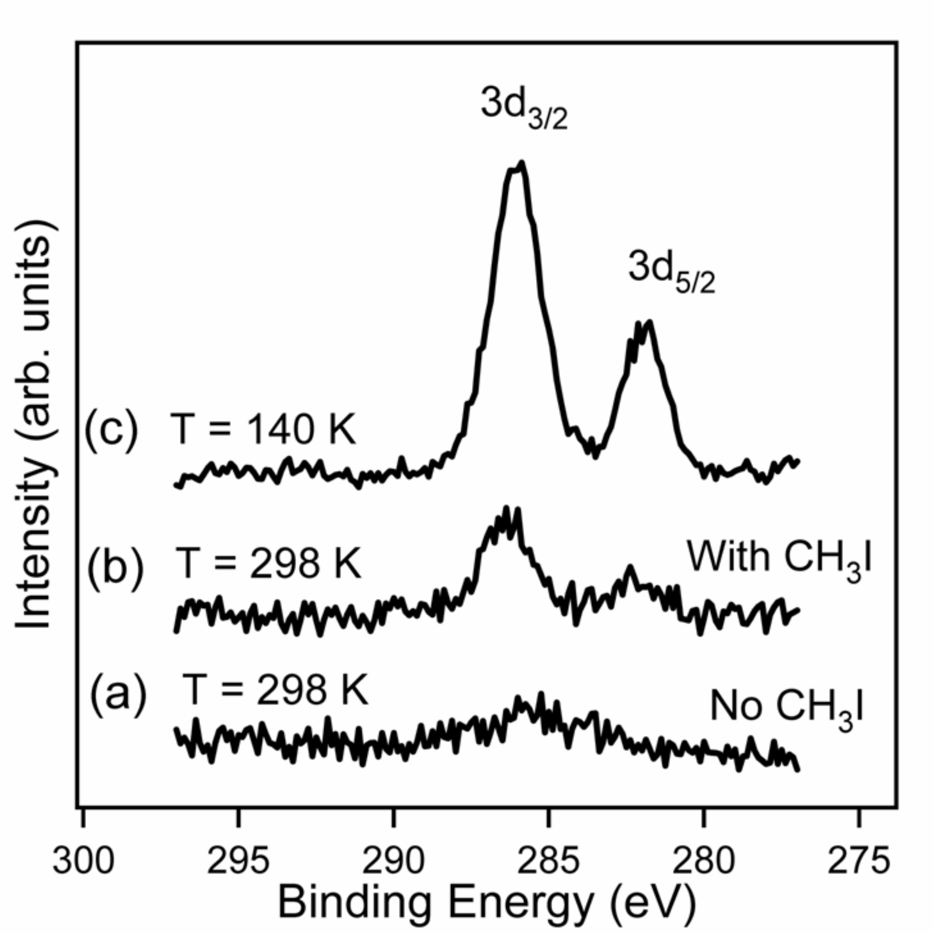

Figure 2.13. Ru 3d XP spectra for 0.45 L DER exposures for a) bare Ta at 298 K, b) I/Ta at 298 K and c) bare Ta at 140 K.

molecularly adsorbed DER at 140 K for comparison purposes. The BE for DER adsorbed on I/Ta at 298 K is shifted up by about 0.4 eV as compared with molecularly adsorbed DER at 140 K. This BE increase is most likely a result of the adsorbed iodine influencing core hole screening and/or altering the local surface potential. Small BE shifts have been observed for other adsorbates dosed to bare versus modified surfaces. In the case of SF_6 dosed to Ni(111) and O/Ni(111), the S 2p BE shifted up by 0.3 eV for the O/Ni(111) surface [49]. The shift was attributed to changes in the local potential of the substrate due to the adsorbed atomic oxygen [49]. Notably, the adsorbed iodine has not caused the BE to decrease, which indicates that the iodine has not caused the DER molecules to dissociate. Thus adsorbed iodine has promoted the adsorption of molecular DER at room temperature.

The effect of adsorbed iodine was investigated for temperatures from 303-773 K. In these experiments, CH_3I was backfilled into the chamber to a pressure of 2×10^{-6} torr and then DER was dosed to the Ta. Backfill doses of CH_3I to a heated Ta substrate result in a carbon-free surface with atomically adsorbed iodine, similar to dosing at 140 K and then heating to 500 K. Fig. 2.11b shows Ru 3d XP spectra for 0.85 L exposures of DER adsorbed to I/Ta for temperatures from 303 K to 773 K. The BE of the Ru $3d_{3/2}$ + C 1s peak decreases with increasing temperature, as shown in Fig. 2.12b (the Ru $3d_{5/2}$ BE follows a similar trend). The decreasing shift in BE is a result of some dissociation of the DER molecules with increasing temperature; however, the DER is less dissociated on the I/Ta surface than on the bare Ta surface. At the lowest temperature of 303 K, the $3d_{3/2}$ BE of 286.5 eV is shifted up by 0.4 eV as compared with a 0.85 L exposure of molecularly adsorbed DER at 140 K, due to differences in core hole screening and surface potential due to the adsorbed iodine. Thus at 303 K DER is molecularly adsorbed; however, the decreasing BE with increasing temperature indicates that the DER is dissociating somewhat with increasing temperature. At the highest temperature of 773 K, the $3d_{3/2}$ BE values on I/Ta and bare Ta are 285.2 and 284.3 eV, respectively. The BE on I/Ta is 0.9 eV higher than that on bare Ta. If ~ 0.4 eV of this observed shift is due to the influence of iodine on core hole screening and surface potential, then the BE on I/Ta is shifted up ~ 0.5 eV as compared with bare Ta. The higher BE on the I/Ta as compared with bare Ta indicates that the DER molecules are not as dissociated on the I/Ta surface. Furthermore, on I/Ta the $3d_{5/2}$ peak is evident over the entire temperature range, while on bare Ta the $3d_{5/2}$ peak is not distinguishable until 673 K. Thus DER undergoes some dissociation on the I/Ta surface, as indicated by the decreasing BE with increasing temperature; however, the amount of dissociation is minor as compared with the bare surface. Ultimately, adsorbed iodine both promotes DER adsorption and reduces DER dissociation at room temperature and above.

Most likely, the iodine decreases DER decomposition by blocking active sites on the Ta substrate. In addition, the iodine increases DER adsorption. In the case of SF_6 dosed to Ni(111) and O/Ni(111), it was found that the pre-adsorbed atomic oxygen both facilitated a stronger adsorption bond of the SF_6 to the surface and increased the sticking coefficient. In the monolayer regime, the sticking coefficient was 0.6 for the bare and 0.85 for the oxygen-precovered Ni(111) surface. The authors suggested that the pre-adsorbed oxygen both enhanced the lateral corrugation of the surface by creating a deeper vertical potential, thus allowing more impinging molecules to adsorb, and the oxygen facilitated a stronger SF_6 adsorption bond due to the dipole of the oxygen interacting with the SF_6 by polarization [49]. The adsorbed iodine may affect DER in a similar manner; adsorption of DER is increased due to the deeper vertical potential of the surface when iodine is pre-adsorbed.

2.4. CONCLUSION

When the Ta is held at 140 K, the majority of DER dosed to the surface adsorbs and desorbs molecularly. TPD indicates that multilayer DER desorbs between 272 and 263 K. Multilayer desorption kinetics appear to be fractional order with repulsive interactions, with a zero coverage desorption energy of 0.9 eV. Monolayer DER desorbs between 278 and 297 K, exhibiting kinetics that appear to be first order with attractive lateral interactions. The monolayer zero coverage desorption energy is 2.3 eV. XPS Ru 3d BE values increase with increasing exposure. The observed shift is attributed to the influence of core hole screening in the monolayer regime and increased sample charging as the DER overlayer becomes thicker in the multilayer regime. Saturation of the monolayer occurs in the exposure range of 1.3-3.6 L, although second layer DER is evident for exposures as low as 0.64 L and may even be present for lower exposures. The sticking coefficient of DER drops significantly once all the Ta surface sites have been occupied, as evidenced by both the abrupt change in slope of the TPD uptake curve and the minimal change in XPS overlayer thickness from 10.5 to 14.5 nm for exposures of 1.3 to 38.1 L. DER exhibits a 3D island growth mode due to the random formation of 3D hit and stick structures, which develop due to the lack of adsorbate mobility at 140 K. Annealing experiments are consistent with the proposed growth mode. Although the majority of DER adsorbs molecularly, a minor surface reaction occurs at defect sites.

The surface reaction results in ligand desorption (both EtCp and DMPD) and hydrocarbon and Ru-hydrocarbon species that remain on the Ta surface.

When the Ta is held between 298-773 K, DER decomposes leaving mostly hydrocarbon species on the surface. No Ru is evident in the XP spectra until 673 K. When the Ta is pre-covered with atomic iodine, DER dissociation is significantly decreased while adsorption is increased. The iodine blocks dissociation sites and increases the vertical potential of the Ta surface, allowing more of the impinging molecules to adsorb.

2.5 REFERENCES

[1] I. Goswami, R. Laxman, Semicond. Int. 27 (2004) 49.

[2] M. L. Green, M. E. Gross, L. E. Papa, K. J. Schnoes, D. Brasen, J. Electrochem. Soc. 132 (1985) 2677.

[3] Q. Wang, J. G. Ekerdt, D. Gay, Y.-M. Sun, J. M. White, Appl. Phys. Lett. 84 (2004) 1380.

[4] M. Kadoshima, T. Nabatame, M. Hiratani, Y. Nakamura, I. Asano, T. Suzuki, Jpn. J. Appl. Phys. 41 (2002) L347.

[5] Y.-H. Song, Y.-L. Chen, Y. Chi, C.-S. Liu, W.-L. Ching, J.-J. Kai, R.-S. Chen, Y.-S. Huang, A. J. Carty, Chem. Vap. Deposition 9 (2003) 162.

[6] T. Aaltonen, P. Alén, M. Ritala, M. Leskelä, Chem. Vap. Deposition 9 (2003) 45.

[7] K. J. Park, J. M. Doub, T. Gougousi, G. N. Parsons, Appl. Phys. Lett. 86 (2005) 051903.

[8] Y. Matsui, M. Hiratani, T. Nabatame, Y. Shimamoto, S. Kimura, Electrochem. Solid-State Lett. 5 (2002) C18.

[9] S. Y. Kang, K. H. Choi, S. K. Lee, C. S. Hwang, H. J. Kim, J. Electrochem. Soc. 147 (2000) 1161.

[10] K. Kawano, H. Kosuge, N. Oshima, H. Funakubo, Electrochem. Solid-State Lett. 10 (2007) D60.

[11] Y. Matsui, M. Hiratani, T. Nabatame, Y. Shimamoto, S. Kimura, Electrochem. Solid-State Lett. 4 (2001) C9.

[12] K. Kawano, A. Nagai, H. Kosuge, T. Shibutami, N. Oshima, H. Funakubo, Electrochem. Solid-State Lett. 9 (2006) C107.

[13] T. Shibutami, K. Kawano, N. Oshima, S. Yokoyama, H. Funakubo, Electrochem. Solid-State Lett. 6 (2003) C117.

[14] S. K. Kim, S. Y. Lee, S. W. Lee, G. W. Hwang, C. S. Hwang, J. W. Lee, J. Jeong, J. Electrochem. Soc. 154 (2007) D95.

[15] J. J. Kim, D. H. Jung, M. S. Kim, S. H. Kim, D. Y. Yoon, Thin Solid Films 409 (2002) 28.

[16] J. J. Kim, M. S. Kim, D. Y. Yoon, Chem. Vap. Deposition 9 (2003) 105.

[17] E. S. Hwang, J. Lee, Chem. Mater. 12 (2000) 2076.

[18] E. S. Hwang, J. Lee, Electrochem. Solid-State Lett. 3 (2000) 138.

[19] J.-L. Lin, B. E. Bent, J. Vac. Sci. Technol. A 10 (1992) 2202.

[20] Y. Zhou, M. A. Henderson, W. M. Feng, J. M. White, Surf. Sci. 224 (1989) 386.

[21] A. Kis, J. Kiss, F. Solymosi, Surf. Sci. 459 (2000) 149.

[22] B. Ulgut, S. Suzer, J. Phys. Chem. B 107 (2003) 2939.

[23] A. M. Lemonds, J. M. White, J. G. Ekerdt, Surf. Sci. 527 (2003) 124.

[24] M. A. Chesters, B. J. Hopkins, M. R. Leggett, Surf. Sci. 43 (1974) 1.

[25] T. Shibutami, K. Kawano, N. Oshima, S. Yokoyama, H. Funakubo, Mat. Res. Soc. Symp. Proc. 748 (2003) 111.

[26] A. M. Lemonds, J. M. White, J. G. Ekerdt, Surf. Sci. 538 (2003) 191.

[27] K. Andersson, A. Gómez, C. Glover, D. Nordlund, H. Öström, T. Schiros, O. Takahashi, H. Ogasawara, L. G. M. Pettersson, A. Nilsson, Surf. Sci. 585 (2005) L183.

[28] W. X. Huang, J. M. White, J. Phys. Chem. B 108 (2004) 5060.

[29] W. Zhao, W. Wei, J. M. White, Surf. Sci. 547 (2003) 374.

[30] W. Frie*β*, H. Schlichting, D. Menzel, Phys. Rev. Lett. 74 (1995) 1147.

[31] D. Welipitiya, C. N. Borca, C. Waldfried, C. Hutchings, L. Sage, C. M. Woodbridge, P. A. Dowben, Surf. Sci. 393 (1997) 34.

[32] T. Rockey, H.-L. Dai, Surf. Sci. 601 (2007) 2307.

[33] A. S. Bolina, A. J. Wolff, W. A. Brown, J. Chem. Phys. 122 (2005) 044713.

[34] M. Parschau, K. Christmann, Surf. Sci. 347 (1996) 63.

[35] S. Varma, P. A. Dowben, J. Vac. Sci. Technol. A 8 (1990) 2605.

[36] J. B. Miller, H. R. Siddiqui, S. M. Gates, J. N. Russell, Jr., J. T. Yates, Jr., J. C. Tully, M. J. Cardillo, J. Chem. Phys. 87 (1987) 6725.

[37] J. W. Niemantsverdriet, K. Wandelt, J. Vac. Sci. Technol. A 6 (1988) 757.

[38] B. Luo, Q. Wang, J. M. White, Chem. Vap. Deposition, 10 (2004) 311.

[39] C.-M. Chan, R. Aris, W. H. Weinburg, Appl. Surf. Sci. 1 (1978) 360.

[40] N. Karl, Ch. Günther, Cryst. Res. Technol. 34 (1999) 243.

[41] K. R. Paserba, A. J. Gellman, Phys. Rev. Lett. 86 (2001) 4338.

[42] N. J. Havercroft, P. M. A. Sherwood, Surf. Interface Anal. 29 (2000) 232.

[43] B. J. Tielsch, J. E. Fulghum, Surf. Interface Anal. 24 (1996) 28.

[44] B. J. Tielsch, J. E. Fulghum, Surf. Interface Anal. 24 (1996) 459.

[45] I. Gouzman, M. Dubey, M. D. Carolus, J. Scwartz, S. L. Bernasek, Surf. Sci. 600 (2006) 773.

[46] O. Gunnarsson, K. Schönhammer, Phys. Scripta 21 (1980) 575.

[47] J. Schnadt, J. N. O'Shea, L. Patthey, J. Schiessling, J. Krempaský, M. Shi, N. Mårtensson, P. A. Brühwiler, Surf. Sci. 544 (2003) 74.

[48] K. Wandelt, B. Gumhalter, Surf. Sci. 140 (1984) 355.

[49] A. Klekamp, E. Umbach, Surf. Sci. 249 (1991) 75.

[50] S. Tanuma, C. J. Powell, D. R. Penn, Surf. Interface Anal. 17 (1991) 927.

[51] S. Tanuma, C. J. Powell, D. R. Penn, Surf. Interface Anal. 21 (1994) 165.

[52] J. E. Whitten, Surf. Sci. 546 (2003) 107.

[53] D. Stacchiola, Y. Wang, W. T. Tysoe, Surf. Sci. 524 (2003) 173.

[54] M. A. Henderson, G. E. Mitchell, J. M. White, Surf. Sci. 184 (1987) L325.

[55] X.-L. Zhou, F. Solymosi, P. M. Blass, K. C. Cannon, J. M. White, Surf. Sci. 219 (1989) 294.

[56] X.-L. Zhou, J. M. White, Surf. Sci. 194 (1988) 438.

[57] X.-L. Zhou, C. Yoon, J. M. White, Surf. Sci. 206 (1988) 379.

Chapter 3: The Effect of an Iodine Source on Nucleation and Film Properties of Ru Films Deposited by Chemical Vapor Deposition

3.1 INTRODUCTION

As device dimensions in integrated circuits scale down, there is an increasing need to deposit ultra-thin, conformal, continuous films for use in applications such as barrier and copper seed layers in back end processing. Currently, the diffusion barrier and seed layer of choice are a Ta/TaN bi-layer followed by a copper seed layer, both deposited by physical vapor deposition (PVD). However, the PVD technology may not be extendable as device features scale below the 32-nm generation due to difficulties in depositing conformal films [1,2]. One possible solution for an alternative diffusion barrier and copper seed layer technology is to develop a liner material that acts to both prevent diffusion and enable copper deposition. Several of the transition metals, including Ru and alloys of Ru with phosphorus, deposited by chemical vapor deposition (CVD), are attractive candidates for the liner material [3,4].

Chemical vapor deposition (CVD) allows conformal deposition in high aspect ratio features, and Ru has several properties that make it a desirable material in microelectronic applications, such as low electrical resistivity, high thermal stability, high chemical stability in the presence of oxygen and water, and negligible solubility with copper [1]. However, there are some limitations that must be overcome in the deposition of Ru films. CVD Ru films suffer from poor nucleation on oxide and nitride substrates such as SiO_2 [5-7], Si_3N_4 [8,9], and TiN [10,11]. Ru follows a Volmer-Weber growth mode in which 3D islands form on the substrate surface. In the case of poor nucleation, sparse islands are formed that lead to rough, large-grained, polycrystalline columnar films with sizeable grain boundaries that may extend through the entire film. For application as a liner material, films should be smooth and nanocrystalline (or amorphous) with minimal grain boundaries. Cu diffusion occurs more rapidily through grain boundaries than through the bulk material, and thus minimizing grain boundaries is essential in producing an effective barrier material [3].

The issue of nucleation will become more significant with decreasing device dimensions. The liner thickness for the 32-nm technology node must be < 3 nm, and the required thickness will continue to decrease with future technology nodes. Thus the liner must be the thinnest possible continuous film that both prevents diffusion and allows uniform copper deposition. A high initial nucleation density is essential to achieve continuity of ultra-thin films; poor nucleation leads to sparse islands on the substrate surface, which do not coalesce into a continuous film until the thickness greatly exceeds the requirements for the liner material. Furthermore, poor nucleation leads to films with increased surface roughness, which impedes the filling of high aspect ratio features and leads to increased resistivity [12].

One attempt to influence nucleation density and film properties of CVD films has involved the use of an iodine source during growth. Hwang and Lee report the use of adsorbed iodine in Cu CVD on TiN [13,14]. The particular iodine source being used is not of consequence; C_2H_5I, CH_3I, $(CH3)_3CI$, and I_2 all show similar effects. The issue of importance is that the iodine-containing molecule should leave only adsorbed iodine on the Cu at the film growth temperature. For example, CH_3I dissociates on Cu into adsorbed methyl groups and iodine atoms. Above 400 K, the methyl groups decompose to evolve methane, ethylene, propylene, and ethane, while the adsorbed iodine is stable up to 950 K [15]. Hwang and Lee suggest that adsorbed iodine in Cu CVD behaves in a manner similar to surfactants in epitaxial growth of metals on metals. In epitaxial growth, surfactant species change the growth mode from 3D Volmer-Weber to 2D layer-by-layer growth, and surfactants are known to segregate to the surface of the deposited films [16]. In the case of Cu CVD, it was observed that iodine acted as a catalyst to enhance the growth rate and segregated to the film surface during growth. Iodine-catalyzed island growth led to islands with a larger average size and a wider size distribution at the onset of coalescence. Improved film roughness was also observed. Other research groups [17,18] have also observed the catalytic effect and surface segregation of iodine during Cu CVD.

The role of iodine in CVD Ru on TiN has also been explored [19,20]. CH_3I has similar surface chemistry on Ru as it does on Cu. CH_3I dissociates into adsorbed methyl groups and iodine atoms on Ru(001); although the only gas that desorbs is methane, the majority of which evolves at 170 K [21]. Adsorbed iodine is stable on the Ru surface up to 1080 K [22]. Thus above 170 K, CH_3I dosed to Ru results primarily in adsorbed atomic iodine, although some residual carbon contamination remains on the surface. In Ru CVD with adsorbed iodine, improved film roughness was observed, as in the case with Cu CVD, although several other properties differed in the case of Ru as compared with Cu. No iodine XPS signal was observed at the film surface after growth, which suggests that iodine may not be segregating to the film surface. In addition, the deposition rate was depressed when an iodine source was used, and smaller, denser nuclei were observed at the initial stages of growth.

One of the major experimental differences between the case of Cu and Ru CVD is the precursors being used for growth. Cu CVD was carried out with copper(I) hexafluoroacetylacetonate vinyltrimethylsilane [Cu^I(hfac)(vtms)], which thermally decomposes and requires no co-reactant. Ru CVD was carried out with bis(ethyl-π-cyclopentadienyl)ruthenium [$Ru(EtCp)_2$] and O_2 as a co-reactant. $Ru(EtCp)_2$ cannot be dissociated by thermal means alone; O_2 is required to decompose the precursor ligands. The difference in precursor chemistry may lend insight into the role iodine plays in nucleation and growth of CVD films.

This chapter reports film growth studies employing (2,4-dimethylpentadienyl)(ethylcyclopentadienyl)Ru, also called Ru(DMPD)(EtCp) or DER, on SiO_2/Si(100), both with and without iodine addition. Like many of the organometallic Ru precursors, DER also requires O_2 as a co-reactant to compose the precursor ligands.

3.2. EXPERIMENTAL DETAILS

Film growth was carried out in a hot-wall quartz chamber with operating pressures ranging from 17 to 1.3×10^3 Pa and temperature control up to 1475 K. The pressure was regulated by a diaphragm valve on the inlet of a mechanical pump and the temperature was regulated by a furnace controller. Ru films were deposited on chemically grown SiO_2 (350 nm)/Si(100) wafers supplied by Freescale Semiconductor. The precursor (2,4-dimethylpentadienyl)(ethylcyclopentadienyl)Ru [DER], supplied by Tosoh Co., was introduced into the chamber by bubbling Ar through it at 20 sccm. Because the vapor pressure of DER is sufficiently high (5.3 Pa at 333 K) [23], the saturator was kept at room temperature and no heating was necessary to deliver the precursor into the chamber. The oxygen co-reactant was introduced at 10 sccm. Films were grown at 575 K and a pressure of 40 Pa. The iodine source used was CH_3I (Sigma-Aldrich, 99.5%) and was introduced using a manual valve without carrier gas because of its high vapor pressure ($\sim 5.3 \times 10^4$ Pa at 298 K) [19]. CH_3I exposures of 10 s were introduced into the chamber after 15 min of film growth had occurred. Then the CH_3I was pumped away and Ru film growth was resumed until the desired film thickness was achieved. CH_3I was introduced after an initial growth time of 15 min because only sparse Ru islands were present on the substrate surface at this time (confirmed by scanning electron microscopy [SEM]), hence 15 min of growth time roughly corresponds to the initial stages of nucleation, and is well before the onset of island coalescence.

Film characterization included SEM [Zeiss Supra 40 VP], atomic force microscopy (AFM) [Digital Instrument Dimension 3100], and high resolution X-ray photoelectron spectroscopy (XPS) [Kratos Axis Ultra DLD]. Film thicknesses were determined by cross-section SEM.

3.3 RESULTS

A high resolution XPS depth profile of a 60 nm Ru film grown without CH_3I addition is shown in Fig. 3.1. The depth profile indicates that there is ~ 7% oxygen contamination in the bulk film, most likely a result of the oxygen co-reactant. Due to overlap between the Ru $3d_{3/2}$ and C 1s XPS peaks, it is very difficult to estimate the amount of carbon contamination in the film. One method that allows a crude estimate of carbon content involves fitting the 3d peaks and then calculating the ratio between the

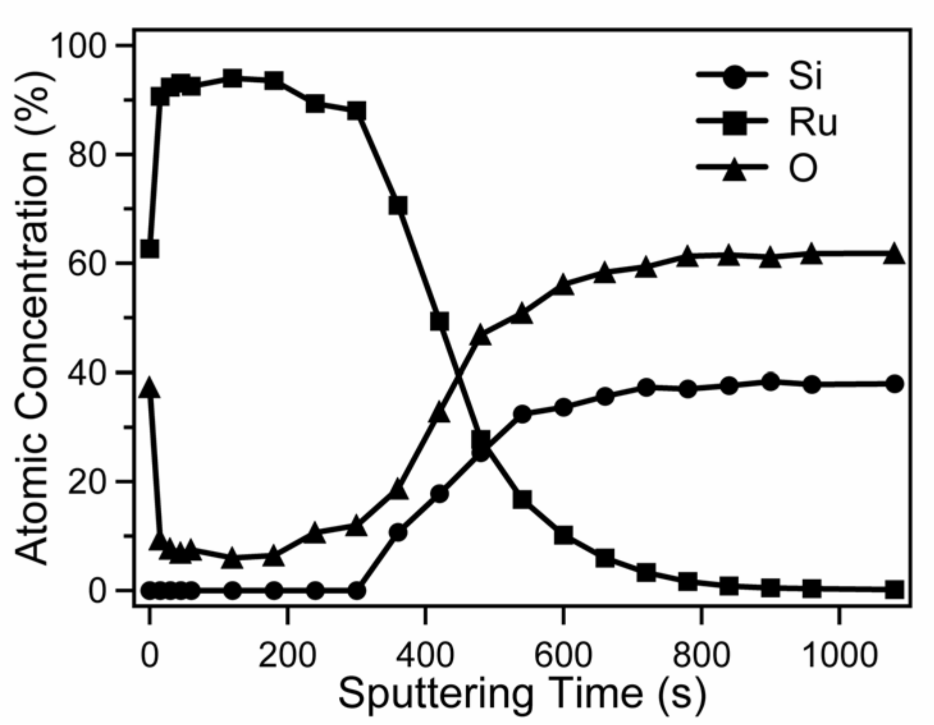

Figure 3.1. XPS depth profile for 60 nm Ru film grown without CH_3I addition.

$3d_{5/2}$ and $3d_{3/2}$ peaks. The theoretical Ru 3d ratio, based on spin-orbit coupling effects of the 3d electrons, is equal to 1.5 [24]. Ratio values less than 1.5 correspond to carbon in the films; however, small errors obtained in peak fitting can lead to large errors in estimating the carbon content. Nonetheless, this method of estimating carbon content was applied to 60 nm films grown both with and without CH_3I addition. High resolution Ru 3d XP spectra of the 60 nm films are shown in Fig. 3.2. These spectra were acquired after a 60 s sputter clean of the surface to remove adventitious carbon. Both films show Ru $3d_{3/2}$ and Ru $3d_{5/2}$ peaks at binding energies of 284.3 and 280.1 eV, respectively. These binding energies correspond to metallic Ru, indicating that the addition of CH_3I does not alter the formation of metallic Ru during film growth. In addition, both 60 nm films have Ru 3d ratios of 1.48, which corresponds roughly to 7% carbon in the films. Because both films have the same Ru 3d ratio, it appears that the addition of CH_3I does not significantly increase the amount of carbon in the films.

High resolution XPS was also used to investigate whether or not iodine segregates to the film surface during growth, in a manner similar to surfactants in epitaxial growth. Iodine segregation was observed by XPS in Cu CVD [13,14]; however, no iodine XPS signal was detected in Ru CVD [20]. Ru 3d and I 3d XP spectra after 15 min and 60 min of growth time are shown in Fig. 3.3. A growth time of 15 min corresponds to the initial stages of nucleation, when only sparse islands have formed on the substrate surface. CH_3I was introduced into the chamber after 15 min of growth time. As seen in Fig. 3.3a, only a small amount of Ru is detected after 15 min of growth, and the amount of iodine that adsorbs to this Ru is shown in Fig. 3.3b. A growth time of 60 min corresponds to a 22 nm film. In this case, CH_3I was introduced after 15 min of growth time, was pumped

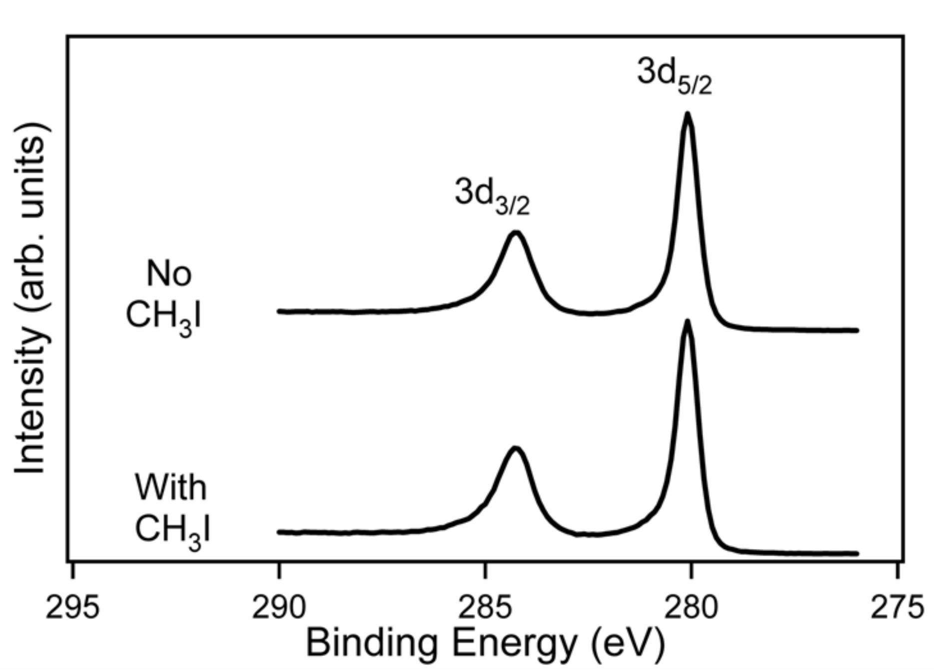

Figure 3.2. Ru 3d XP spectra for 60 nm films grown with and without CH_3I addition.

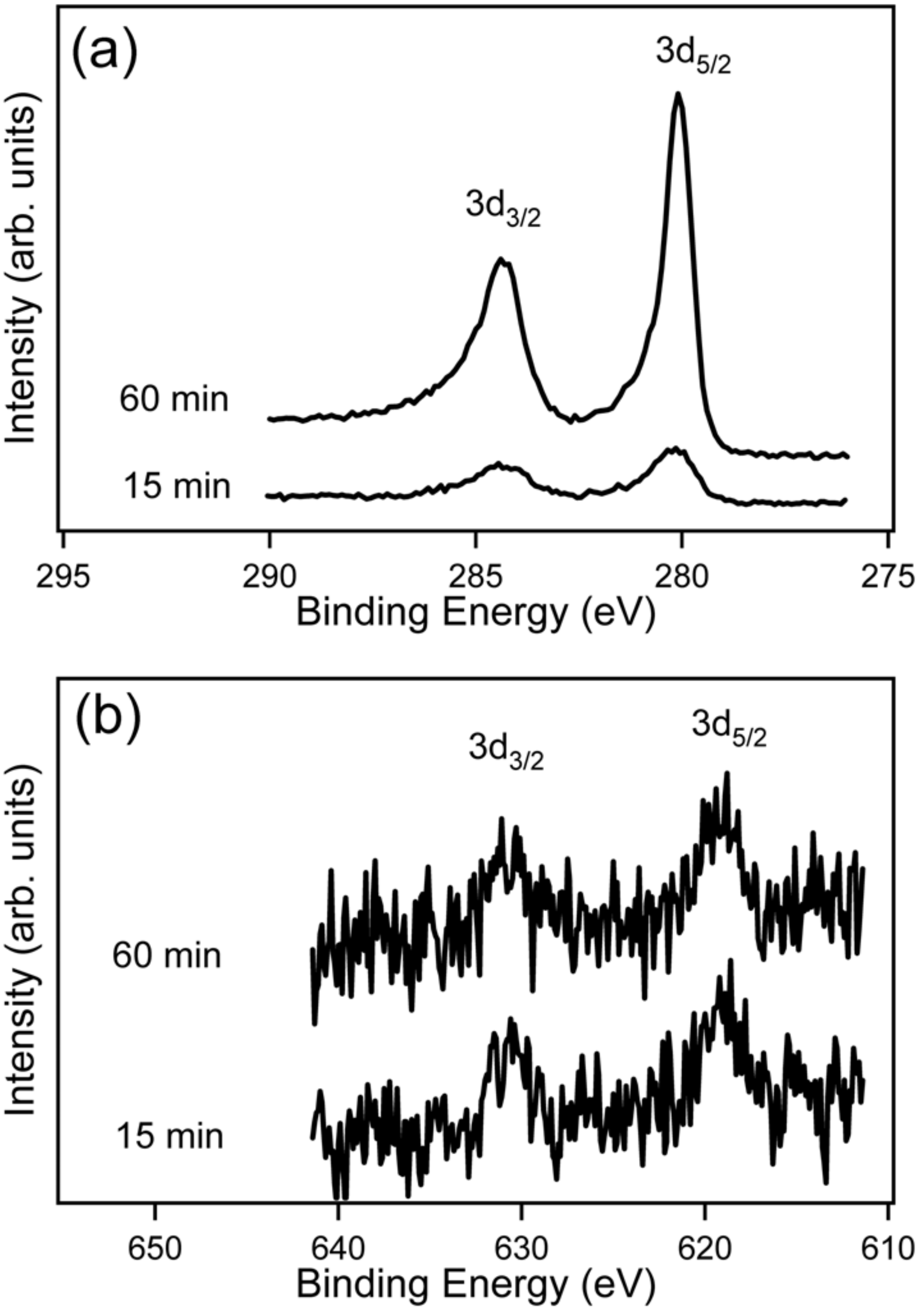

Figure 3.3. XP spectra after 15 min and 60 min of growth time for a) Ru 3d and b) I 3d. A growth time of 15 min corresponds to sparse islands on the surface and a growth time of 60 min corresponds to a 22 nm film.

away, and then the growth continued for another 45 min. As expected, the Ru XPS signal is much larger for the film grown for 60 min than for the sparse Ru islands that have nucleated after 15 min. In contrast, the iodine XPS signal for 60 min appears to be quite close to that of the 15 min signal. This indicates that some, if not all, of the iodine dosed to the Ru islands is segregating to the film surface. If the iodine stayed adsorbed to the Ru islands and was buried in the growing film, the iodine signal at the film surface would decrease and most likely attenuate completely.

Fig. 3.4 shows Ru 3d and I $3d_{3/2}$ XPS peak areas as a function of deposition time. Deposition time is reported in lieu of film thickness because it is difficult to assign a film thickness to 15 min and 30 min of growth time, both of which correspond to discontinuous Ru islands on the surface, prior to the onset of film coalescence. Both the Ru 3d and I $3d_{3/2}$ peak areas are normalized by the Si 2p peak area from a blank sample of SiO_2/Si(100) that was acquired on the same day as the Ru film was analyzed. This is to account for any irregularities in XPS sensitivity that may occur from acquiring scans on different days. Fig. 3.4a shows that the Ru 3d signal increases with deposition time, as expected. As the films get thicker, the Ru 3d peak area increases. Fig. 3.4b shows that the I $3d_{3/2}$ signal decreases with deposition time. This implies that some of the iodine is being buried in the film and some is segregating to the surface. If all of the iodine were segregating to the film surface during growth, the I $3d_{3/2}$ signal would be constant with deposition time.

However, it should be noted that XPS depth profiles of several films grown with CH_3I were carried out. In all cases, an iodine signal was acquired at the surface of the film, and this iodine signal completely attenuated after 60 s of sputtering. No iodine

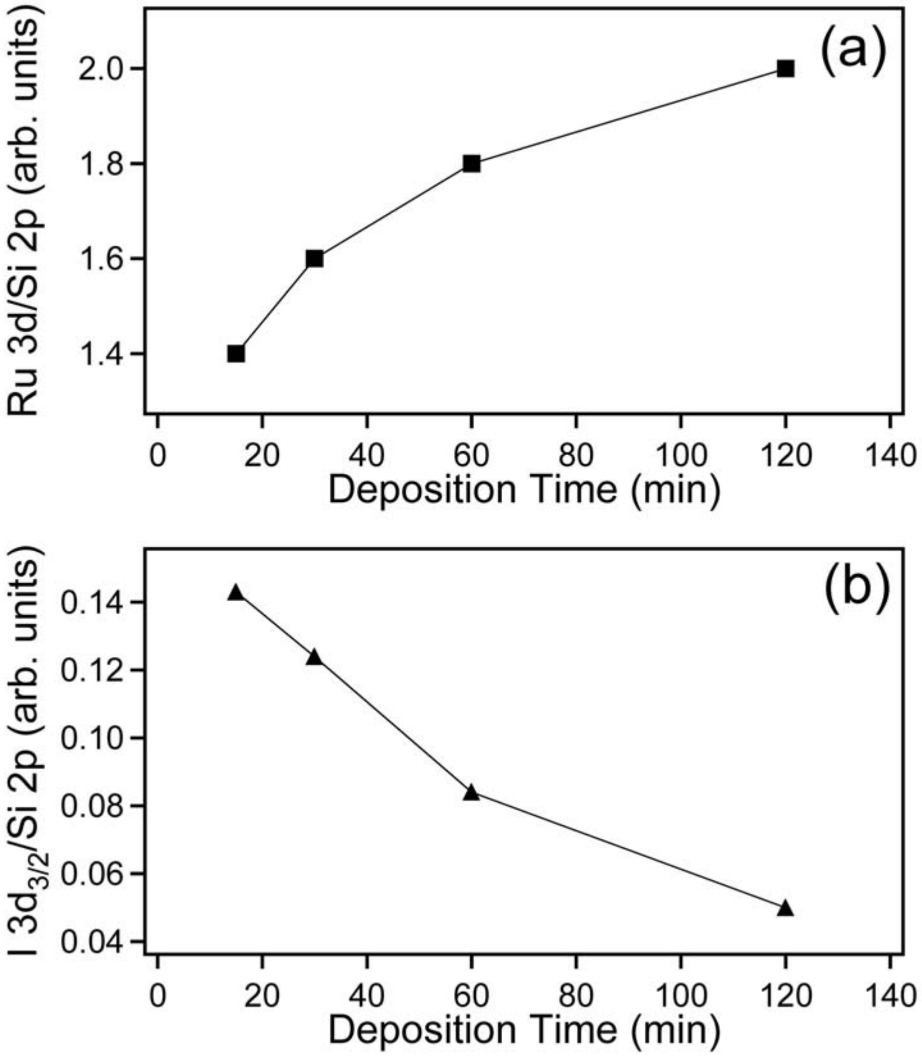

Figure 3.4. XPS peak areas for a) Ru 3d and b) I 3d$_{3/2}$ as a function of deposition time. The XPS peak areas are normalized by the Si 2p peak area from a bare sample of SiO_2/Si(100) that was acquired on the same day as the Ru film was analyzed in order to account for any irregularities in XPS sensitivity.

signal was obtained anywhere other than the film surface during the depth profiles. The XPS sensitivity factor for the I $3d_{5/2}$ peak is 1.4 times that of Ru 3d and 18.9 times that of Si 2p, and iodine concentrations of < 1% can be obtained by XPS. Thus any iodine concentrated in the bulk film should generate an XPS signal. Nonetheless, it appears that some of the iodine is segregating to the film surface and some is remaining in the bulk film.

Furthermore, the I $3d_{3/2}$ and I $3d_{5/2}$ peaks are at binding energies of 630.8 and 619.3 eV, respectively. These binding energies correspond to elemental iodine. As mentioned previously, the Ru 3d binding energies are consistent with metallic Ru. Neither the Ru 3d or I 3d signals show any XPS chemical shift, thus there is no formal bonding or electron donating or accepting between Ru and I.

The deposition rate as a function of film thickness for films grown both with and without CH_3I addition is shown in Fig. 3.5. The deposition rate was determined by getting a film thickness from cross-section SEM and dividing it by the total deposition time. In the case of Ru films growth without CH_3I addition, the deposition rate is essentially constant with respect to film thickness. In the case of CH_3I addition, the deposition rate is also constant with film thickness; however, the deposition rate is decreased from that of no CH_3I addition. It seems likely that the CH_3I is blocking active sites on the Ru, suppressing film growth. Furthermore, the decreased deposition rate provides further evidence that iodine segregates to the film surface during growth. If the iodine stayed adsorbed to the Ru islands and was buried in the growing film, the deposition rate may be depressed initially, but the effect of the iodine would be reduced with increasing deposition time. If the iodine were buried, it would be expected that for

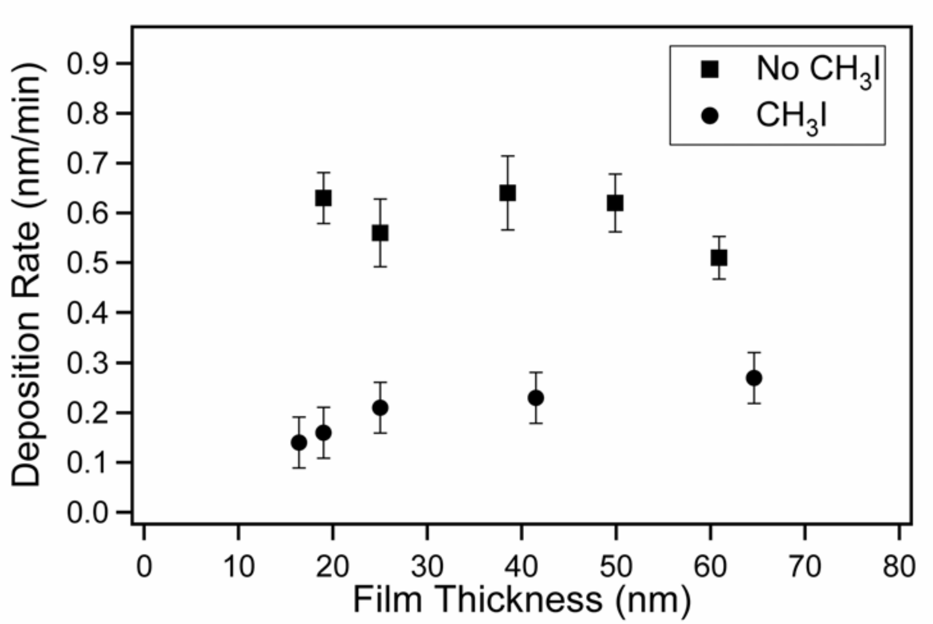

Figure 3.5. The deposition rate as a function of film thickness for films growth both with and without CH_3I addition. The deposition rate was determined by dividing film thickness from cross-section SEM by the total deposition time.

prolonged deposition times, the deposition rate for CH_3I addition would approach that of no CH_3I addition. However, with CH_3I addition, the deposition rate remained depressed for all growth times, indicating that the iodine segregated to the surface and blocked active sites throughout the entire film growth.

The addition of CH_3I also influenced nucleation of the films by blocking active sites. Fig. 3.6 shows plan view SEM images for 30 min of growth time, both with and without the addition of CH_3I. In the case of CH_3I addition, growth occurred for 15 min, then the CH_3I was introduced, pumped away, and then growth continued for another 15 min. After 30 min of growth time, the substrate is covered with Ru islands for both cases; however, for no addition, there are fewer islands (8.5×10^{10} cm^{-2}) than for CH_3I addition (18.3×10^{10} cm^{-2}). Furthermore, the size distribution of the islands differs greatly depending on whether or not an iodine source was used. The size distribution of the islands, summarized in Table 3.1, indicates that 89% of the islands are in the range 10-30 nm for CH_3I addition, while only 52% are in that range for no CH_3I addition. In addition, only 1% of the islands are > 30 nm for CH_3I addition, while 14% are > 30 nm for no CH_3I addition. This suggests that when an iodine source is introduced to the initially-formed islands, it inhibits their growth and allows time for additional nucleation to occur on the SiO_2 surface. In the case of no addition, the initially-formed islands grow much more rapidly than new islands are nucleated.

The iodine source promotes denser, more uniform nucleation, which results in films with denser, smaller grains. Plan view SEM images for both 25 nm and 60 nm films growth both with and without CH_3I addition are shown in Fig. 3.7. Simulations of

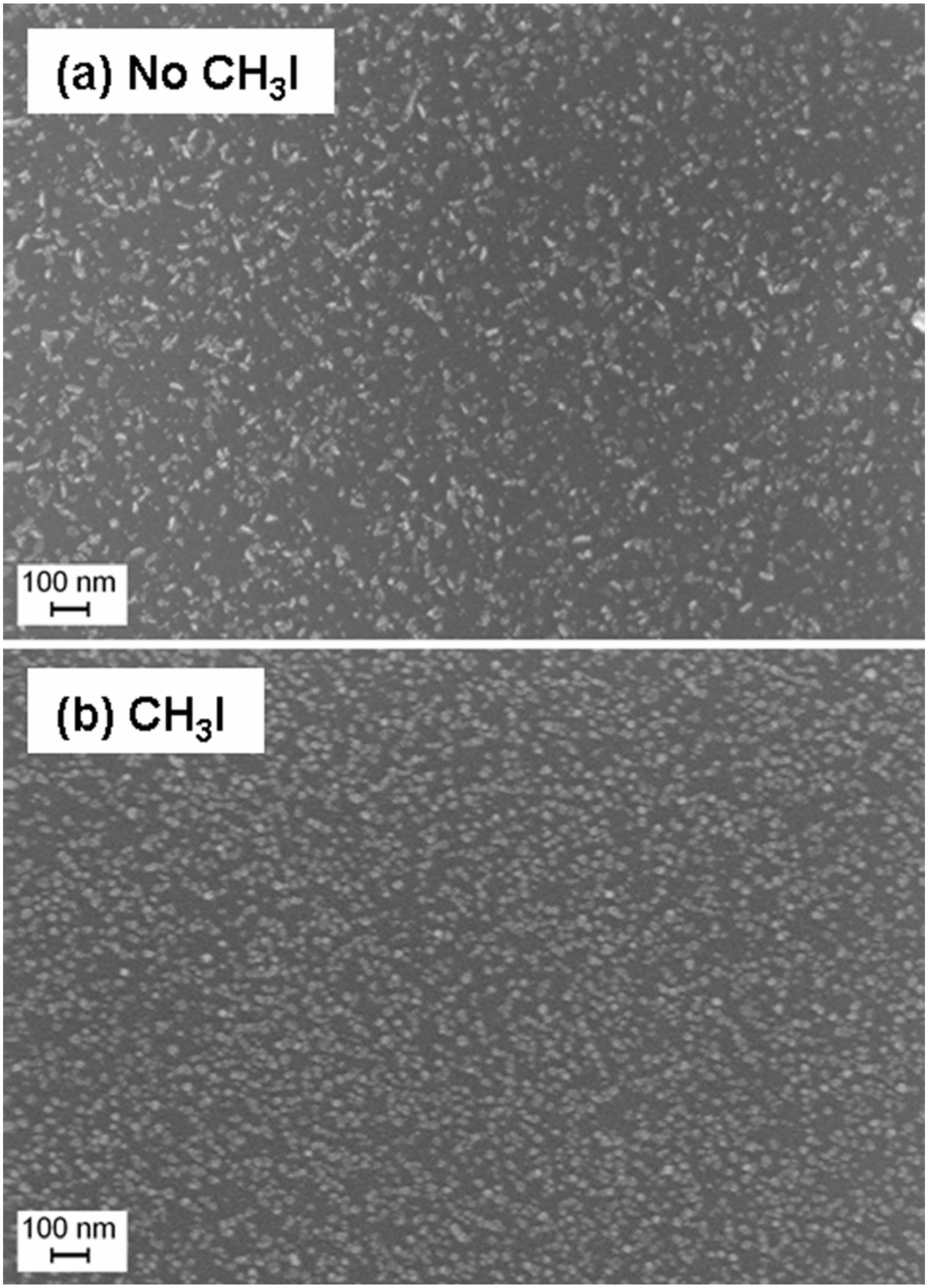

Figure 3.6. SEM images after 30 min of growth time for a) no CH_3I and b) CH_3I addition.

	No CH_3I	CH_3I
Total Islands	8.5×10^{10} cm^{-2}	18.3×10^{10} cm^{-2}
< 10 nm	34%	10%
10-30 nm	52%	89%
> 30 nm	14%	1%

Table 3.1. Size distribution of the Ru islands after 30 min of growth time both with and without the addition of CH_3I. For CH_3I addition, growth occurred for 15 min, then the CH_3I was introduced, pumped away, and then growth continued for another 15 min.

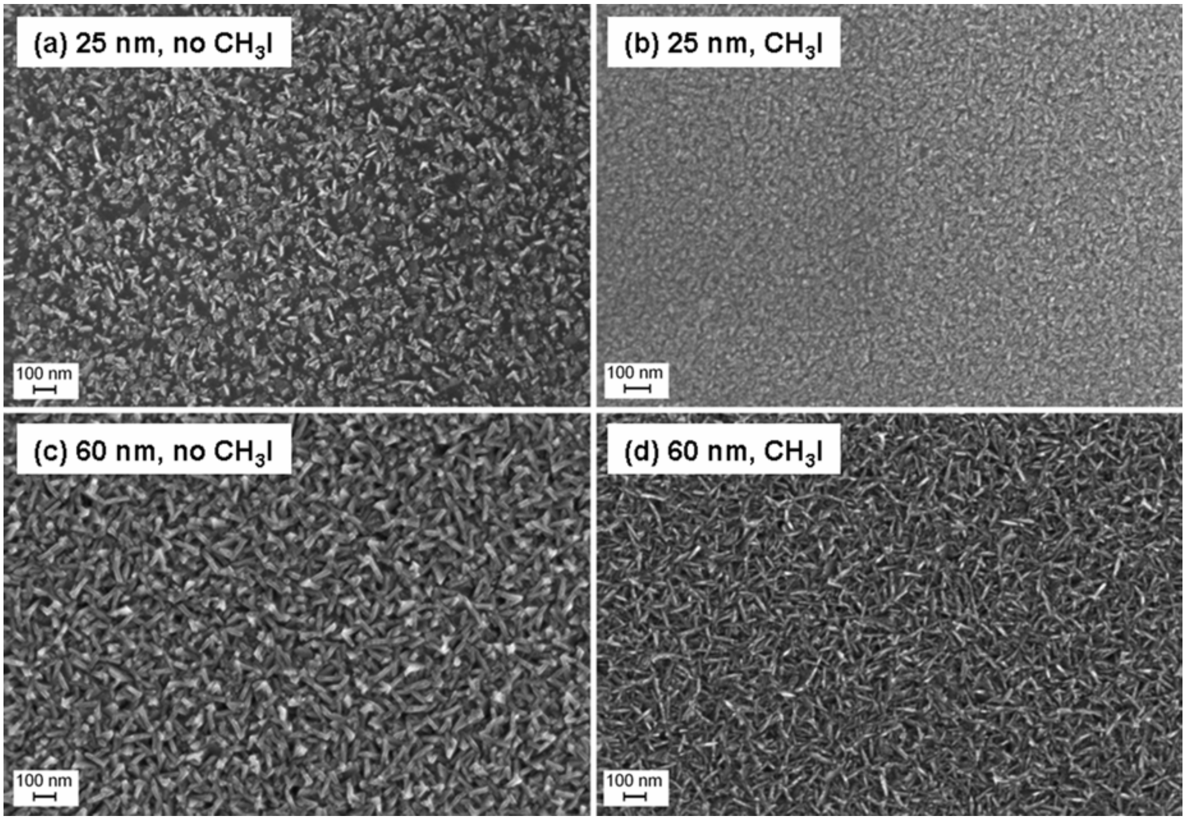

Figure 3.7. SEM images for films of a) 25 nm, no CH_3I, b) 25 nm, CH_3I, c) 60 nm, no CH_3I and d) 60 nm, CH_3I addition.

the growth dynamics of polycrystalline films with columnar structures have indicated that the nucleation of truncated-cube-shaped crystals results in the appearance of roof-like terminations in plan view analyses of film topography [25]. All of the Ru films appear to have roof-like terminations, although the shape of the grains is more evident for the thicker 60 nm films. It is clear from the SEM images that the introduction of CH_3I during the initial stages of growth leads to films with smaller, denser grains, although the shape of the grains is not altered by addition of the iodine source.

The enhanced nucleation density and smaller grains afforded by the iodine source also leads to improved film roughness. The root-mean-square (RMS) roughness of films grown both with and without the addition of CH_3I was determined by AFM. Fig. 3.8 shows the evolution of film roughness with respect to film thickness. No addition and CH_3I addition both result in the RMS roughness increasing with increasing film thickness, most likely due to thicker films having larger grains; however, the use of CH_3I reduces roughness at all thicknesses. In addition, AFM images for both 19 nm and 60 nm films grown both with and without CH_3I are shown in Fig. 3.9. The 19 nm films for no addition and CH_3I addition have RMS roughness values of 3.55 and 1.99 nm, respectively, while the 60 nm films have RMS roughness values of 8.42 and 5.62 nm, respectively. The AFM images also show smaller, denser grains with CH_3I addition; however, the grains appear to be spherical for all but the 60 nm film grown without CH_3I addition. It is known that surface data in AFM can be convoluted by the shape of the AFM tip. The crystal grains may erroneously appear as spherical when the size of the AFM tip is comparable to the size of the crystal grains [25]. Of the four films shown in Fig. 3.9, the 60 nm film grown without CH_3I addition has the largest grains, and the roof-

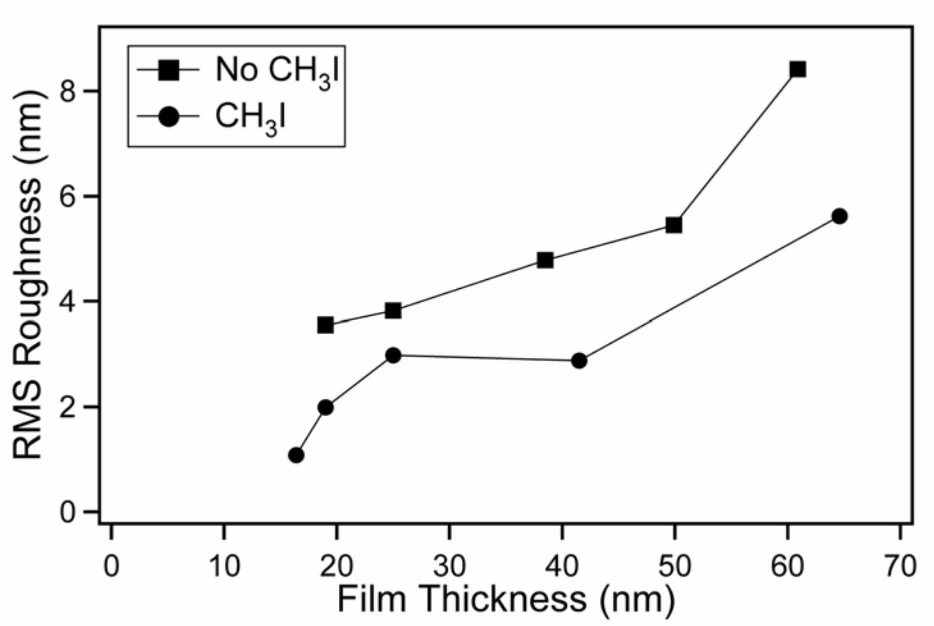

Figure 3.8. Film roughness determined by AFM both with and without CH_3I addition.

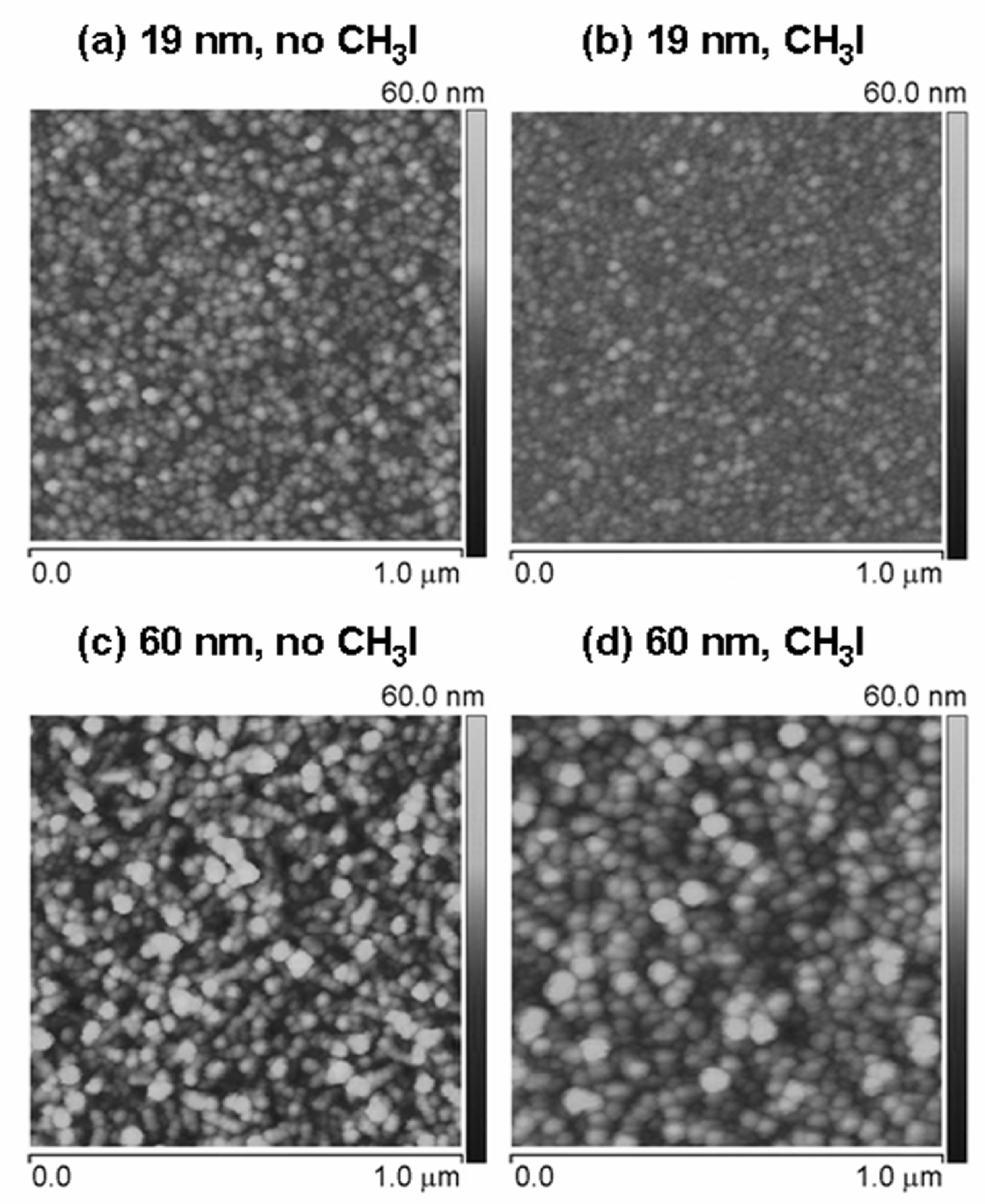

Figure 3.9. AFM images for films of a) 19 nm, no CH_3I, b) 19 nm, CH_3I, c) 60 nm, no CH_3I and d) 60 nm, CH_3I addition. The RMS roughness values are a) 3.55 nm, b) 1.99 nm, c) 8.42, and d) 5.62 nm.

like terminations observed in SEM begin to be evident in the AFM image. Nonetheless, the addition of CH_3I reduces grain size and RMS roughness.

3.4. DISCUSSION

SEM analyses indicate that the addition of an iodine source at the initial stages of nucleation promotes more abundant islands with a more uniform size distribution. It appears that the adsorbed iodine inhibits the growth of the initially-formed islands, which allows additional nucleation to occur on the SiO_2 surface. The adsorbed iodine is blocking growth sites on the Ru islands. XPS depth profiles reveal that the majority of the adsorbed iodine segregates through the film to the surface during growth. Furthermore, the deposition rate is depressed throughout the entire film growth, indicating that the site blocking effect is active on the Ru surface during the entire deposition.

As mentioned previously, CH_3I decomposes into adsorbed CH_3 and I on Ru. The majority of the hydrocarbons desorb as CH_4 at 170 K, although some residual carbon remains on the surface [21]. This residual carbon could also contribute to the site blocking effect. However, it is worth noting that the addition of CH_3I to the initially-formed Ru islands did not increase the amount of carbon in the films as compared with no CH_3I addition, as evidenced by XPS. Thus it is expected that any residual carbon adsorbed to the Ru islands as a result of the CH_3I exposure is minor and the site blocking effect is primarily due to the adsorbed iodine. Thus at the film growth temperature of 575 K, the CH_3I exposure leaves chemisorbed iodine and an insignificant amount of residual carbon on the Ru islands.

Furthermore, it has been shown that CH_3I reversibly adsorbs to SiO_2 through a hydrogen bond between free surface hydroxyl groups and the iodine atom below room temperature; however, once the CH_3I has been evacuated from the chamber, no CH_3I remains adsorbed to the SiO_2 [26]. To confirm that no CH_3I irreversibly adsorbs to or decomposes on the SiO_2 during our film growth conditions, CH_3I was exposed to SiO_2 and the SiO_2 was then analyzed in XPS. No traces of iodine were found and the amount of adventitious carbon was not increased from typical background levels. Thus a CH_3I exposure at the film growth temperature of 575 K results in adsorbed atomic iodine on the Ru islands, but does not adsorb to the SiO_2 once the CH_3I has been pumped away after the 10 s dose.

Like many of the related precursors containing cyclopentadienyl and pentadienyl ligands, such as $Ru(Cp)_2$ and $Ru(EtCp)_2$, film growth with the DER precursor requires O_2 as a co-reactant. In the case of CVD with $Ru(EtCp)_2$ and O_2, Kang et al. used both thermodynamic calculations and film growth studies to show that a sufficient amount of oxygen is needed to crack the Ru-ligand bonds in order for film growth to occur [27]. Ultra-high vacuum (UHV) surface science studies have shown that oxygen dissociatively chemisorbs on Ru(001) [28], and it is believed that during Ru film growth, oxygen dissociates on the Ru film surface and this adsorbed atomic oxygen decomposes the ligands of the precursor. In fact, in the case of ALD with $Ru(Cp)_2$ and O_2, Aaltonen et al. completed very detailed mechanistic studies on the ALD mechanism, which showed that during the oxygen pulse, a layer of adsorbed atomic oxygen forms on the growing Ru surface and this oxygen partially decomposes the ligands of the $Ru(Cp)_2$ during the $Ru(Cp)_2$ pulse. During the next oxygen pulse, complete oxidation of the Cp ligands occurs and then a new oxygen layer is formed on the Ru [29]. Furthermore, in the case of ALD with $Ru(EtCp)_2$ and O_2, Kwon et al. showed that using a hydrogen plasma to remove the adsorbed oxygen from the Ru after every oxygen pulse drastically reduced the film thickness/cycle [30]. It is clear that during CVD and ALD film growth, oxygen dissociates on the growing Ru and this atomic oxygen is necessary to decompose the ligands of the incoming precursor. Thus there are two adsorption sites necessary for film growth: precursor adsorption sites and oxygen dissociation sites.

In the case of iodine adsorption during Ru film growth, the iodine may be blocking either DER adsorption sites or oxygen dissociation sites. In recent UHV surface science studies from our group of DER on bare and iodine pre-covered Ta, it has been shown that the adsorbed iodine promotes the adsorption of molecular DER [31]. When DER is exposed to a bare Ta surface held at 573 K (essentially the same temperature as the film growth studies in this chapter), minor accumulation of hydrocarbons occurs, but no Ru or molecular DER adsorbs to the surface. When DER is exposed to iodine pre-covered Ta at 573 K, DER adsorbs molecularly. Thus the adsorbed iodine both blocks the dissociation of DER into hydrocarbon residue and promotes DER adsorption. The adsorbed iodine enhances the vertical potential of the Ta surface, which allows more of the impinging DER molecules to adsorb. It is likely that adsorbed iodine during Ru film growth behaves in a similar manner and promotes the adsorption of DER. It appears that the iodine promotes DER adsorption as opposed to blocking DER adsorption sites.

Furthermore, it has also been shown that an iodine adlayer passivates Ru(001) against hydroxide, chemisorbed oxygen, and oxide formation during exposure to air [17]. In addition, an iodine adlayer passivates polycrystalline Ru against oxide formation, including chemisorbed oxygen, during exposure to water vapor [17]. Kis et al. have shown that preadsorbed O atoms on Ru(001) lower the thermal desorption temperature of iodine by almost 200 K, which they attribute to the repulsive interaction between oxygen and iodine [22]. Thus it is likely that iodine is blocking oxygen dissociation sites during Ru film growth, possibly due to electrostatic repulsion between I and O.

In the case of Ru films grown from DER and O_2, it appears that adsorbed iodine blocks oxygen dissociation sites, depressing the film growth. Furthermore, iodine increases adsorption of DER to the growing Ru islands, and the additional adsorption of DER may block additional sites needed to dissociate O_2. The decrease in the available supply of adsorbed surface oxygen needed to decompose the precursor ligands results in stunted growth of the initially-formed Ru islands, which leads to denser, more uniform nucleation and ultimately smaller-grained, smoother films. In effect, new iodine-free islands nucleate after CH_3I exposure and these grow along with the slower growing I-covered Ru islands until all islands coalesce into a film. On the other hand, adsorbed iodine increases the deposition rate of Cu films deposited from Cu^I(hfac)(vtms), which thermally decomposes [13,14]. Hwang et al. suggest that iodine weakens the Cu^I-hfac bond [13]. Ultimately, the major difference between the role of iodine in Ru versus Cu CVD is that in Ru CVD, iodine blocks dissociation sites for the oxygen co-reactant, while no significant site blocking occurs in Cu CVD. Furthermore, as also observed by Kim et al. [20], the metal-ligand bonds in the DER are much stronger than the metal-ligand bonds in Cu^I(hfac)(vtms) and thus iodine is able to influence precursor dissociation in the case of Cu CVD, but not in the case of Ru CVD.

3.5. CONCLUSION

The addition of CH_3I to CVD Ru film growth resulted in more populous, uniform nucleation, which ultimately lead to smaller-grained, smoother films. The CH_3I did not significantly increase the amount of carbon contamination in the films. The majority of the adsorbed iodine segregated through the films to the surface during growth, resulting in a continuously depressed deposition rate. The adsorbed iodine blocks oxygen dissociation sites, reducing the oxygen supply available to decompose the ligands of the DER precursor, which slows the growth of the initially-formed islands and allows new islands to nucleate, and continually depresses film growth throughout the deposition.

3.6 REFERENCES

[1] I. Goswami, R. Laxman, Semicond. Int. 27 (2004) 49.

[2] H. Kim, Surf. Coat. Technol. 200 (2006) 3104.

[3] J. Shin, A. Waheed, W. A. Winkenwerder, H.-W. Kim, K. Agapiou, R. A. Jones, G. S. Hwang, J. G. Ekerdt, Thin Solid Films 515 (2007) 5298.

[4] L. B. Henderson, J. G. Ekerdt, Thin Solid Films 517 (2009) 1645.

[5] J. Papadatos, S. Consiglio, S. Skordas, E. T. Eisenbraun, A. E. Kaloyeros, J. Peck, D. Thompson, C. Hoover, J. Mater. Res. 19 (2004) 2947.

[6] P. G. Ganesan, M. Eizenberg, C. Dornfest, J. Electrochem. Soc. 149 (2002) G510.

[7] Y. Matsui, M. Hiratani, T. Nabatame, Y. Shimamoto, S. Kimura, Electrochem. Solid-State Lett. 4 (2001) C9.

[8] K. C. Smith, Y.-M. Sun, N. R. Mettlach, R. L. Hance, J. M. White, Thin Solid Films 376 (2000) 73.

[9] S. Y. Kang, C. S. Hwang, H. J. Kim, J. Electrochem. Soc. 152 (2005) C15.

[10] K. Choi, J. Lim, S. Roy, C. Lee, Jpn. J. Appl. Phys 42 (2003) 5539.

[11] H. Han, J. J. Kim, D. Y. Yoon, J. Vac. Sci. Technol. A 22 (2004) 1120.

[12] S.-E. Park, H.-M. Kim, K.-B. Kim, S.-H. Min, Electrochem. Solid-State Lett. 1 (1998) 262.

[13] E. S. Hwang, J. Lee, Chem. Mater. 12 (2000) 2076.

[14] E. S. Hwang, J. Lee, Electrochem. Solid-State Lett. 3 (2000) 138.

[15] J.-L. Lin, B. E. Bent, J. Vac. Sci. Technol. A 10 (1992) 2202.

[16] J. Camarero, L. Spendeler, G. Schmidt, K. Heinz, J. J. de Miguel, R. Miranda, Phys. Rev. Lett. 73 (1994) 2448.

[17] J. Liu, J. Lei, N. Magtoto, S. Rudenja, M. Garza, J. A. Kelber, J. Electrochem. Soc. 152 (2005) G115.

[18] H.-B. Lee, D.-K. Kwak, S.-W. Kang, Electrochem. Solid-State Lett. 8 (2005) C39.

[19] J. J. Kim, D. H. Jung, M. S. Kim, S. H. Kim, D. Y. Yoon, Thin Solid Films 409 (2002) 28.

[20] J. J. Kim, M. S. Kim, D. Y. Yoon, Chem. Vap. Deposition 9 (2003) 105.

[21] Y. Zhou, M. A. Henderson, W. M. Feng, J. M. White, Surf. Sci. 224 (1989) 386.

[22] A. Kis, J. Kiss, F. Solymosi, Surf. Sci. 459 (2000) 149.

[23] T. Shibutami, K. Kawano, N. Oshima, S. Yokoyama, H. Funakubo, Mat. Res. Soc. Symp. Proc. 748 (2003) 111.

[24] H. Kim, I. Rabelo de Moraes, G. Tremiliosi-Filho, R. Haasch, A. Wieckowski, Surf. Sci. 474 (2001) L203.

[25] O. Nilsen, O. B. Karlsen, A. Kjekshus, H. Fjellvåg, Thin Solid Films 515 (2007) 4538.

[26] K. C. McGee, M. D. Driessen, V. H. Grassian, J. Catal. 159 (1996) 69.

[27] S. Y. Kang, K. H. Choi, S. K. Lee, C. S. Hwang, H. J. Kim, J. Electrochem. Soc. 147 (2000) 1161.

[28] M. C. Wheeler, D. C. Seets, C. B. Mullins, J. Chem. Phys. 105 (1996) 1572.

[29] T. Aaltonen, Antti Rahtu, M. Ritala, M. Leskelä, Electrochem. Solid-State Lett. 6 (2003) C130.

[30] O.-K. Kwon, S.-H. Kwon, H.-S. Park, S.-W. Kang, J. Electrochem. Soc. 151 (2004) C753.

[31] K. M. Thom, J. G. Ekerdt, Surf. Sci. 603 (2009) 920.

Chapter 4: Ultra-smooth Ru Films From $Ru_3(CO)_{12}$ Deposited by Chemical Vapor Deposition

4.1 INTRODUCTION

The scaling of dimensions in microelectronic devices results in an increased need to develop smooth, ultra-thin films that allow conformal deposition in high-aspect ratio features. Ru and alloys of Ru with phosphorus have been considered for use in applications such as barrier and copper seed layers in back end processing [1,2]. Ru is a desirable material in microelectronics because it has properties such as low electrical resistivity, high thermal and chemical stability, and negligible solubility with Cu [3], and Ru is being considered as a liner material that should both prevent diffusion and enable copper deposition. For Ru to be used as a diffusion barrier material, it is essential to minimize grain boundaries, as Cu diffusion occurs more rapidly through grain boundaries than through the bulk material [1]. In addition, the Ru film must be smooth and highly resistive to allow electroplating of Cu [3,4].

Although Ru has many promising properties, certain limitations must be overcome in the deposition of Ru films. Ru films often have polycrystalline columnar structure with sizeable grain boundaries and are usually very rough [5,6]. In ultra-thin films, large surface roughness leads to a significant increase in resistivity [7,8]. Several methods may be used to deposit Ru films, and each comes with certain advantages and limitations.

Physical vapor deposition (PVD) is a technique in which the directionality of the atoms traveling towards the substrate during growth causes step shadowing and makes it very difficult to deposit conformal films in high-aspect ratio features. However, PVD growth typically follows a two-dimensional (2D) growth mode, which leads to very smooth films. Currently, the diffusion barrier and seed layer are a Ta/TaN bi-layer followed by a copper seed layer, both deposited by PVD [4].

In contrast, chemical vapor deposition (CVD) is a technique in which the non-directional nature of the reactant gas flux at the substrate surface allows conformal deposition in high-aspect ratio features. However, CVD growth follows a three-dimensional (3D) growth mode, which may lead to films with excessive surface roughness, thus PVD films are typically smoother than CVD films [6]. In the case of Ru, both PVD and CVD films often show undesirable polycrystalline columnar structure. However, it is expected that CVD may eventually replace PVD as the deposition technique for the liner material due to significant improvements in film conformality [3,4].

This chapter reports growth studies of both CVD Ru films deposited from $Ru_3(CO)_{12}$ and PVD Ru films. It is shown that the CVD Ru films are smoother than those of PVD Ru and exhibit little to no polycrystalline columnar structure.

In addition, Nilsen et al. have published a series of articles on the simulation of the growth of thin films from various seed objects, such as spheres, cubes, octahedra, truncated cubes, and tetragonal crystallites [9-12]. The shape of the different seed objects, or nuclei, that form are determined by the different growth precursors used and/or the crystal structure of the evolving material. Nilsen et al. have shown that the different types of crystal shapes forming each island during nucleation significantly impact both growth dynamics and the topography and surface roughness of the resulting films. This chapter will also address the shape of the seed objects and the resulting topography and surface roughness of Ru and RuO_2 films.

4.2 EXPERIMENTAL DETAILS

4.2.1 Film Growth for CVD vs. PVD Comparison

CVD Ru film growth was carried out in a hot-wall quartz chamber with operating pressures ranging from 0.125 – 10 torr and temperature control up to 1475 K. The pressure was regulated by a diaphragm valve on the inlet of a mechanical pump and the temperature was regulated by a furnace controller. The precursor, $Ru_3(CO)_{12}$ (Sigma-Aldrich, 99%), was heated to 353 K to obtain sufficient vapor pressure and was delivered to the chamber using 5 sccm Ar carrier gas through lines that were heated 10 K higher than the saturator temperature to prevent precursor condensation. Films were grown at 575 K and pressures of 80-100 mtorr.

In the hot-wall CVD system, Ru growth occurs on the heated chamber walls during deposition. After every deposition, a cleaning cycle was performed in order to remove the metallic Ru deposit from the chamber walls. Cleaning was necessary to facilitate effective substrate heating during CVD. In order to clean the tube, it was heated to 1248 K while 70 sccm of O_2 was flowed through. The Ru deposit was removed as volatile Ru-oxides.

PVD Ru film growth was carried out by DC magnetron sputtering in 20 sccm of Ar with 20 W power. The pressure in the PVD chamber was maintained at 10 mtorr during sputter depositions.

All Ru films were deposited on chemically grown SiO_2 (350 nm)/Si(100) wafers supplied by Freescale Semiconductor.

Film characterization included *ex situ* X-ray photoelectron spectroscopy (XPS) [Physical Electronics 3057; Mg K_α], scanning electron microscopy (SEM) [Zeiss Supra 40 VP], high resolution SEM [Hitachi S-5500], and atomic force microscopy (AFM) [Digital Instrument Dimension 3100]. Film thicknesses were determined by high resolution cross-section SEM.

4.2.2 Film Growth for CVD Films With Differing Seed Objects

CVD film growth was carried out using the system described in Section 4.2.1. Ru films deposited with $Ru_3(CO)_{12}$ are described in Section 4.2.1. Additionally, Ru and RuO_2 films were deposited using the precursor (2,4-dimethylpentadienyl)(ethylcyclopentadienyl)Ru, also called Ru(DMPD)(EtCp) or DER, supplied by Tosoh Co. DER was introduced into the chamber by bubbling Ar through it at 20 sccm. Because the vapor pressure of DER is sufficiently high, the saturator was kept at room temperature and no heating was necessary to deliver the precursor into the chamber. In order to deposit metallic Ru, the oxygen co-reactant was introduced at 10 sccm. In order to deposit RuO_2, the oxygen co-reactant was introduced at 20 sccm. Films were grown at 575 K and a pressure of 300 mtorr. All Ru and RuO_2 films were deposited on chemically grown SiO_2 (350 nm)/Si(100) wafers supplied by Freescale Semiconductor.

Film characterization included *ex situ* high resolution XPS [Kratos Axis Ultra DLD], SEM [Zeiss Supra 40 VP], and AFM [Digital Instrument Dimension 3100]. Film thicknesses were determined by cross-section SEM.

4.3 RESULTS AND DISCUSSION

4.3.1 CVD vs. PVD Ru Films

XPS analyses indicate that Ru films grown using $Ru_3(CO)_{12}$ are metallic Ru with < 1% oxygen contamination. Fig. 4.1 shows a Ru 3d XP spectrum for a 28 nm film. The Ru $3d_{3/2}$ and Ru $3d_{5/2}$ peaks are at binding energies of 284.3 and 280.2 eV, respectively. These binding energies are consistent with metallic Ru. Due to overlap between the Ru $3d_{3/2}$ and C 1s XPS peaks, it is very difficult to estimate the amount of carbon contamination in these films. One method that allows a crude estimate of carbon content involves fitting the 3d peaks and then calculating the ratio between the $3d_{5/2}$ and $3d_{3/2}$ peaks. The theoretical Ru 3d ratio, based on spin-orbit coupling effects of the 3d electrons, is equal to 1.5 [13]. Ratio values less than 1.5 correspond to carbon in the films; however, small errors obtained in peak fitting can lead to large errors in estimating the carbon content. Nonetheless, this method of estimating carbon content was applied to the films in this study and indicates that there is about ~ 10-20% carbon contamination.

SEM analyses indicate that films grown with $Ru_3(CO)_{12}$ are very smooth and show very little of the columnar structure that is typical for Ru films. Fig. 4.2 shows SEM images for 9 nm and 13 nm films. Both films are very smooth with an average grain size of < 10 nm. In contrast, PVD Ru films show a rougher topography and distinct polycrystalline columnar structure. Fig. 4.3. shows SEM images for 20 and 50 nm PVD

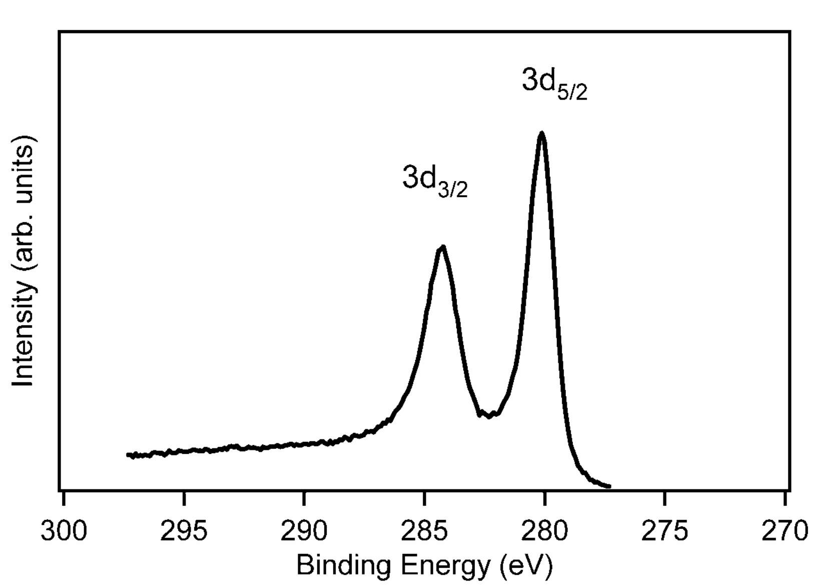

Figure 4.1. Ru 3d XP spectrum for 28 nm film grown with $Ru_3(CO)_{12}$.

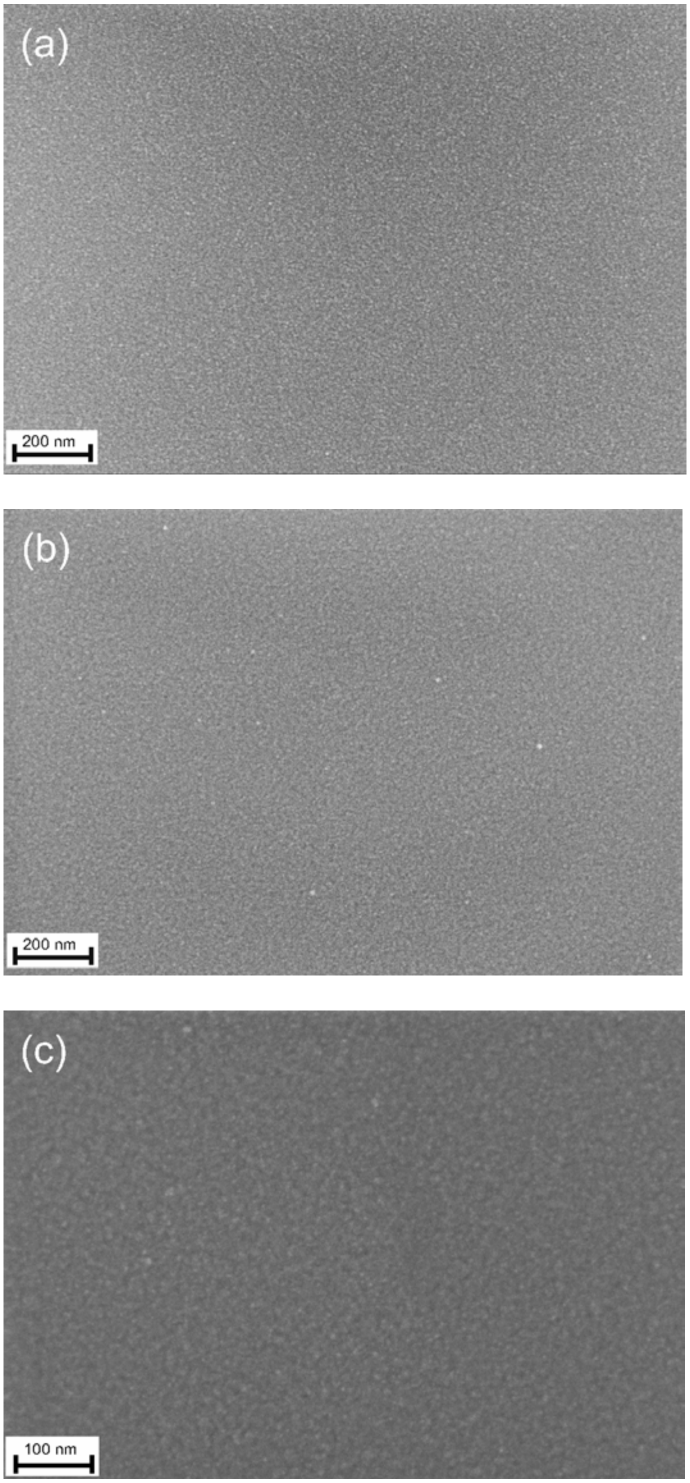

Figure 4.2. SEM images for films of a) 9 nm, b) 13 nm (lower magnification), and c) 13 nm (higher magnification) for Ru films grown with $Ru_3(CO)_{12}$.

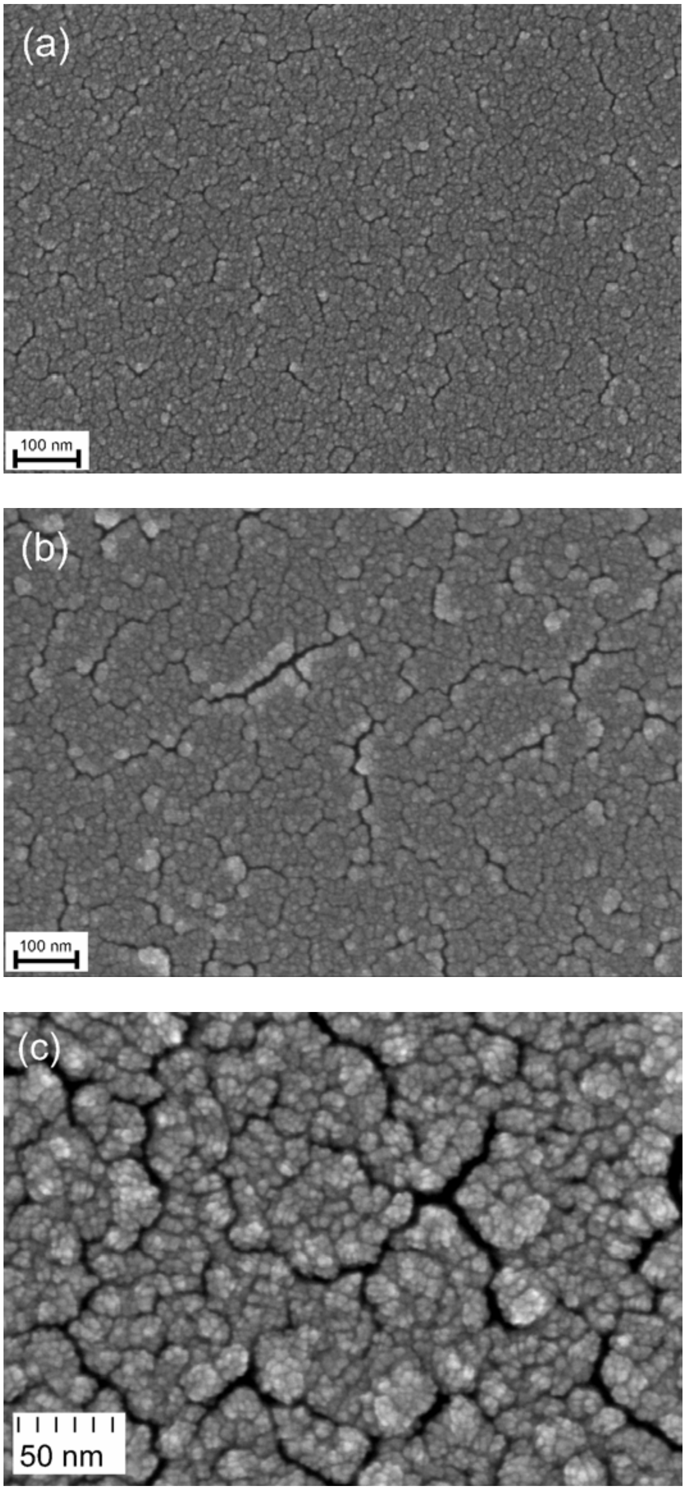

Figure 4.3. SEM images for films of a) 20 nm, b) 50 nm (lower magnification), and c) 50 nm (higher magnification) for Ru films grown by PVD.

films. The PVD films suffer from high residual stress, which has resulted in significant surface cracking. PVD films often have residual stress due to the differences in the expansion coefficient between the film and substrate (mechanical stresses) as well as stress due to rapid solidification of adatoms (growth stresses) [14]. The cross-sectional SEM images shown in Fig. 4.4 indicate that the CVD films are smooth with no columnar grain structure, while the PVD films show distinct polycrystalline columnar grains.

The very smooth surface morphology of the CVD films results in very low surface roughness measured by AFM as compared with PVD films. A comparison of roughness values between films must be done at the same film thickness because as film thickness increases, roughness also increases. Fig. 4.5. shows AFM images for a 28 nm CVD and 20 nm PVD film. In spite of the surface cracking, the 20 nm PVD film has low root-mean-square (RMS) roughness of 1.06 nm. However, the CVD film has even lower surface roughness of 0.63 nm. Both CVD and PVD films were deposited on 350 nm SiO_2 with a roughness of 0.19 nm. Although the CVD film is 8 nm thicker than the PVD film, the roughness is significantly lower.

Fig. 4.6. shows the evolution of film roughness with respect to film thickness for the CVD and PVD films. Fig. 4.6a shows that the CVD films increase in roughness from 0.40 to 0.63 nm with increasing film thickness from 9-28 nm, while the PVD films increase in roughness from 0.11 to 3.36 nm for film thicknesses of 3.5-50 nm. Fig. 4.6b allows a comparison of the CVD and PVD films over a range of thicknesses; the CVD films are significantly smoother than the PVD films at all thicknesses.

AFM and SEM analyses indicate that the CVD Ru films are very smooth with little columnar grain structure. The morphology of these films is significantly influenced

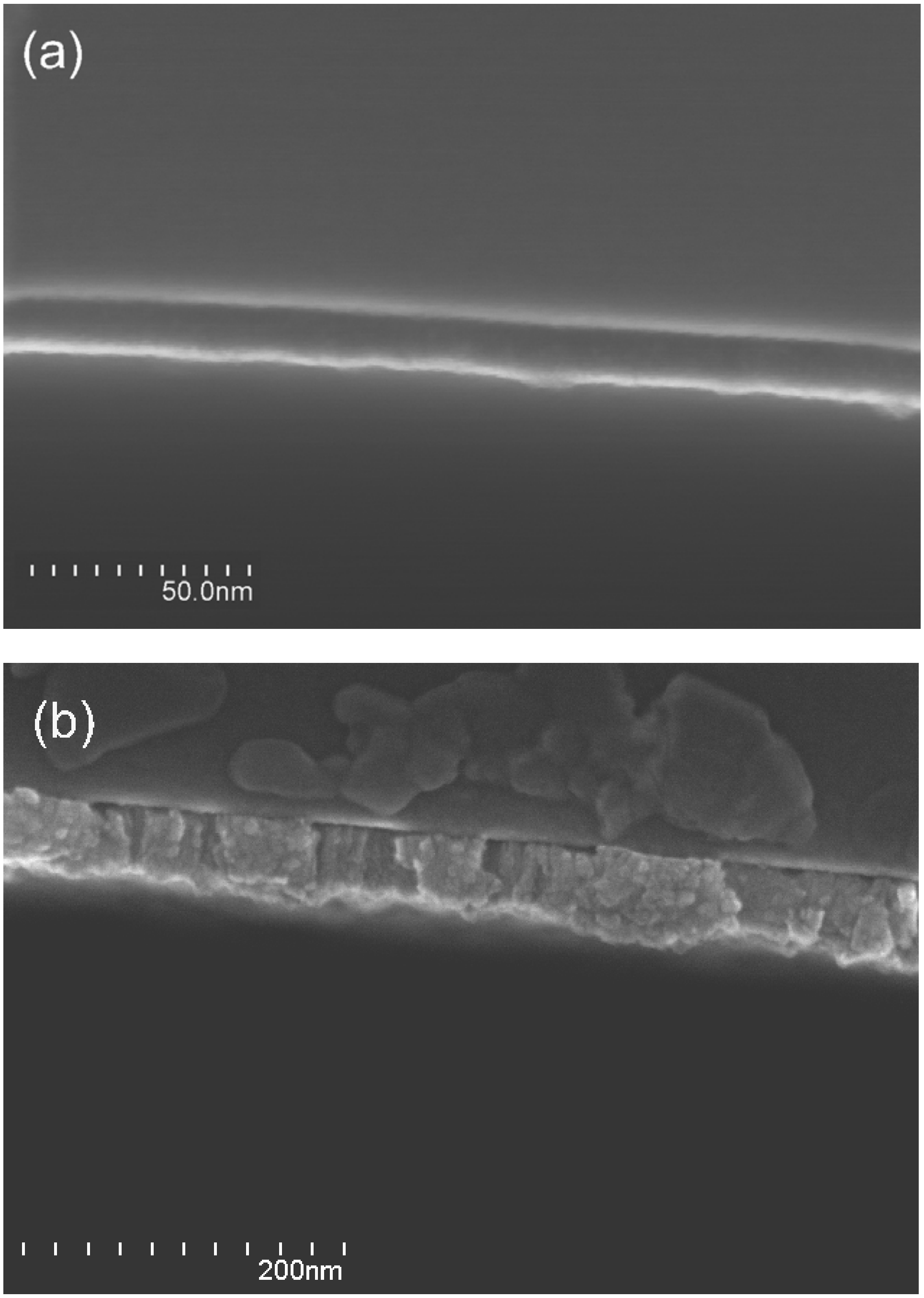

Figure 4.4. Cross-sectional SEM images for Ru films on SiO_2/Si of a) 13 nm grown with $Ru_3(CO)_{12}$, and b) 50 nm grown by PVD.

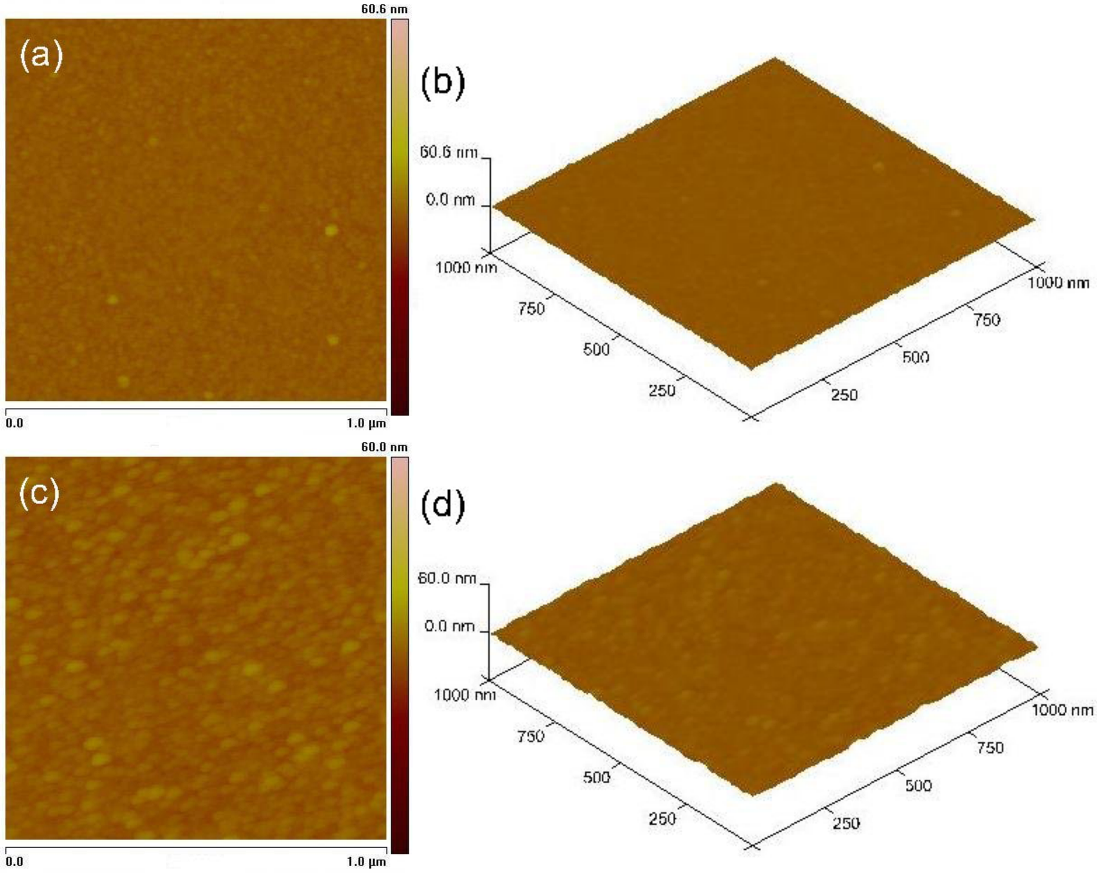

Figure 4.5. AFM images for films of a,b) 28 nm grown with $Ru_3(CO)_{12}$ and c,d) 20 nm grown by PVD. The RMS roughness values are a) 0.63 nm and b) 1.06 nm.

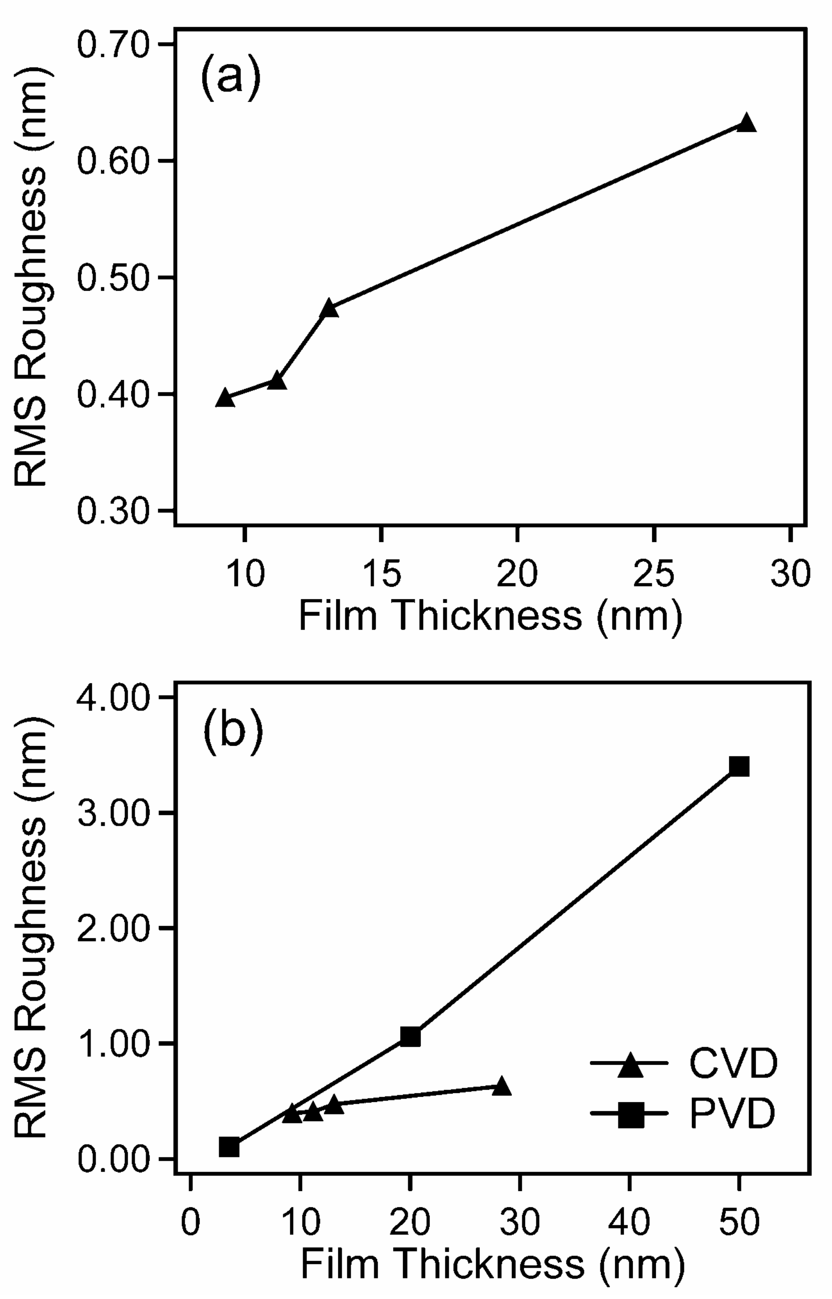

Figure 4.6. Film roughness determined by AFM for Ru films grown with a) $Ru_3(CO)_{12}$ and b) $Ru_3(CO)_{12}$ and PVD. The $Ru_3(CO)_{12}$ is shown in a) with a scale that allows more careful examination of the increase in roughness with film thickness.

by precursor decomposition in the hot-wall CVD system. $Ru_3(CO)_{12}$ enters the heated quartz tube and some precursor reacts on the chamber walls before it reaches the SiO_2 substrate. During growth, Ru is deposited on the chamber walls, as evidenced by a large metallic Ru mirror, which appears on the quartz tube after deposition. As the $Ru_3(CO)_{12}$ deposits Ru on the chamber walls, CO from thermal decomposition of the precursor is evolved from the chamber walls. This CO reaches the SiO_2 substrate, along with unreacted $Ru_3(CO)_{12}$ precursor. Thus, deposition of metallic Ru on the SiO_2 substrate occurs in an atmosphere of both $Ru_3(CO)_{12}$ precursor and CO that has evolved from the chamber walls.

CO does not adsorb to the SiO_2 substrate at the growth temperature of 575 K; however, CO does adsorb to the Ru. CO adsorbs reversibly to Ru(001) at temperatures as high as 700 K [15], and CO dissociates into C(a) and O(a) on stepped Ru(109) at ~ 480 K, which then recombines and desorbs at ~ 520 K [16]. Furthermore, CO may combine with O(a) to evolve CO_2 [17]. At the Ru growth temperature of 575 K, it is probable that CO exhibits reversible adsorption, as well as dissociation into C(a) and O(a) followed by recombinative desorption, and CO may combine with O(a) to evolve CO_2. Thus, there is a competition between CO adsorption and $Ru_3(CO)_{12}$ adsorption on the Ru.

The competition for adsorption sites between CO and $Ru_3(CO)_{12}$ most likely begins during the initial stages of nucleation. The growth of the initially-formed Ru islands is stunted because the CO blocks active sites for $Ru_3(CO)_{12}$ adsorption. This poisoning of the Ru islands depresses their growth and allows additional nucleation to occur on the SiO_2 surface. Film roughness is heavily influenced by nucleation density, and the additional nucleation that occurs on the SiO_2 substrate results in smoother films.

Previous work from our group [18] has shown that the addition of CH_3I to CVD Ru growth has a similar effect; adsorbed iodine on the Ru islands blocks adsorption sites for the O_2 co-reactant, reducing island growth and allowing further nucleation on the SiO_2. CH_3I was added during CVD Ru growth using the precursor (2,4-dimethylpentadienyl)(ethylcyclopentadienyl)Ru [DER], which requires O_2 as a co-reactant to combust the ligands of the DER. Adsorbed iodine on the Ru islands enhances the adsorption of the DER precursor; however, the iodine blocks adsorption of the essential O_2 co-reactant, which stunts Ru island growth. The improvements in nucleation afforded by the addition of CH_3I result in smoother Ru films with smaller grains [18]. In the case of the $Ru_3(CO)_{12}$, which decomposes thermally and does not require a co-reactant, adsorbed CO blocks adsorption of the precursor itself. In CVD Ru film growth from both DER/O_2 and $Ru_3(CO)_{12}$, poisoning of the Ru islands occurs by site blocking.

The smooth nature of the films grown from $Ru_3(CO)_{12}$ is strongly influenced by CO site blocking during the initial stages of nucleation; furthermore, in addition to enhancing nucleation, CO site blocking occurs continuously throughout the deposition and impacts the entire film growth. During deposition from $Ru_3(CO)_{12}$ in a CO atmosphere, the blocking of active sites by CO most likely occurs throughout the entire film growth because Ru grows on the heated chamber and evolution of CO from the walls occurs during the entire deposition. Thus, the entire deposition is influenced by the poisoning effect of CO. This continuously depressed growth rate also leads to smoother films with smaller grains, as was observed in the case of CH_3I addition and poisoning during Ru film growth [18]. It should be noted that the quartz tube was cleaned after every deposition to remove the Ru deposit, as detailed in Section 4.2.1, so that every growth began with a clean tube.

Wang et al. report the roughness of a 6 nm Ru film deposited from $Ru_3(CO)_{12}$, grown in a cold-wall CVD system, to be 1.2 nm on a Ta substrate with a roughness of 0.7 nm [19]. The roughness of a 9 nm Ru film grown in the hot-wall system is 0.40 nm on a SiO_2 substrate with a roughness of 0.19 nm. The Ru film on Ta may be rougher than those reported here because it was grown on a rougher substrate; however, it is most likely rougher because it was deposited in a cold-wall system without the influence of CO. Additional studies in a cold-wall system equipped to vary the CO partial pressure are needed to further investigate the role of CO poisoning on nucleation and film growth.

XPS analyses indicate that the films have $< 1\%$ oxygen and $\sim$ 10-20% carbon contamination. Because the oxygen contamination in these films is negligible, while carbon content is moderate, it is likely that CO dissociation into C(a) and O(a) leaves a moderate amount of C(a) in the film. Additional CO most likely combines with O(a) to evolve CO_2, which accounts for the lack of oxygen in the film.

CVD films deposited from $Ru_3(CO)_{12}$ are very smooth with little to no columnar grain structure and may be possible candidates for the liner material.

4.3.2 CVD Ru and RuO_2 Films Grown From Differing Seed Objects

Nilsen et al. have published a series of articles on the simulation of the growth of thin films from various seed objects, such as spheres, cubes, octahedra, truncated cubes, and tetragonal crystallites [9-12]. They have shown that the different types of crystal shapes forming each island during nucleation significantly impact both growth dynamics and the topography and surface roughness of the resulting films. Ru and RuO_2 CVD films closely resemble the predicted topography simulated from the growth of different types of seed objects. Film composition of the Ru and RuO_2 films was verified using high resolution XPS (not shown). Fig. 4.7 shows SEM images for films of differing topography that most likely result from the growth of different types of seed objects. CVD Ru grown with $Ru_3(CO)_{12}$ shows a spherical topography resulting from spherical seed crystals. CVD RuO_2 grown with DER and O_2 shows a needle-like topography resulting from tetragonal seed crystals. CVD Ru grown with DER and O_2 shows a roof-like termination topography resulting from truncated-cube shaped seed crystals.

Nilsen et al. state that the surface packing density of the precursor used for growth determines the type of crystal habit that forms. Thus they speculate that different seed crystals will be formed when different precursors are used for growth [10]. This is most likely why the Ru from $Ru_3(CO)_{12}$ and Ru from DER and O_2 show different topography. RuO_2 shows a different topography from Ru because it is a different material.

Furthermore, Nilsen et al. have simulated the effect of seed object on surface roughness. They have shown that spherical seed objects lead to the smoothest films [10]. For thin films, tetragonal seed objects may lead to films that could be either rougher or smoother than those from truncated cubes; however, for thick films tetragonal seed objects definitely lead to smoother films than those from truncated cubes [11]. In this study, the RuO_2 film is 98 nm, which is considered thick based on the scale used in the simulation. Thus the order of surface roughness predicted by Nilsen et al. based on seed object is spherical < tetragonal < truncated cube. Fig. 4.9b shows the simulation from [10], which includes films from spheres and truncated cubes. The roughness of films

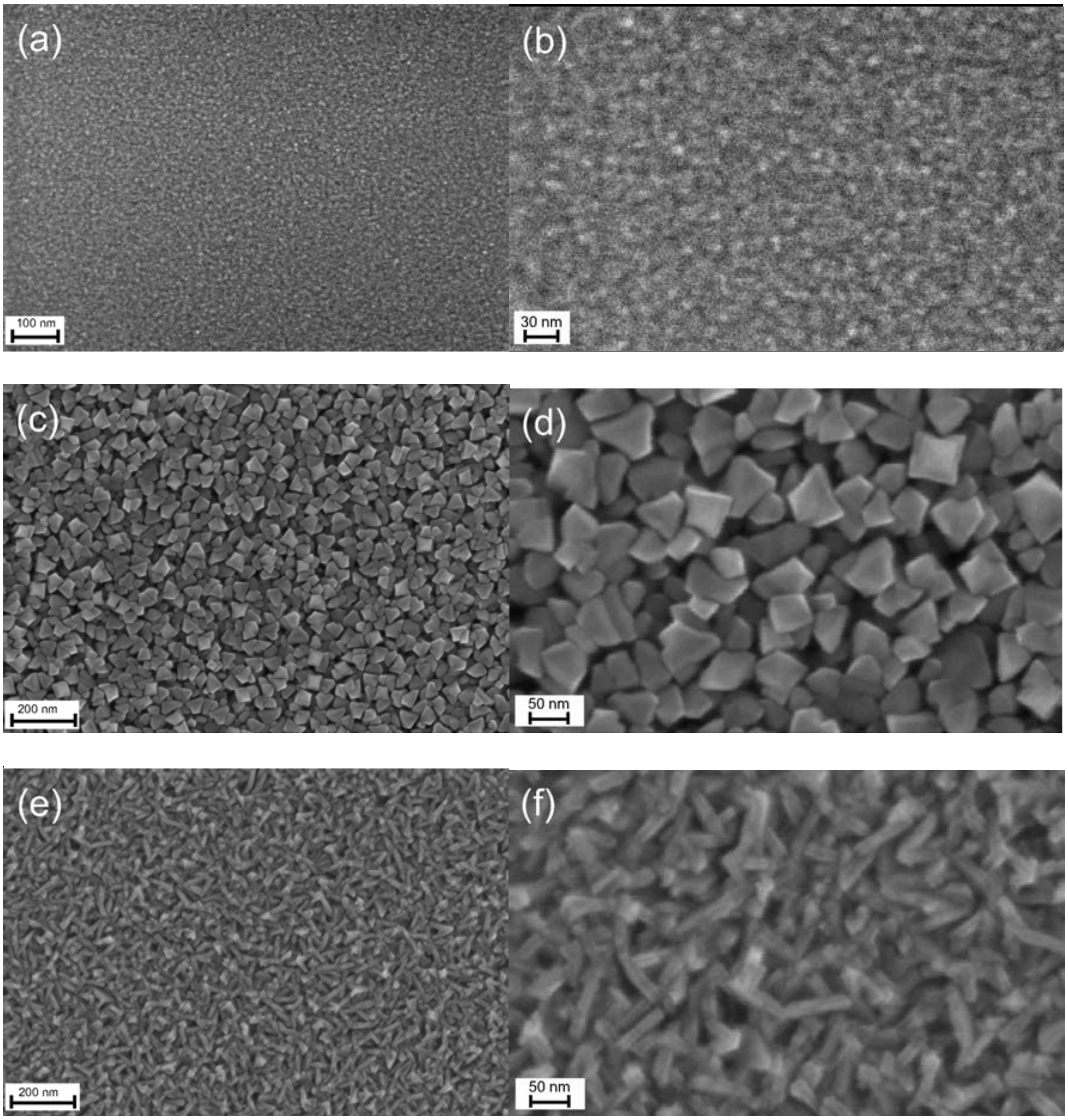

Figure 4.7. SEM images for films of a,b) Ru, 9 nm, grown with $Ru_3(CO)_{12}$, c,d) RuO_2, 98 nm, grown with DER and O_2, and e,f) Ru, 60 nm, grown with DER and O_2. The type of seed object and resulting topography are a,b) spherical seed and spherical topography, c,d) tetragonal-shaped seed and needle-like topography and e,f) truncated-cube-shaped objects and roof-like termination topography.

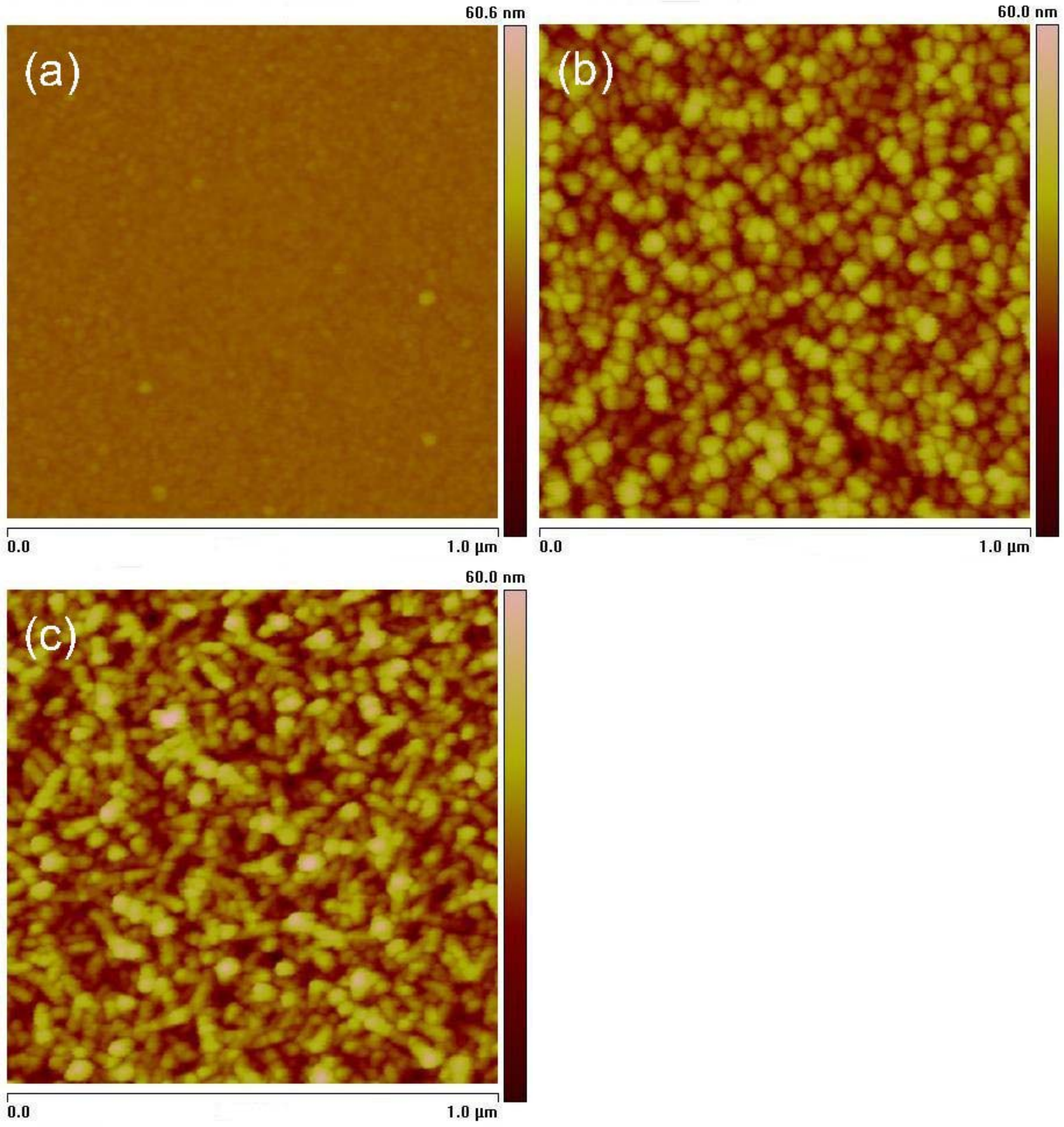

Figure 4.8. AFM images for films of a) Ru, 9 nm, grown with $Ru_3(CO)_{12}$, b) RuO_2, 98 nm, grown with DER and O_2, and c) Ru, 60 nm, grown with DER and O_2. The type of seed object and resulting topography are a,b) spherical seed and spherical topography, c,d) tetragonal-shaped seed and needle-like topography and e,f) truncated-cube-shaped objects and roof-like termination topography. The RMS roughness values are a) 0.40 nm, b) 6.54 nm, and c) 8.42 nm.

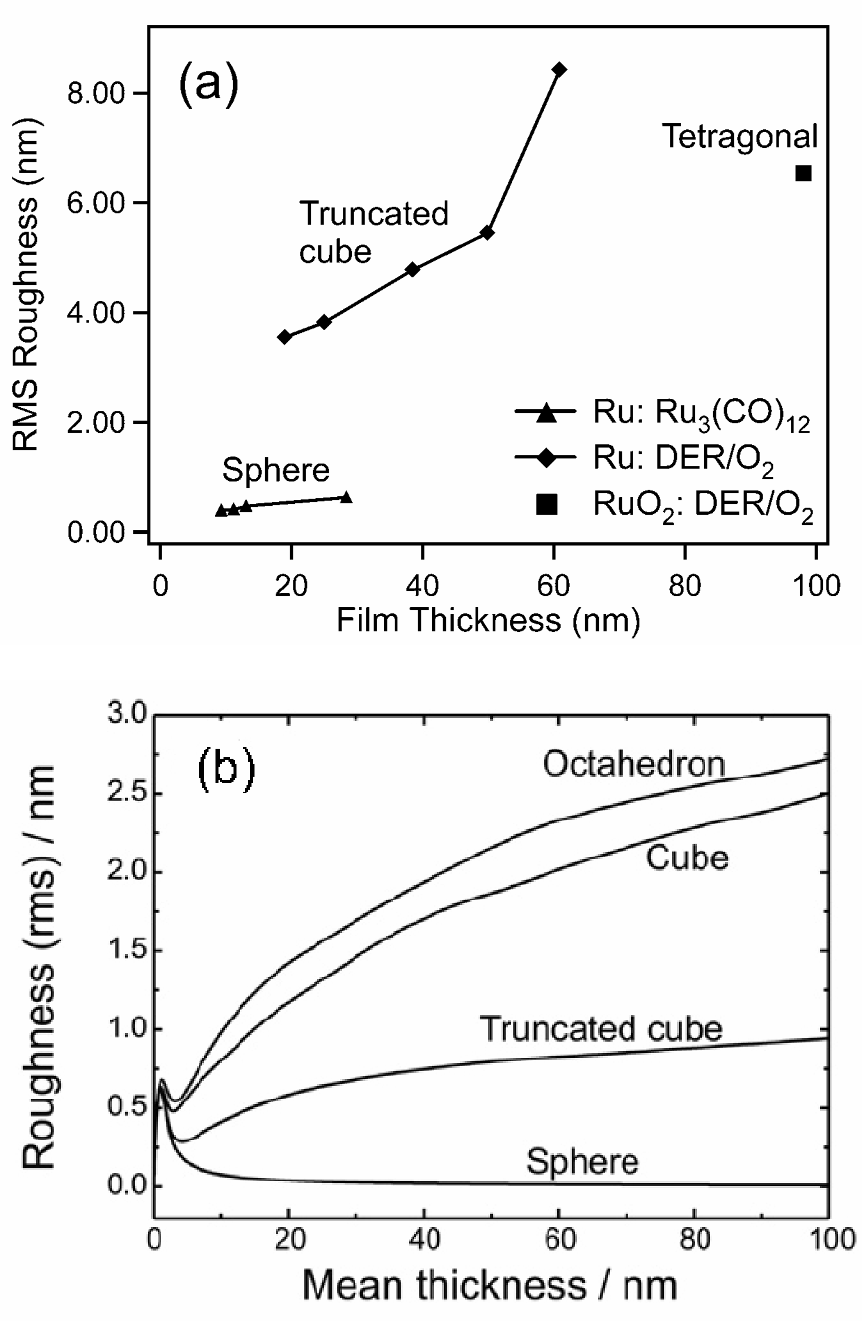

Figure 4.9. Film roughness a) determined by AFM for films of Ru grown with $Ru_3(CO)_{12}$, Ru grown with DER and O_2, and RuO_2 grown with DER and O_2 and b) for 800 seed objects for sphere, truncated cube, cube and octahedron shape as a function of the film thickness, taken from [10]. The roughness of films from tetragonal seed objects, which falls in between those of spheres and truncated cubes, is discussed in [11].

from tetragonal seed objects, which falls in between those of spheres and truncated cubes, is discussed in [11].

Fig. 4.8 shows AFM images of the Ru and RuO_2 films with differing topography. These films are of differing thicknesses, therefore it is impractical to compare roughness values directly for these three particular films. However, it is worth noting that the topography is clearly visible in the AFM images. Typically AFM tends to show grains that appear more spherical than they actually are due to data that is convoluted by the shape of the AFM tip [10].

Fig. 4.9a allows comparison of roughness values for the three different topographies for a range of film thicknesses. Ru films from $Ru_3(CO)_{12}$ (spherical) are the smoothest, followed by the RuO_2 film (tetragonal), while the Ru films from DER and O_2 are the roughest (truncated cube). Thus the experimental roughness values for the films in this study support the order of surface roughness predicted by Nilsen et al. based on seed object and resulting topography. These simulations help to explain why the Ru films grown with $Ru_3(CO)_{12}$ exhibit reduced surface roughness.

4.4. CONCLUSION

CVD Ru films grown with $Ru_3(CO)_{12}$ are very smooth, with roughness values ranging from 0.40-0.63 nm for film thicknesses of 9-28 nm. The CVD films are smoother than those of PVD and show little to no columnar grain structure in cross-section SEM. PVD Ru films show roughness values ranging from 0.11-3.36 nm for film thicknesses of 3.5-50 nm. The PVD films show surface cracking from residual film stress and have a polycrystalline columnar grain structure.

During CVD growth, Ru is deposited on the heated chamber, and the reaction by-product CO desorbs from the walls. Thus, deposition of metallic Ru on the SiO_2 substrate occurs in an atmosphere of both $Ru_3(CO)_{12}$ precursor and CO. There is a competition for adsorption sites between CO and the $Ru_3(CO)_{12}$ precursor. During deposition, the CO stunts the growth of the initially-formed Ru islands, allowing additional nucleation to occur on the SiO_2 surface, and CO continues to block active sites throughout the entire deposition. CO poisoning results in ultra-smooth Ru films with an average grain size < 10 nm.

CVD Ru and RuO_2 films closely resemble the predicted topography simulated from the growth of seed objects by Nilsen et al. Futhermore, the experimental roughness values of these films support the order of surface roughness predicted by Nilsen et al. based on seed object and the resulting topography.

4.5 REFERENCES

[1] J. Shin, A. Waheed, W. A. Winkenwerder, H.-W. Kim, K. Agapiou, R. A. Jones, G. S. Hwang, J. G. Ekerdt, Thin Solid Films 515 (2007) 5298.

[2] L. B. Henderson, J. G. Ekerdt, Thin Solid Films 517 (2009) 1645.

[3] I. Goswami, R. Laxman, Semicond. Int. 27 (2004) 49.

[4] H. Kim, Surf. Coat. Technol. 200 (2006) 3104.

[5] J. Shin, H.-W. Kim, G. S. Hwang, J. G. Ekerdt, Surf. Coat. Technol. 201 (2007) 9256.

[6] J. Shin, D. Gay, Y.-M. Sun, J. M. White, J. G. Ekerdt, AIP Conf. Proc. 788 (2005) 482.

[7] H. Marom, M. Eizenberg, J. Appl. Phys. 99 (2006) 123705.

[8] W. Tang, K. Xu, P. Wang, X. Li, Microelectronic Eng. 66 (2003) 445.

[9] O. Nilsen, O. B. Karlsen, A. Kjekshus, H. Fjellvåg, Thin Solid Films 515 (2007) 4527.

[10] O. Nilsen, O. B. Karlsen, A. Kjekshus, H. Fjellvåg, Thin Solid Films 515 (2007) 4538.

[11] O. Nilsen, O. B. Karlsen, A. Kjekshus, H. Fjellvåg, Thin Solid Films 515 (2007) 4550.

[12] O. Nilsen, O. B. Karlsen, A. Kjekshus, H. Fjellvåg, J. Crystal Growth 308 (2007) 366.

[13] H. Kim, I. Rabelo de Moraes, G. Tremiliosi-Filho, R. Haasch, A. Wieckowski, Surf. Sci. 474 (2001) L203.

[14] R. O. E. Vijgen, J. H. Dautzenberg, Thin Solid Films 270 (1995) 264.

[15] T. E. Madey, D. Menzel, Proc. Int. Conf. Solid Surf. 2 (1974) 229.

[16] T. Zubkov, G. A. Morgan Jr., J. T. Yates Jr., Chem. Phys. Lett. 362 (2002) 181.

[17] I. Rosso, M. Antonini, C. Galletti, G. Saracco, V. Specchia, Topics in Catal. 30 (2004) 475.

[18] K. M. Thom, J. G. Ekerdt, Thin Solid Films (2009) (in press).

[19] Q. Wang, J. G. Ekerdt, D. Gay, Y.-M. Sun, J. M. White, Appl. Phys. Lett. 84 (2004) 1380.

Chapter 5: Summary

5.1 CONCLUSIONS

The research presented in this dissertation offers contributions toward the use of Ru in the liner in integrated circuits. Fundamental surface science investigations and film growth studies reveal that the precursor DER is suitable for CVD Ru, and nucleation and film properties can be improved by the addition of methyl iodide. In addition, use of the $Ru_3(CO)_{12}$ precursor results in thin, ultra-smooth films, which are good candidates for inclusion in the liner.

Surface science investigations of DER on polycrystalline Ta were performed. When the Ta is held at 140 K, the majority of DER dosed to the surface adsorbs and desorbs molecularly. TPD indicates that multilayer DER desorbs between 272 and 263, with kinetics that appear to be fractional order with repulsive interactions. The multilayer zero coverage desorption energy is 0.9 eV. Monolayer DER desorbs between 278 and 297 K, exhibiting kinetics that appear to be first order with attractive lateral interactions. The monolayer zero coverage desorption energy is 2.3 eV. XPS Ru 3d BE values increase with increasing exposure. The observed shift is attributed to the influence of core hole screening in the monolayer regime and increased sample charging as the DER overlayer becomes thicker in the multilayer regime. Saturation of the monolayer occurs in the exposure range of 1.3-3.6 L, although second layer DER is evident for exposures as low as 0.64 L and may even be present for lower exposures. The sticking coefficient of DER drops significantly once all the Ta surface sites have been occupied, as evidenced by both the abrupt change in slope of the TPD uptake curve and the minimal change in

XPS overlayer thickness from 10.5 to 14.5 nm for exposures of 1.3 to 38.1 L. DER exhibits a 3D island growth mode due to the random formation of 3D hit and stick structures, which develop due to the lack of adsorbate mobility at 140 K. Annealing experiments are consistent with the proposed growth mode. Although the majority of DER adsorbs molecularly, a minor surface reaction occurs at defect sites. The surface reaction results in ligand desorption (both EtCp and DMPD) and hydrocarbon and Ru-hydrocarbon species that remain on the Ta surface.

When the Ta is held between 298-773 K, DER decomposes leaving mostly hydrocarbon species on the surface. No Ru is evident in the XP spectra until 673 K. The XPS BE decreases with increasing temperature, indicating that the amount of molecular dissociation increases with temperature. However, the BE never reaches that of metallic Ru, indicating that the DER cannot fully decompose by thermal means alone. When the Ta is pre-covered with atomic iodine, DER dissociation is significantly decreased while adsorption is increased. The iodine blocks dissociation sites and increases the vertical potential of the Ta surface, allowing more of the impinging molecules to adsorb.

The CVD of Ru films from DER and O_2 was carried out both with and without CH_3I addition. The addition of CH_3I results in more populous, uniform nucleation, which ultimately leads to smaller-grained, smoother films. For films grown both with and without CH_3I addition, XPS results indicate ~ 7% oxygen and ~ 7% carbon contamination; therefore, the addition of CH_3I does not significantly increase the amount of carbon in the films. XPS also indicates that the majority of the adsorbed iodine segregates through the films to the surface during growth, which results in a continuously depressed deposition rate. SEM images show that the addition of CH_3I more than doubles the number of islands on the surface, and the improvement in nucleation results in smaller-grained, smoother films. AFM indicates that the roughness of all films grown with CH_3I is decreased from that of films not grown with CH_3I; for instance, the roughness of 60 nm films decreased from 8.42 to 5.62 nm for no CH_3I and CH_3I addition, respectively. During nucleation, the adsorbed iodine stunts the growth of the initially-formed islands, allowing time for additional nucleation to occur on the SiO_2 surface. The iodine is active throughout the entire film deposition because it segregates through the film during growth. The role of iodine during nucleation and film growth is primarily to block O_2 adsorption and dissociation sites, which reduces the oxygen supply available to decompose the ligands of the DER precursor. Furthermore, surface science studies of DER on polycrystalline Ta indicate that adsorbed iodine also increases DER adsorption (which may block additional active sites available for O_2 adsorption and dissociation), and decreases DER dissociation, which may also contribute to the stunted nucleation and depressed growth rate.

CVD Ru films were grown with $Ru_3(CO)_{12}$ and compared with PVD Ru films. AFM indicates that the CVD Ru films are very smooth, with roughness values ranging from 0.40-0.63 nm for film thicknesses of 9-28 nm. The PVD films are also smooth, with roughness values ranging from 0.11-3.4 nm for film thicknesses of 3.5-50 nm; however, the CVD films are smoother than those from PVD. SEM analyses indicate that the CVD films have a very smooth surface topography, and cross-sectional images show little to no columnar grain structure. The PVD films have a rougher surface topography that shows cracking due to residual stress in the films, and cross-sectional images show significant polycrystalline columnar grain structure. The smooth surface and reduction of grain boundaries in the CVD Ru films make them possible candidates for the liner material.

During CVD growth, Ru is deposited on the heated chamber, and the reaction by-product CO desorbs from the walls. Thus, deposition of metallic Ru on the SiO_2 substrate occurs in an atmosphere of both $Ru_3(CO)_{12}$ precursor and CO. There is a competition for adsorption sites between CO and the $Ru_3(CO)_{12}$ precursor. During deposition, the CO stunts the growth of the initially-formed Ru islands, allowing additional nucleation to occur on the SiO_2 surface, and CO continues to block active sites throughout the entire deposition. CO poisoning results in ultra-smooth Ru films with an average grain size < 10 nm.

CVD films of Ru (from $Ru_3(CO)_{12}$ and DER/O_2) and RuO_2 (from DER/O_2) closely resemble the predicted topography simulated from the growth of seed objects by Nilsen et al [1-4]. Ru films grown with $Ru_3(CO)_{12}$ showed a spherical topography resulting from spherical seed crystals, while Ru grown with DER and O_2 shows a roof-like termination topography resulting from truncated-cube shaped seed crystals. The difference in seed crystal and topography is a result of the different growth precursors. CVD RuO_2 grown with DER and O_2 shows a needle-like topography resulting from tetragonal seed crystals. RuO_2 shows a different topography from Ru because it is a different material. Futhermore, Nilsen et al. predict the order of surface roughness based on seed object and the resulting topography to be spherical < tetragonal < truncated cube [2,3]. The experimental roughness values of the CVD films support the order of surface roughness predicted by Nilsen et al.

5.2 RECOMMENDATIONS FOR FUTURE WORK

Although nucleation and surface roughness of CVD Ru films grown with DER and O_2 showed improvement with the addition of CH_3I, this precursor chemistry is not practical for industrial applications. The semiconductor industry is hesitant to introduce O_2 into manufacturing, as it may oxidize other sensitive components, such as Cu at the bottom of vias and Ta/TaN [5,6]. However, the concept of introducing a “contaminant” to alter the growth of the initially-formed islands and the growing film, in order to manipulate nucleation and film properties, may be extendable to other precursor chemistries.

In CVD Ru film growth, CH_3I effectively poisons the growth of the islands, allowing time for additional nucleation to occur on the substrate, by blocking active sites needed for precursor and co-reactant adsorption/dissociation. It would be interesting to study other atoms and/or molecules that may poison growth. For instance, it is known that sulfur poisons Ru catalysts, such as those used for the methanation of CO [7]. The effect of sulfur on CVD Ru film growth should be explored. It is possible that sulfur may block active sites and impact nucleation and growth in a manner similar to CH_3I.

Furthermore, this work investigated the role of CO poisoning on Ru films grown from $Ru_3(CO)_{12}$ in a hot-wall CVD system. Ru nucleation and film growth were influenced by CO desorbing from the heated walls of the chamber. In order to further investigate the role of CO poisoning, it is necessary to conduct experiments in a cold-wall CVD system in which CO is added during growth. Experiments in which the CO partial pressure is varied in a cold-wall CVD system would help eludicate the impact of CO on Ru film growth.

In this work, the method of enhancing nucleation involved altering the reactivity of the initially-formed islands towards the precursor, resulting in stunted island growth. It would also be worthwhile to attempt to alter the reactivity of the substrate towards the precursor, resulting in more populous nucleation without depressing the growth rate. Ru precursors nucleate more readily on hydroxylated surfaces, and it would be interesting to explore the reactivity of other functional groups toward Ru precursors. $Ru(EtCp)_2$ can be deposited in NH_3 plasma (without O_2). It may be worthwhile to explore the effect of $–NH_3$ terminated surfaces on Ru nucleation.

CVD films grown with $Ru_3(CO)_{12}$ are very smooth and show little to no columnar grain structure. For this reason, it is possible that these films may have sufficient microstructure to act as a Cu diffusion barrier. In this case, the CVD Ru film could not only replace the Ta/Cu seed layer, but may be sufficient to replace the entire TaN/Ta/Cu seed layer multilayer stack. However, issues with adhesion of Ru to the dielectric are of concern. It would still be worthwhile to evaluate the barrier properties of the films grown with $Ru_3(CO)_{12}$ and compare them with those of conventional Ta/TaN barriers. Previous work in our group has shown that bias temperature stress (BTS) time-to-failure analysis is a strong method to evaluate barrier properties.

In this work, all CVD Ru films were grown on planar substrates. The conformality of films should be examined on patterned wafers with high-aspect ratio features. In addition, growth on substrates other than SiO_2 should be explored. If the CVD Ru film will replace the Ta/Cu seed layer, but the liner will still retain the TaN diffusion barrier, it will be important to examine CVD Ru films on TaN substrates. The surface roughness of CVD Ru on TaN should be evaluated. Because TaN is a rougher substrate than SiO_2, it is expected that CVD Ru films on TaN will be rougher than those on SiO_2. It is important to determine if CVD Ru grown with $Ru_3(CO)_{12}$ exhibits excellent surface roughness on different substrates.

In our research group, the carbon content in Ru films is determined by XPS. Due to overlap between the Ru $3d_{3/2}$ and C 1s XPS peaks, carbon content must be estimated by fitting the 3d peaks; however, small errors obtained in peak fitting can lead to large errors in estimating the carbon content. The amount of carbon in a film is of particular concern because carbon increases the film resistivity. It would be useful to obtain determinations of carbon content from methods other than XPS. Both secondary ion mass spectrometry (SIMS) and elastic recoil detection analysis (ERDA) are methods that can be used to determine carbon content in Ru films.

In this work, film thicknesses were determined by cross-section SEM (X-SEM). Previous work in our group has used XPS peak attenuation to calculate film thickness; however, if the films are excessively rough and/or have significant island structure, XPS grossly underestimates thickness. For instance, a 60 nm Ru film grown with DER/O_2, determined by X-SEM, appears to be only ~ 8 nm using XPS peak attenuation. However, X-SEM cannot be used to determine thickness for films < 10 nm due to edge effects. It is imperative that an additional method of determining film thickness be used for films < 10 nm.

X-ray Reflectometry (XRR) is a method that allows determination of film thickness, roughness, and density. Thicknesses determined by XRR would offer complementary data to X-SEM for thicker films and provide a more accurate measure for films < 10 nm. In addition, roughness values from XRR could be compared with those determined by AFM, and information about film density would be obtained. Finally, the issue of determining the minimum possible thickness to achieve a continuous film is of great importance and difficulty. It is possible that XRR may be used to help address this issue.

5.3 REFERENCES

[1] O. Nilsen, O. B. Karlsen, A. Kjekshus, H. Fjellvåg, Thin Solid Films 515 (2007) 4527.

[2] O. Nilsen, O. B. Karlsen, A. Kjekshus, H. Fjellvåg, Thin Solid Films 515 (2007) 4538.

[3] O. Nilsen, O. B. Karlsen, A. Kjekshus, H. Fjellvåg, Thin Solid Films 515 (2007) 4550.

[4] O. Nilsen, O. B. Karlsen, A. Kjekshus, H. Fjellvåg, J. Crystal Growth 308 (2007) 366.

[5] O. K. Kwon, S. H. Kwon, H. S. Park, S. W. Kang, J. Electrochem. Soc. 151 (2004) C753.

[6] H. G. Tompkins, J. A. Sellers, J. Vac. Sci. Technol. *A* 12 (1994) 2446.

[7] V. S. Kamble, V. P. Londhe, N. M. Gupta, K. Ravindranathan Thampi, M. Grätzel, J. Catal. 158 (1996) 427.

Bibliography

[1] T. Aaltonen, P. Alen, M. Ritala, M. Leskela, Chem. Vap. Deposition 9 (2003) 45.

[2] T. Aaltonen, Antti Rahtu, M. Ritala, M. Leskelä, Electrochem. Solid-State Lett. 6 (2003) C130.

[3] K. Andersson, A. Gómez, C. Glover, D. Nordlund, H. Öström, T. Schiros, O. Takahashi, H. Ogasawara, L. G. M. Pettersson, A. Nilsson, Surf. Sci. 585 (2005) L183.

[4] O. J. Bchir, Ph.D Dissertation, The University of Florida (2004).

[5] O. J. Bchir, K. M. Green, H. M. Ajmera, E. A. Zapp, T. J. Anderson, B. C. Brooks, L. L. Reitfort, D. H. Powell, K. A. Abboud, L. McElwee White, J. Am. Chem. Soc. 127 (2005) 7825.

[6] O. J. Bchir, K. M. Green, M. S. Hlad, T. J. Anderson, B. C. Brooks, C. B. Wilder, D. H. Powell, L. McElwee-White, J. Organometallic Chem. 684 (2003) 338.

[7] M. T. Bohr, Tech. Dig., Int. Electron Devices Meet. (1995) 241.

[8] A. S. Bolina, A. J. Wolff, W. A. Brown, J. Chem. Phys. 122 (2005) 044713.

[9] J. Camarero, L. Spendeler, G. Schmidt, K. Heinz, J. J. de Miguel, R. Miranda, Phys. Rev. Lett. 73 (1994) 2448.

[10] C.-M. Chan, R. Aris, W. H. Weinburg, Appl. Surf. Sci. 1 (1978) 360.

[11] M. A. Chesters, B. J. Hopkins, M. R. Leggett, Surf. Sci. 43 (1974) 1.

[12] K. Choi, J. Lim, S. Roy, C. Lee, Jpn. J. Appl. Phys 42 (2003) 5539.

[13] O. Chyan, T. N. Arunagiri, T. Ponnuswamy, J. Electrochem Soc. 150 (2003) C347.

[14] W. Frie*β*, H. Schlichting, D. Menzel, Phys. Rev. Lett. 74 (1995) 1147.

[15] P. G. Ganesan, M. Eizenberg, C. Dornfest, J. Electrochem. Soc. 149 (2002) G510.

[16] I. Goswami, R. Laxman, Semicond. Int. 27 (2004) 49.

[17] I. Gouzman, M. Dubey, M. D. Carolus, J. Scwartz, S. L. Bernasek, Surf. Sci. 600 (2006) 773.

[18] M. L. Green, M. E. Gross, L. E. Papa, K. J. Schnoes, D. Brasen, J. Electrochem. Soc. 132 (1985) 2677.

[19] O. Gunnarsson, K. Schönhammer, Phys. Scripta 21 (1980) 575.

[20] H. Han, J. J. Kim, D. Y. Yoon, J. Vac. Sci. Technol. A 22 (2004) 1120.

[21] N. J. Havercroft, P. M. A. Sherwood, Surf. Interface Anal. 29 (2000) 232.

[22] L. B. Henderson, J. G. Ekerdt, Thin Solid Films 517 (2009) 1645.

[23] M. A. Henderson, G. E. Mitchell, J. M. White, Surf. Sci. 184 (1987) L325.

[24] J. Heo, S.-J. Won, D. Eom, S. Y. Lee, Y. B. Ahn, C. S. Hwang, H. J. Kim, Electrochem Solid-State Lett. 11 (2008) H210.

[25] C.-K. Hu, Mat. Res. Soc. Sym. Proc. 511 (1998) 305.

[26] W. X. Huang, J. M. White, J. Phys. Chem. B 108 (2004) 5060.

[27] E. S. Hwang, J. Lee, Chem. Mater. 12 (2000) 2076.

[28] E. S. Hwang, J. Lee, Electrochem. Solid-State Lett. 3 (2000) 138.

[29] International Technology Roadmap for Semiconductors, 2007 Edition, http://public.itrs.net (2007).

[30] M. Kadoshima, T. Nabatame, M. Hiratani, Y. Nakamura, I. Asano, T. Suzuki, Jpn. J. Appl. Phys. 41 (2002) L347.

[31] A. E. Kaloyeros, E. Eisenbraun, Ann. Rev. Mat. Sci. 30 (2000) 363.

[32] V. S. Kamble, V. P. Londhe, N. M. Gupta, K. Ravindranathan Thampi, M. Grätzel, J. Catal. 158 (1996) 427.

[33] S. Y. Kang, K. H. Choi, S. K. Lee, C. S. Hwang, H. J. Kim, J. Electrochem. Soc. 147 (2000) 1161.

[34] S. Y. Kang, C. S. Hwang, H. J. Kim, J. Electrochem. Soc. 152 (2005) C15.

[35] N. Karl, Ch. Günther, Cryst. Res. Technol. 34 (1999) 243.

[36] K. Kawano, H. Kosuge, N. Oshima, H. Funakubo, Electrochem. Solid-State Lett. 10 (2007) D60.

[37] K. Kawano, A. Nagai, H. Kosuge, T. Shibutami, N. Oshima, H. Funakubo, Electrochem. Solid-State Lett. 9 (2006) C107.

[38] H. Kim, Surf. Coating Technol. 200 (2006) 3104.

[39] H. Kim, I. Rabelo de Moraes, G. Tremiliosi-Filho, R. Haasch, A. Wieckowski, Surf. Sci. 474 (2001) L203.

[40] J. J. Kim, D. H. Jung, M. S. Kim, S. H. Kim, D. Y. Yoon, Thin Solid Films 409 (2002) 28.

[41] J. J. Kim, M. S. Kim, D. Y. Yoon, Chem. Vap. Deposition 9 (2003) 105.

[42] S. K. Kim, S. Y. Lee, S. W. Lee, G. W. Hwang, C. S. Hwang, J. W. Lee, J. Jeong, J. Electrochem. Soc. 154 (2007) D95.

[43] A. Kis, J. Kiss, F. Solymosi, Surf. Sci. 459 (2000) 149.

[44] A. Klekamp, E. Umbach, Surf. Sci. 249 (1991) 75.

[45] A. Kohn, M. Eizenberg, Y. Shacham-Diamond, Appl. Surf. Sci. 212 (2003) 367.

[46] O.-K. Kwon, S.-H. Kwon, H.-S. Park, S.-W. Kang, J. Electrochem. Soc. 151 (2004) C753.

[47] M. W. Lane, C. E. Murray, F. R. McFeely, P. M. Vereecken, R. Rosenburg, Appl. Phys. Lett. 83 (2003) 2330.

[48] H.-B. Lee, D.-K. Kwak, S.-W. Kang, Electrochem. Solid-State Lett. 8 (2005) C39.

[49] A. M. Lemonds, J. M. White, J. G. Ekerdt, Surf. Sci. 527 (2003) 124.

[50] A. M. Lemonds, J. M. White, J. G. Ekerdt, Surf. Sci. 538 (2003) 191.

[51] J. Lim, H. Park, C. Lee, Thin Solid Films 475 (2005) 194.

[52] J.-L. Lin, B. E. Bent, J. Vac. Sci. Technol. A 10 (1992) 2202.

[53] J. Liu, J. Lei, N. Magtoto, S. Rudenja, M. Garza, J. A. Kelber, J. Electrochem. Soc. 152 (2005) G115.

[54] B. Luo, Q. Wang, J. M. White, Chem. Vap. Deposition, 10 (2004) 311.

[55] T. E. Madey, D. Menzel, Proc. Int. Conf. Solid Surf. 2 (1974) 229.

[56] H. Marom, M. Eizenberg, J. Appl. Phys. 99 (2006) 123705.

[57] Y. Matsui, M. Hiratani, T. Nabatame, Y. Shimamoto, S. Kimura, Electrochem. Solid-State Lett. 4 (2001) C9.

[58] Y. Matsui, M. Hiratani, T. Nabatame, Y. Shimamoto, S. Kimura, Electrochem. Solid-State Lett. 5 (2002) C18.

[59] K. C. McGee, M. D. Dreissen, V. H. Grassian, J. Catal. 159 (1996) 69.

[60] J. B. Miller, H. R. Siddiqui, S. M. Gates, J. N. Russell, Jr., J. T. Yates, Jr., J. C. Tully, M. J. Cardillo, J. Chem. Phys. 87 (1987) 6725.

[61] G. E. Moore, Electronics 38 (1965) 114.

[62] S. P. Murarka, S. W. Hymes, Crit. Rev. Solid State Mat. Sci. 20 (1995) 87.

[63] J. W. Niemantsverdriet, K. Wandelt, J. Vac. Sci. Technol. A 6 (1988) 757.

[64] O. Nilsen, O. B. Karlsen, A. Kjekshus, H. Fjellvåg, Thin Solid Films 515 (2007) 4527.

[65] O. Nilsen, O. B. Karlsen, A. Kjekshus, H. Fjellvåg, Thin Solid Films 515 (2007) 4538.

[66] O. Nilsen, O. B. Karlsen, A. Kjekshus, H. Fjellvåg, Thin Solid Films 515 (2007) 4550.

[67] O. Nilsen, O. B. Karlsen, A. Kjekshus, H. Fjellvåg, J. Crystal Growth 308 (2007) 366.

[68] J. Papadatos, S. Consiglio, S. Skordas, E. T. Eisenbraun, A. E. Kaloyeros, J. Peck, D. Thompson, C. Hoover, J. Mater. Res. 19 (2004) 2947.

[69] K. J. Park, J. M. Doub, T. Gougousi, G. N. Parsons, Appl. Phys. Lett. 86 (2005) 051903.

[70] S.-E. Park, H.-M. Kim, K.-B. Kim, S.-H. Min Electrochem. Solid-State Lett. 1 (1998) 262.

[71] M. Parschau, K. Christmann, Surf. Sci. 347 (1996) 63.

[72] K. R. Paserba, A. J. Gellman, Phys. Rev. Lett. 86 (2001) 4338.

[73] L. Peters, Semiconductor International 24 (2001) 66.

[74] T. Rockey, H.-L. Dai, Surf. Sci. 601 (2007) 2307.

[75] I. Rosso, M. Antonini, C. Galletti, G. Saracco, V. Specchia, Topics in Catal. 30 (2004) 475.

[76] J. Schnadt, J. N. O'Shea, L. Patthey, J. Schiessling, J. Krempaský, M. Shi, N. Mårtensson, P. A. Brühwiler, Surf. Sci. 544 (2003) 74.

[77] T. Shibutami, K. Kawano, N. Oshima, S. Yokoyama, H. Funakubo, Electrochem. Solid-State Lett. 6 (2003) C117.

[78] T. Shibutami, K. Kawano, N. Oshima, S. Yokoyama, H. Funakubo, Mat. Res. Soc. Symp. Proc. 748 (2003) 111.

[79] J. Shin, D. Gay, Y.-M. Sun, J. M. White, J. G. Ekerdt, AIP Conf. Proc. 788 (2005) 482.

[80] J. Shin, H.-W. Kim, G. S. Hwang, J. G. Ekerdt, Surf. Coat. Technol. 201 (2007) 9256

[81] J. Shin, A. Waheed, W. A. Winkenwerder, H.-W. Kim, K. Agapiou, R. A. Jones, G. S. Hwang, J. G. Ekerdt, Thin Solid Films 515 (2007) 5298.

[82] K. C. Smith, Y.-M. Sun, N. R. Mettlach, R. L. Hance, J. M. White, Thin Solid Films 376 (2000) 73.

[83] Y.-H. Song, Y.-L. Chen, Y. Chi, C.-S. Liu, W.-L. Ching, J.-J. Kai, R.-S. Chen, Y.-S. Huang, A. J. Carty, Chem. Vap. Deposition 9 (2003) 162.

[84] D. Stacchiola, Y. Wang, W. T. Tysoe, Surf. Sci. 524 (2003) 173.

[85] W. Tang, K. Xu, P. Wang, X. Li, Microelectronic Eng. 66 (2003) 445.

[86] S. Tanuma, C. J. Powell, D. R. Penn, Surf. Interface Anal. 17 (1991) 927.

[87] S. Tanuma, C. J. Powell, D. R. Penn, Surf. Interface Anal. 21 (1994) 165.

[88] K. M. Thom, J. G. Ekerdt, Surf. Sci. 603 (2009) 920.

[89] K. M. Thom, J. G. Ekerdt, Thin Solid Films (2009) (in press).

[90] B. J. Tielsch, J. E. Fulghum, Surf. Interface Anal. 24 (1996) 28.

[91] B. J. Tielsch, J. E. Fulghum, Surf. Interface Anal. 24 (1996) 459.

[92] H. G. Tompkins, J. A. Sellers, J. Vac. Sci. Technol. *A* 12 (1994) 2446.

[93] B. Ulgut, S. Suzer, J. Phys. Chem. B 107 (2003) 2939.

[94] L. H. Van Vlack, Elements of Materials Science and Engineering, 6th Ed. (1990**)**.

[95] S. Varma, P. A. Dowben, J. Vac. Sci. Technol. A 8 (1990) 2605.

[96] J. A. Venables, Introduction to Surface and Thin Film Processes (2000).

[97] R. O. E. Vijgen, J. H. Dautzenberg, Thin Solid Films 270 (1995) 264.

[98] K. Wandelt, B. Gumhalter, Surf. Sci. 140 (1984) 355.

[99] Q. Wang, J. G. Ekerdt, D. Gay, Y.-M. Sun, J. M. White, Appl. Phys. Lett. 84 (2004) 1380.

[100] D. Welipitiya, C. N. Borca, C. Waldfried, C. Hutchings, L. Sage, C. M. Woodbridge, P. A. Dowben, Surf. Sci. 393 (1997) 34.

[101] M. C. Wheeler, D. C. Seets, C. B. Mullins, J. Chem. Phys. 105 (1996) 1572.

[102] C. Whitman, M. M. Moslehi, A. Paranjpe, L. Velo, T. Omstead, J. Vac. Sci. Technol. A 17 (1999) 1893.

[103] J. E. Whitten, Surf. Sci. 546 (2003) 107.

[104] C.-C. Yang, T. Spooner, S. Ponoth, K. Chanda, A. Simon, C. Lavoie, M. Lane, C.-K. Hu, E. Liniger, L. Gignac, T. Shaw, S. Cohen, F. McFeely, D. Edelstein, Proc. IEEE International Interconnect Tech. Conf. (2006) 187.

[105] B. Zhao, M. Brongo, Mat. Res. Soc. Symp. Proc. 564 (1999) 485.

[106] W. Zhao, W. Wei, J. M. White, Surf. Sci. 547 (2003) 374.

[107] X.-L. Zhou, F. Solymosi, P. M. Blass, K. C. Cannon, J. M. White, Surf. Sci. 219 (1989) 294.

[108] X.-L. Zhou, J. M. White, Surf. Sci. 194 (1988) 438.

[109] X.-L. Zhou, C. Yoon, J. M. White, Surf. Sci. 206 (1988) 379.

[110] Y. Zhou, M. A. Henderson, W. M. Feng, J. M. White, Surf. Sci. 224 (1989) 386.

[111] T. Zubkov, G. A. Morgan Jr., J. T. Yates Jr., Chem. Phys. Lett. 362 (2002) 181.

Vita

Kelly Marriott Thom, daughter of Bertrum and Patricia Green, was born in St. Petersburg, FL, on June 15, 1978. She attended the Pinellas County Center for the Arts (PCCA) at Gibbs High School in St. Petersburg, FL, where she majored in violin performance and served as concertmaster of the PCCA Chamber Orchestra from her sophomore year until graduation in 1996. Kelly earned Bachelor of Science degrees in both Chemical Engineering and Chemistry from The University of Florida in Gainesville, FL, graduating Cum Laude in 2003. In 2004, she began her graduate studies at The University of Texas at Austin under the supervision of Dr. John G. Ekerdt.

At The University of Florida, Kelly worked for Dr. Timothy J. Anderson as an undergraduate research assistant in the area of thin film technology. She spent 2.5 years aiding graduate student Omar Bchir in the deposition and characterization of WN_xC_y films for use as a Cu diffusion barrier. She was the recipient of the University of Florida Chemical Engineering Alumni Scholarship Award.

For her graduate work at UT Austin, Kelly was the first recipient of the five-year GRC/Al Tasch Fellowship for doctoral study in microelectronics-related disciplines, awarded by the Semiconductor Research Corporation (SRC). She also received a four-year College of Engineering Doctoral Fellowship awarded by UT Austin. During graduate school, she studied the deposition and characterization of chemical vapor deposition (CVD) Ru films, with a focus on enhancing nucleation and improving film properties.

Kelly has authored and co-authored five publications in refereed journals, including Thin Solid Films, Surface Science, the Journal of the American Chemical Society, the Journal of Crystal Growth, and the Journal of Organometallic Chemistry. During graduate school, her work was presented at the SRC Techcon in Austin, TX in November 2008 and September 2007; the AVS 54th International Symposium in Seattle, WA in October 2007; the SRC Student Symposium in Raleigh, NC in September 2006; and the SRC Techcon in Portland, OR in September 2005.

Permanent address: 1713 Lady Grey Avenue Pflugerville, TX 78660

This dissertation was typed by the author.